AD-A120 416 II-IV-V2 CHALCOPYRITES FOR HIGH SPEED DEVICES(U) 1/2
WASHINGTON UNIV ST LOUIS MO SEMICONDUCTOR RESEARCH LAB
C M WOLFE ET AL. 31 JUL 82 WU/SRL-59457-5
UNCLASSIFIED AFOSR-TR-82-0906 AFOSR-79-0096 F/G 20/2 NL

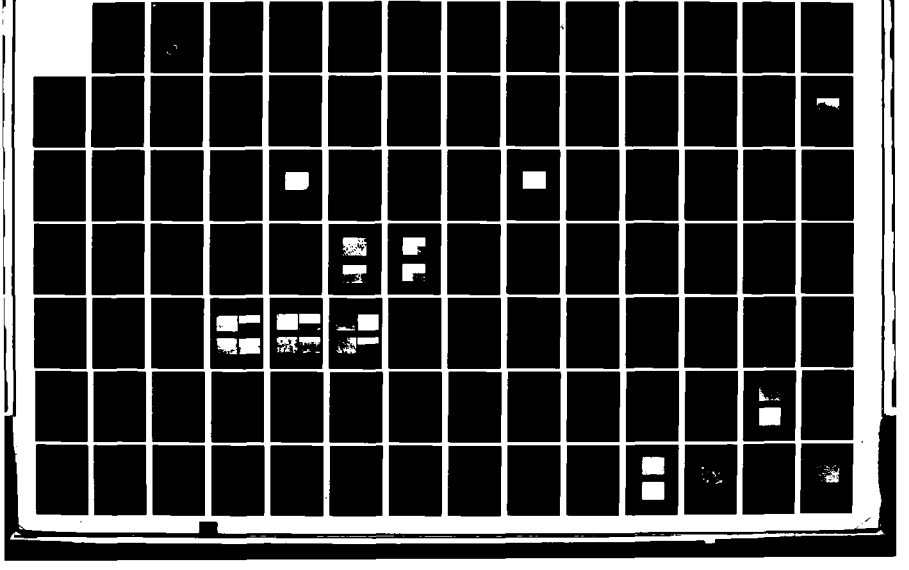

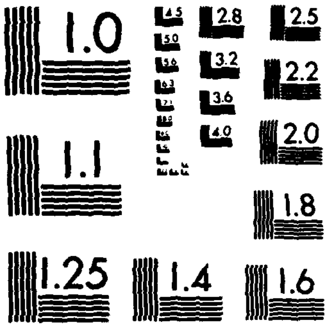

MICROCOPY RESOLUTION TEST CHART
NATIONAL BUREAU OF STANDARDS-1963-A

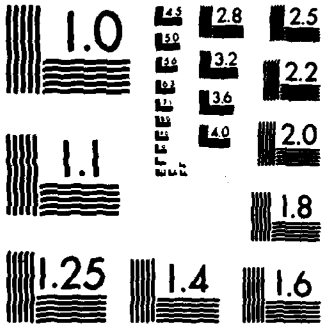

MICROCOPY RESOLUTION TEST CHART
NATIONAL BUREAU OF STANDARDS-1963-A

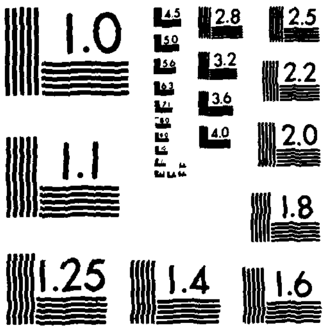

MICROCOPY RESOLUTION TEST CHART
NATIONAL BUREAU OF STANDARDS-1963-A

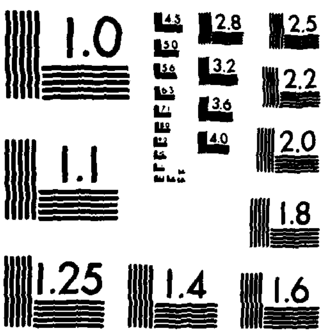

MICROCOPY RESOLUTION TEST CHART
NATIONAL BUREAU OF STANDARDS-1963-A

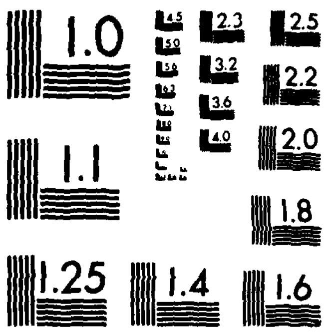

MICROCOPY RESOLUTION TEST CHART
NATIONAL BUREAU OF STANDARDS-1963-A

WASHINGTON UNIVERSITY IN ST. LOUIS

AFOSR-TR- 82-0906

11

II-IV-V_2 CHALCOPYRITES FOR HIGH SPEED DEVICES

SEMICONDUCTOR RESEARCH LABORATORY

Washington University

Saint Louis, Missouri 63130

31 July 1982

FINAL TECHNICAL REPORT NO. WU/SRL-59457-5

1 June 1979 to 31 May 1982

Air Force Office of Scientific Research
Building 410
Bolling Air Force Base, DC20332

Grant No. AFOSR-79-0096

Unclassified

SECURITY CLASSIFICATION OF THIS PAGE (When Data Entered)

REPORT DOCUMENTATION PAGE		READ INSTRUCTIONS BEFORE COMPLETING FORM
1. REPORT NUMBER AFOSR-TR- 82-0906	2. GOVT ACCESSION NO. AD-A120416	3. RECIPIENT'S CATALOG NUMBER
4. TITLE (and Subtitle) II-IV-V_2 Chalcopyrites for High Speed Devices		5. TYPE OF REPORT & PERIOD COVERED Final 1 June 79-31 May 82
		6. PERFORMING ORG. REPORT NUMBER WU/SRL-59457-5
7. AUTHOR(s) C.M. Wolfe, M.W. Muller, G.A. Davis, and S. Julie Hsieh		8. CONTRACT OR GRANT NUMBER(s) AFOSR-79-0096
9. PERFORMING ORGANIZATION NAME AND ADDRESS Washington University Box 1127 St. Louis, MO 63130		10. PROGRAM ELEMENT, PROJECT, TASK AREA & WORK UNIT NUMBERS 2306/[redacted] 61102F
11. CONTROLLING OFFICE NAME AND ADDRESS Air Force Office of Scientific Research Building 410 Bolling AFB, DC 20332		12. REPORT DATE 31 July 82 13. NUMBER OF PAGES 136
14. MONITORING AGENCY NAME & ADDRESS(if different from Controlling Office)		15. SECURITY CLASS. (of this report) Unclassified 15a. DECLASSIFICATION/DOWNGRADING SCHEDULE

16. DISTRIBUTION STATEMENT (of this Report)

Approved for public release;
distribution unlimited.

17. DISTRIBUTION STATEMENT (of the abstract entered in Block 20, if different from Report)

18. SUPPLEMENTARY NOTES

19. KEY WORDS (Continue on reverse side if necessary and identify by block number)

$CdSnP_2$, $Zn_xCd_{1-x}SnP_2$, $ZnGeAs_2$, epitaxial growth, transport properties, high-speed devices, heterostructures, inertial transport device, Zener oscillations.

20. ABSTRACT (Continue on reverse side if necessary and identify by block number)

There is evidence that some of the II-IV-V_2 chalcopyrites have basic electronic properties that are superior to the properties of their analog III-V sphalerite compounds for high speed devices. The primary objective of this work was to investigate techniques for the growth of high-quality epitaxial II-IV-V_2 chalcopyrite layers on III-V substrates. For this purpose we initially selected $CdSnP_2$ which nearly lattice

(over)

DD FORM 1 JAN 73 1473 EDITION OF 1 NOV 65 IS OBSOLETE

Unclassified

SECURITY CLASSIFICATION OF THIS PAGE (When Data Entered)

20. Abstract (continued)

matches InP and $ZnGeAs_2$ which matches GaAs.

Using liquid phase epitaxial methods it was found that the lattice match between $CdSnP_2$ and InP is not close enough to obtain high-quality layers. The layer morphology was greatly improved by growing lattice matched $Zn_xCd_{1-x}SnP_2$ on InP. One of these layers had a room temperature electron mobility of 2000 cm^2/V sec at a concentration of $3x10^{19}cm^{-3}$, which is substantially larger than can be obtained in InP at the same concentration. At the other end of this chalcopyrite alloy, $ZnSnP_2$ was found to closely lattice match GaAs with good morphology. Some of these layers exhibited hole mobilities of 70 cm^2/V sec at concentrations of about $1x10^{18}cm^{-3}$. Attempts to obtain n-type conductivity in $ZnSnP_2$ were unsuccessful. For both $CdSnP_2$ and $ZnSnP_2$ the conductivity increased with increased loss of volatile constituents.

Several chloride-transport vapor-phase methods were examined in an unsuccessful effort to grow $ZnGeAs_2$ layers epitaxially on GaAs substrates. Our experience with these methods indicates that most of the reproducibility problems could be overcome with a hydride transport process.

Discussions in the literature have pointed out several problems with the usual theory of heterostructures. We present a general, first-order, nonequilibrium thermodynamic analysis which points out that one problem with conventional theory is that it neglects a generalized thermodynamic force. This force can be associated with the gradient of the effective density-of-states. In heterostructures such gradients cause the charge carriers to move into regions with higher density-of-states, thus increasing the entropy of the system in agreement with the second law of thermodynamics. We also show that if the electrochemical potential is referenced to the infinite vacuum level, then the electron affinity rule must be valid in the absence of interface states.

One application for some of the II-IV-V_2 chalcopyrites may be in inertial transport devices. Calculations are presented on the I-V characteristics of a space-charge limited diode. If the electrons exhibit inertial motion (are not scattered), then they will quickly reach nonparabolic regions of the conduction band. When this nonparabolicity is taken into account, the current appears ohmic rather than exhibiting a $V^{3/2}$ behavior, as has been previously supposed. Inertial transport may also be utilized to achieve a terahertz Zener oscillator. If Zener oscillations are to be used as coherent radiation sources, the carriers must oscillate in phase. A scheme is proposed for phase initialization and focusing, whereby carriers are injected into an interaction region in phase, and scattered carriers are eliminated from the interaction region. The method utilizes injection across a heterojunction energy barrier, a submicron interaction region, and electromagnetic feedback.

TABLE OF CONTENTS

1. INTRODUCTION

The II-IV-V_2 chalcopyrites have several potential advantages over III-V compounds and alloys for high speed device applications. For example, $ZnGeAs_2$ and $CdSnP_2$ are expected[1] to have lower conduction band effective masses than their technologically important III-V compound analogs, GaAs and InP. This together with the differences in band structure[2] could result in higher hot electron mobilities and saturated drift velocities for the II-IV-V_2 chalcopyrites. One might also expect some of the ordered II-IV-V_2 compounds to have higher carrier mobilities and thermal conductivities than their equivalent disordered III-V alloys. The technology of the II-IV-V_2 chalcopyrites, however, is not as advanced as that of their III-V analogs and few of these potential advantages have been realized. In fact, the state of the art for these materials is about the same as that for the III-V compounds a number of years ago, when the current interest in III-V compounds for device applications began to develop. Considering the potential advantages of these materials this work was undertaken to develop some of the II-IV-V_2 compounds into technologically useful materials.

1.1 MATERIAL CONSIDERATIONS

Just as it was for the III-V compounds, it is difficult to determine which of the II-IV-V_2 chalcopyrites are most promising for high-speed device applications. If we take into account the evolution of the III-V compounds, we would choose the ternary analogs of GaAs and InP: $ZnGeAs_2$ and $CdSnP_2$.

$ZnGeAs_2$ has been determined to have an energy gap of 1.15 eV[2], somewhat lower than the 1.43 eV of GaAs. With a lattice constant of 5.672 Å[3] it should be possible to grow it epitaxially on Ge with a lattice mismatch of 0.25 percent or on GaAs with a mismatch of 0.34 percent. However, it has only been grown from the melt with high p-type conductivity and low mobility[3]. $CdSnP_2$ has been determined to have an energy gap of about 1.17 eV[4], somewhat lower than the 1.35 eV of InP. With a lattice constant of 5.900 Å[3] it could be grown epitaxially on InP with a mismatch of 0.53 percent. More work has been done on $CdSnP_2$ than on $ZnGeAs_2$[5]. $CdSnP_2$ has previously been grown epitaxially on InP from a Sn melt with low n-type conductivity and reasonable mobility[6]. It has also been made p-type[7]. The conduction band effective mass for $CdSnP_2$ has been measured to be 0.036 m[5] which is better than half the mass of InP and less than the calculated value of 0.059 m[1] for $CdSnP_2$.

To utilize the potential high-speed capabilities of any of the II-IV-V_2 chalcopyrites it is necessary to grow well-controlled epitaxial layers of the material on semi-insulating and heavily-doped substrates. An examination of the CdP_2-Sn phase diagram[8] indicates that $CdSnP_2$ forms peritectically and that it can be grown from a Sn-rich solution at temperatures between 220 and 570°C. As indicated, this method has been used to grow layers of $CdSnP_2$ epitaxially on InP substrates[6] and has also been used to grow platelets of $CdSnP_2$. Thus, liquid epitaxy seems to be a good technique for growing $CdSnP_2$.

The $ZnGeAs_2$ phase diagram [9] indicates a high solubility of Ge which precludes the use of liquid epitaxy to grow this material. This high Ge solubility may account for the poor quality of material grown from the melt. For this reason a vapor-phase technique should be a suitable method for growing $ZnGeAs_2$ epitaxially on GaAs or Ge substrates.

The heterostructure properties of $CdSnP_2$ grown on InP substrates and $ZnGeAs_2$ on GaAs or Ge could be helpful for high speed device applications. The somewhat lower band-gap of $CdSnP_2$ compared to InP and $ZnGeAs_2$ compared to GaAs could help confine carriers to the epitaxial layer and thus prevent the injection of hot electrons into the substrate in the same manner as has been discussed [10] for InGaAs FETs on GaAs. Also, to obtain exact lattice matched heterostructures, it may be possible to grow alloys of these materials with other chalcopyrites on InP and GaAs.

1.2 RESEARCH OBJECTIVES

The objectives of this work as they evolved from these arguments and the work itself were to:

(1) develop techniques for the growth of high-quality epitaxial $Zn_xCd_{1-x}SnP_2$ on InP and GaAs and $ZnGeAs_2$ on GaAs or Ge;

(2) minimize electrically-active defects and residual impurities in these materials to achieve well-controlled doping;

(3) investigate the electrical transport properties of these materials to determine their suitability for heterostructures and high-speed device applications;

(4) develop the technology required for the fabrication of suitable device structures; and

(5) investigate novel high-speed device concepts which could utilize the unique properties of these chalcopyrite materials.

1.3 REFERENCES

1. H. Kildal, Ph.D. Thesis, Stanford University (1972).
2. A. Shileika, Surface Science 37, 730 (1973).
3. A.S. Borshchevskii, N.A. Goryunova, F.P. Kesamanly, and D.N. Nasledov, Phys. Stat. Solidi 21, 9 (1976).
4. J.L. Shay, E. Buehler, and J.H. Wernick, Phys. Rev. B 2, 4104 (1970).
5. J.L. Shay and J.H. Wernick, Ternary Chalcopyrite Semiconductors (Pergamon Press, Oxford, 1975).
6. S. Knight, E. Buehler, and I. Camlibel, J. Appl. Phys. 43, 3422 (1972).
7. E.I. Leonov, V.N. Orlov, V.I. Sokolova, and Yu. G. Shreter, Phys. Stat. Solidi (a) 8, 387 (1971).
8. E. Buehler, J.H. Wernick, and J.L. Shay, Mater. Res. Bull. 6, 303 (1971).
9. A.S. Borshchevskii, N.A. Goryunova, F.P. Kesamanly, and D.N. Nasledov, Phys. Stat. Solidi 21, 9 (1967).
10. D.R. Decker, R.D. Fairman, and C.K. Neshimoto, Proc. Cornell. Elect. Eng. Conf. 5, 305 (1975).

2. LIQUID PHASE EPITAXIAL GROWTH OF $Zn_xCd_{1-x}SnP_2$

$CdSnP_2$ is a semiconductor material of some interest for high speed and microwave devices because it has a smaller electron effective mass than its III-V analog InP [1] and because of the observation of negative differential mobility at high electric fields [2-3]. In addition, since $CdSnP_2$ has a bandgap and lattice constant close to those of InP it seems to be a good material for heterostructure devices with InP. Growth of $CdSnP_2$ as platelets [4] and epitaxially on InP [5] has so far yielded material with high carrier concentrations and low mobilities compared to the III-V compounds. In fact, attempts to produce epitaxial layers of $CdSnP_2$ on InP have yielded layers with very poor morphology and much lower mobilities compared to the platelets. One objective of this project was to grow $CdSnP_2$ platelets and make measurements of their electrical characteristics and to improve the quality of epitaxial layers grown on InP in an attempt to grow device quality material.

As in the $CdSnP_2$/InP system $ZnSnP_2$ growth on GaAs is of interest for the study of heterostructure devices. In addition $ZnSnP_2$ is an attractive material for the study of chalcopyrite growth on the III-V sphalerite structure of GaAs for numerous reasons although no epitaxial growth experiments have yet been reported. The lattice constant of $ZnSnP_2$ mismatches that of GaAs by only 0.04% so liquid phase growth can be achieved

without alloying as was required in the $CdSnP_2$/InP system. Because the c/a ratio of the tetragonal $ZnSnP_2$ structure is 2.00 growth experiments can be performed on various substrate orientations without incorporating any c-to-2a mismatch. This allows us to study the effects of substrate orientation on LPE growth which was not possible in the $CdSnP_2$/InP system. The second objective of this project was to study the LPE growth of $ZnSnP_2$ on GaAs to determine if $ZnSnP_2$ is a potentially useful semiconductor material.

$CdSnP_2$ and $ZnSnP_2$ are crystals which grow with the chalcopyrite lattice structure shown in Figure 1. This structure resembles the sphalerite structure of the III-V compounds with the Column III element sublattice being replaced by a Column II element sublattice and a Column IV element sublattice. $CdSnP_2$ is a direct analog of InP since the In sublattice is replaced by Cd and Sn sublattices where Cd and Sn straddle In on the periodic table. To accomodate these two sublattices the size of the cubic unit cell must be doubled. Most chalcopyrites exhibit a uniaxial compression along their longer dimension ($ZnSnP_2$ is an exception) so that two different lattice constants are needed to describe the cubic unit cell: a and c as shown in Figure 1 where $c/a \leq 2$ for all chalcopyrites.

Various material parameters for $CdSnP_2$, $ZnSnP_2$, GaAs, and InP are presented in Table 1 [6]. The mismatch of $CdSnP_2$ on InP is 0.53%, which is considered small for some growth systems but which is large for LPE growth. This is believed to be the major reason for poor morphology and

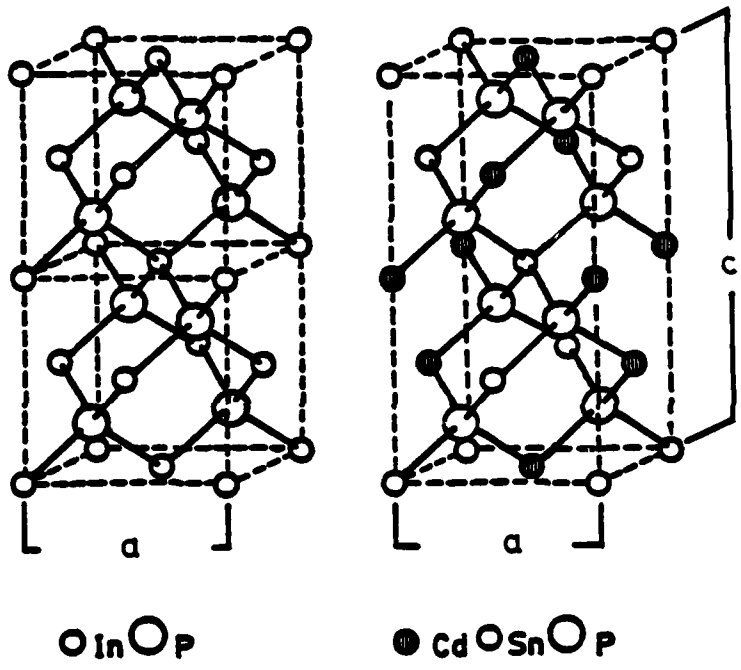

Figure 1 Cubic unit cells of the InP sphalerite structure and the $CdSnP_2$ chalcopyrite structure.

Table 1 Physical properties of
InP, GaAs, $CdSnP_2$, and $ZnSnP_2$

	InP	GaAs	$CdSnP_2$	$ZnSnP_2$
a(Å)	5.8688	5.65315	5.900	5.651
c(Å)	--	--	11.513	11.302
c/a	--	--	1.951	2.00
Eg(ev)	1.28	1.35	1.17	1.66
M.P.(°C)	1070	1237	570	930

poor electrical properties of $CdSnP_2$ epitaxial layers on InP. The a lattice constant of $ZnSnP_2$ is a good deal smaller than that of InP so a chalcopyrite alloy of $CdSnP_2$ and $ZnSnP_2$ might be produced which can lattice match InP. This was the impetus behind the experiments attempting to grow the lattice matched chalcopyrite alloy, $Zn_xCd_{1-x}SnP_2$ on InP. Assuming Vegard's law is approximately obeyed, the alloy composition which lattice matches {100} InP is $Zn_{0.13}Cd_{0.87}SnP_2$.

It should be noted that $CdSnP_2$ has a melting point much smaller than those of most semiconductor materials and so the growth of $CdSnP_2$ is restricted to comparatively low temperatures. In addition, loss of volatile constituents from the melt, especially phosphorus, will be appreciable near the melting point.

Because the melting point of $ZnSnP_2$ is closer to those of the III-V compounds the growth of $ZnSnP_2$ is not as restricted. However, $ZnSnP_2$ makes a phase transition to a disordered sphalerite phase at 720°C [6]. This phase has been observed in solution grown platelets in which cooling rates greater than 5°C/hr were used [9]. Thus LPE growth of $ZnSnP_2$ on GaAs is restricted at least to temperatures below 720°C and cooling rates less than 5°C/hr in order to grow the chalcopyrite phase.

2.1 $CdSnP_2$ PLATELETS

2.1.1 Growth Procedure

$CdSnP_2$ was initially grown as platelets from a Sn solution to make material property measurements and for possible use as a source material in the LPE system. Following a procedure described by Buehler *et al* [4], elemental Cd, Sn and red P_4 were placed in a vitreous carbon boat and sealed in an eight inch 25 mm O.D. quartz ampoule evacuated to a residual pressure of 2×10^{-6} torr. All elemental materials used were 99.999% pure. The quartz ampoule was nominally 1 mm thick to withstand the phosphorus pressures produced on heating. The carbon boat, quartz ampoule and quartz sealing plug had been cleaned in aqua regia for 24 hours and baked out under vacuum prior to loading. The ampoule was heated over a period of six hours, allowed to homogenize for one hour, and then slowly cooled to 230°C. A schematic of a typical sealed ampoule is shown in Figure 2. Data for these growth runs are given in Table 2.

The resulting ingots containing $CdSnP_2$ in Sn were immersed in Hg and heated to about 60°C to dissolve the Sn. The $CdSnP_2$ crystals were separated from the bulk of the Hg-Sn solution by passing it through a gauze sieve and the remaining solution was removed in 33% HNO_3. The resulting $CdSnP_2$ material was typically in the form of

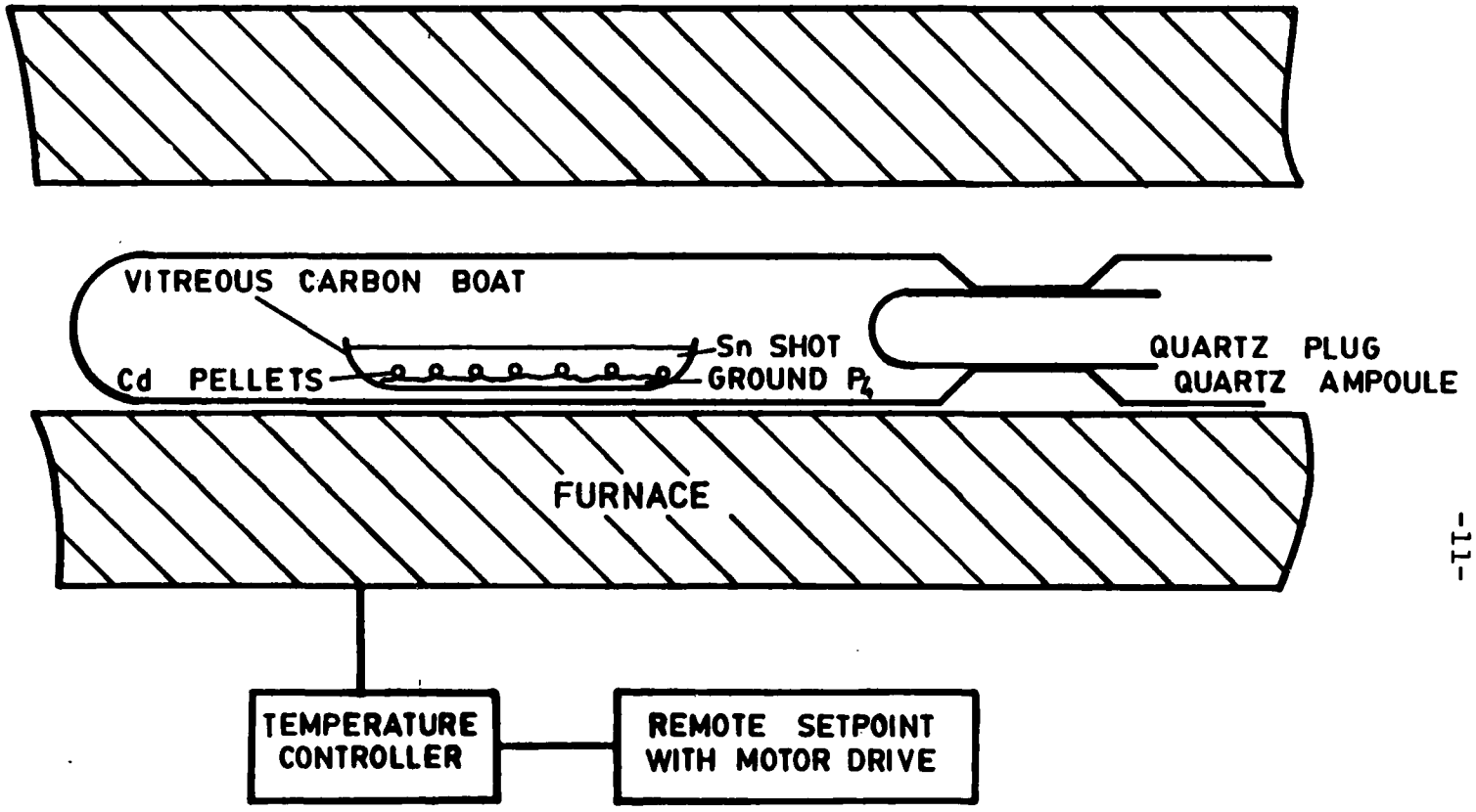

Figure 2 Sealed ampoule system used for growing $CdSnP_2$ platelets.

Table 2 Data for sealed tube $CdSnP_2$ platelet growth.

RUN	MOLAR % Cd	MOLAR % Sn	MOLAR % P	TOTAL MASS (Grams)	HOMOGENIZATION TEMPERATURE (^{o}C)	COOLING RATE ($^{o}C/Hr$)
C-5	1.8	94.7	3.5	23.1	600	2.5
E-1	2.5	92.5	5.0	10.4	600	2.5
E-3	8.0	76.8	15.2	11.2	700	10.0
E-4	10.9	69.2	19.9	9.8	715	10.0
E-5	8.0	74.0	18.0	10.1	600	10.0
E-6	8.0	77.0	15.0	11.3	600	10.0
E-7	5.8	83.6	10.6	13.3	700	7.3
F-1	8.0	76.8	15.2	11.2	850	2
F-2	7.9	77.0	15.0	11.3	700	5
F-3	8.0	76.9	15.1	11.2	700	5
F-4	7.0	79.0	14.0	11.0	700	5

10 mm x 4 mm x 3 mm odd shaped single crystals mixed with an abundance of smaller crystals (2 mm x 2 mm x 2 mm).

2.1.2 Sample Preparation

Experimental samples were prepared from the larger platelets by chemical-mechanical polishing with a 1% Br in methyl alcohol solution. The resulting samples were 100 μm to 400 μm thick with parallel flat surfaces of area 0.25 cm^2 to 0.50 cm^2.

2.1.3 Contacts

Ohmic contacts were made to the $CdSnP_2$ samples using 10 mil and 20 mil diameter Sn spheres alloyed at 300°C for two minutes in a high purity hydrogen atmosphere. These contacts were found to have a contact resistance of 1.9×10^{-4} Ω cm^2 at 300 K. Although these contacts adhered well to the sample surface at 300 K they tended to break off of the samples when immersed in liquid nitrogen. No contact resistance measurements were made at 77 K.

Gold plated onto the surface of several samples produced softly rectifying contacts. The contacts were alloyed for twenty seconds at 300°C in a hydrogen atmosphere to produce ohmic contacts. No contact resistance measurements were made on these contacts.

Al contacts evaporated onto the surface of several samples gave rectifying contacts with various reverse breakdown voltages ranging from one to five volts.

The best barriers were obtained by evaporating Al onto the entire sample, masking contact regions with apiezon wax, and removing the excess Al in HF. The contacts produced in this manner had higher breakdown voltages than those produced by Al evaporation through a glass or metal mask.

2.1.4 Hall and Resistivity Measurements

The majority of $CdSnP_2$ samples were used for van der Pauw and Hall measurements at 300 K, 77 K, and at elevated temperatures (300 K to 625 K). These samples were prepared as described above with four 10 mil diameter Sn contacts alloyed to the sample surfaces. Those samples which were measured at elevated temperatures were encapsulated with pyrolytic SiO_2 grown at 300°C. The encapsulant layers were 0.20 μm to 0.40 μm thick.

The samples measured at 300 K were n type with a mean carrier concentration of $1 \times 10^{17} cm^{-3}$ and a mean mobility of 725 $cm^2/V\text{-sec}$. The better samples had carrier concentrations in the range of 5×10^{16} to $8 \times 10^{16} cm^{-3}$ with mobilities of 1400 to 2000 $cm^2/V\text{-sec}$. When these samples were measured at 77 K, no substantial changes in the carrier concentrations or mobilities from the 300 K values were observed. 300 K and 77 K measurements were made using a 2.15 kG permanent magnet.

High temperature Hall measurements were made in the apparatus shown schematically in Figure 3. These measurements were made in hydrogen purified by a palladium diffusion cell using a flow rate of 15 ml/min. A 3.5 kG magnetic field produced by a four-inch electromagnet was used for these measurements.

High temperature measurements of the encapsulated samples were limited to temperatures below 700 K due to irreversible changes in the samples. The results of measurements on a typical sample are plotted in Figure 4. In these experiments the temperature was increased from room temperature and measurements were taken every 25 K. The circles in Figure 4 are the data for the initial set of measurements and the squares are from a subsequent set of measurements which were made after the sample had returned to room temperature. These data indicate a steady increase in the carrier concentration and decrease in the mobility with increasing temperature up to 600 K. Above 600 K the changes accelerate and are irreversible as can be seen from the lower mobilities and higher carrier concentrations at low temperatures in the latter measurements.

The irreversible changes are due to loss of volatile constituents from the samples; probably

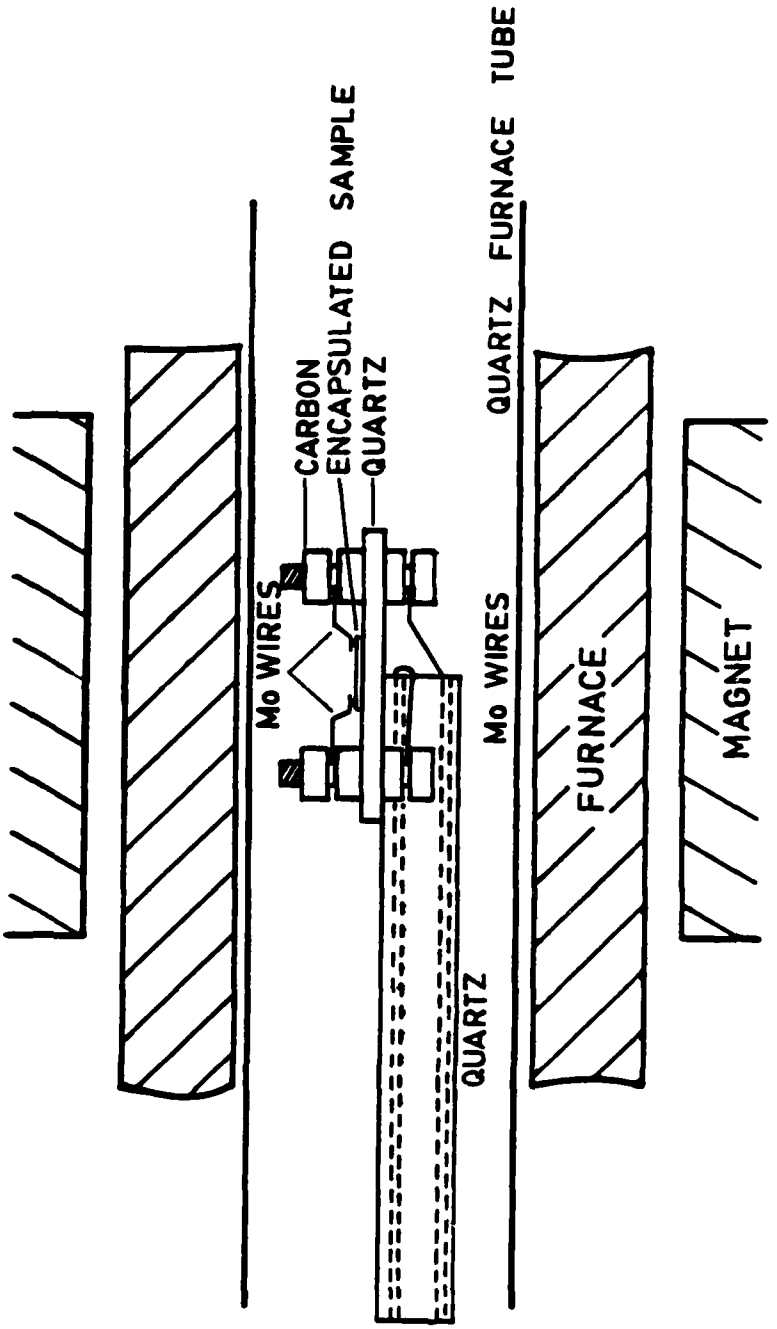

Figure 3 Schematic of high temperature Hall measurement apparatus.

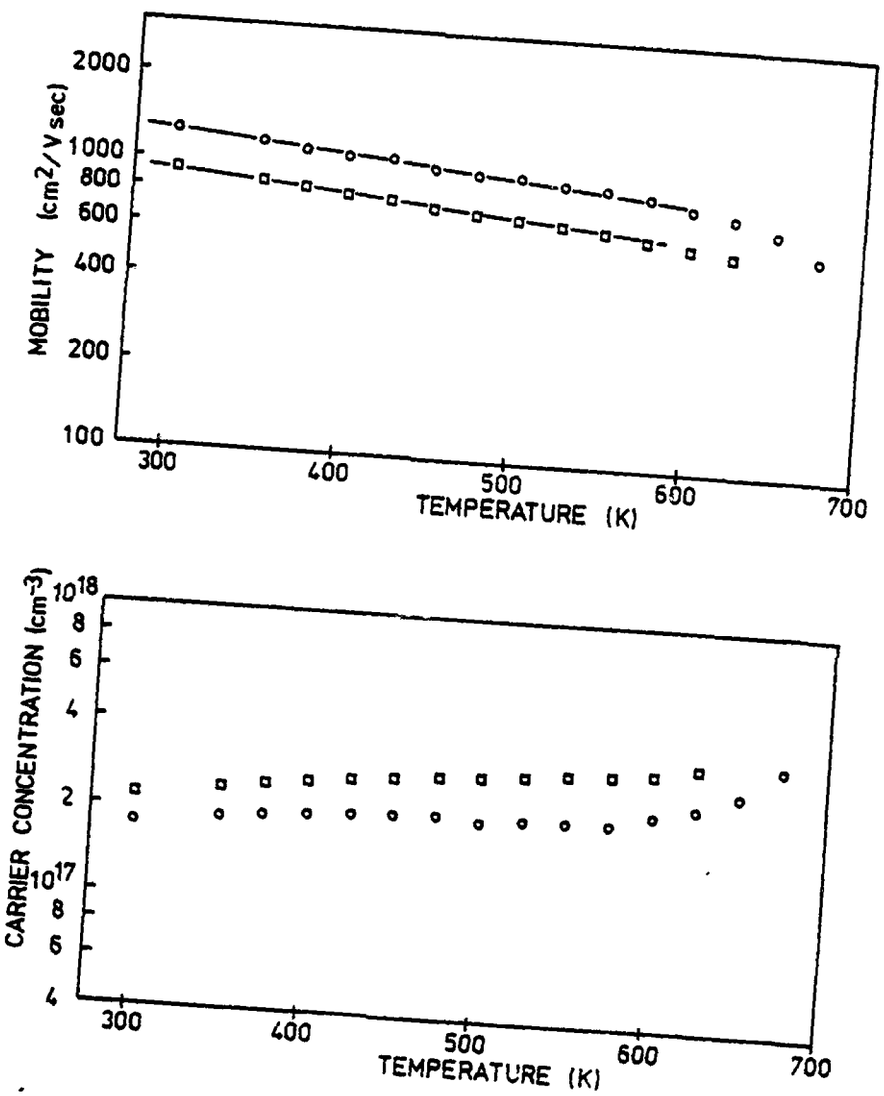

Figure 4 High temperature Hall data for a $CdSnP_2$ platelet sample.

phosphorus due to its high vapor pressure. This is supported by the observation of numerous cracks in the encapsulating layers of the samples after measurements were made. The above data indicate that depletion of volatile components from the samples causes an increased n type carrier concentration and a decreased mobility. Thus, to produce epitaxial layers of high quality, emphasis should be placed on maintaining a high concentration of the volatile component in the growth melts.

2.2 $CdSnP_2$ GROWN ON InP

2.2.1 Sealed Tube Epitaxial Growth

Epitaxial growth experiments were initially performed using a tipping boat arrangement described by Shay *et al* [5] which is shown schematically in Figure 5. In these experiments a carbon boat was used to contain the substrate and growth melt. The growth melt was homogenized in a separate step by loading the cleaned carbon boat with 99.999% Cd, Sn, and red P_4 and sealing the boat in a cleaned quartz ampoule evacuated to a residual pressure of 2×10^{-6} torr. The starting materials were measured to give a molar composition of 94% Sn, 2% Cd, and 4% P with a total mass of 10.6 grams. This ampoule was then heated to 600°C over a period of six hours, allowed to homogenize for an hour, and quenched. The quartz ampoule was broken open, a substrate was inserted into the carbon boat, and the boat was sealed in another quartz ampoule after evacuating to 2×10^{-6} torr and backfilling with argon to 620 torr. The {100} Fe-doped InP substrate had been prepared by chemical-mechanical polishing one face with 4% bromine-methyl alcohol followed by cleaning in boiling trichloroethylene, acetone, and methyl alcohol, and a four minute etch in 2% bromine-methyl alcohol. The loaded ampoule was held in a vertical furnace as shown in Figure 5 and was rapidly heated to 525°C and allowed

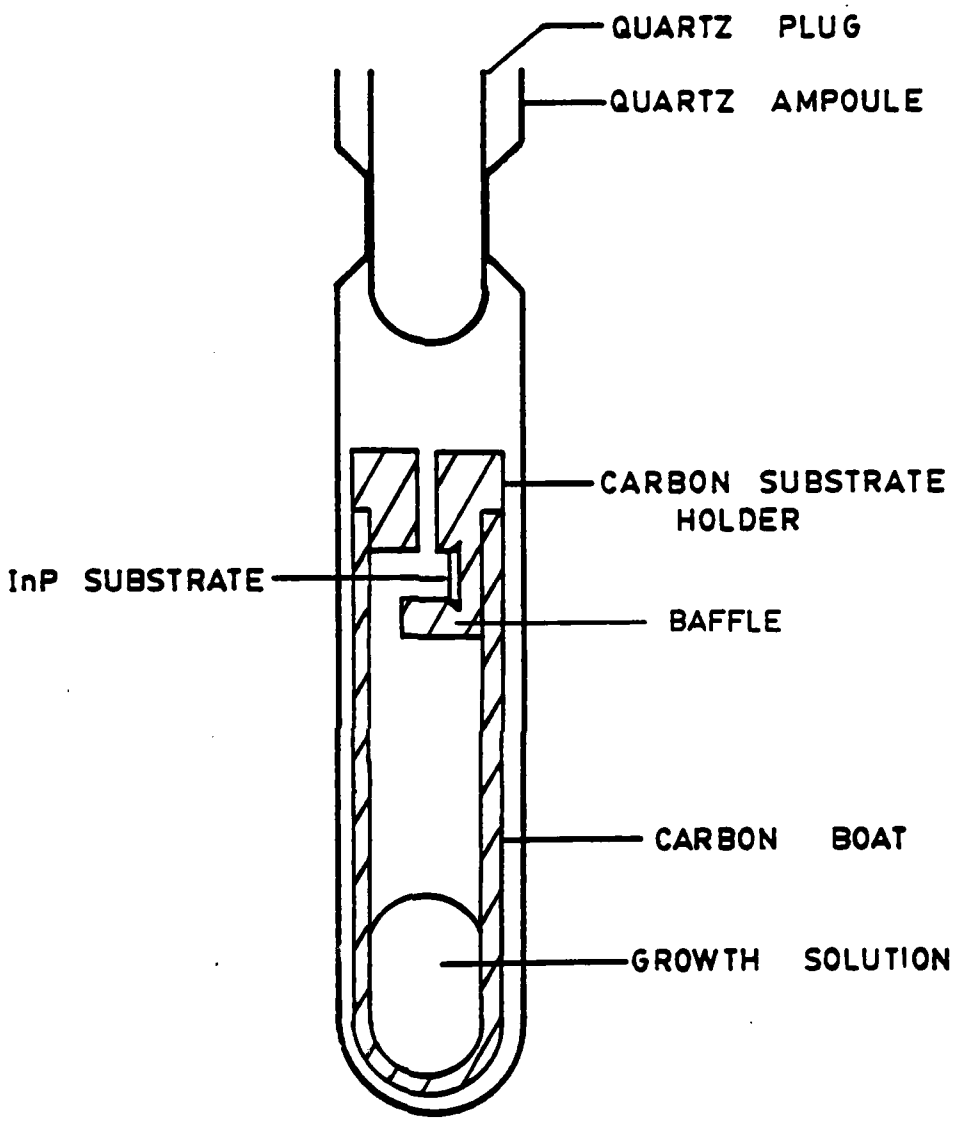

Figure 5 Schematic of sealed tube tipping LPE system.

to equilibrate for fifteen minutes. The furnace was then cooled to 510°C and rotated 180° so that the melt solution would flow over the substrate and out of the hole in the substrate holder as the furnace was cooled 10°C/hour. When the furnace had cooled to 360°C, it was tipped back to its original position and the ampoule was quenched. The separate homogenizing run, argon backfill, and the baffle on the substrate holder were all used to decrease the transport of volatile constituents from the melt to the substrate before melt contact was made. These constituents were found to cause severe pitting of the substrate.

The epitaxial growth produced in this manner was very rough with uneven interfaces. A typical cross section of a sample is shown in Figure 6. The epitaxial layers were generally 100 μm thick. No Hall measurements were made on these layers.

Because of the poor layer quality, little time was spent working with this system. Instead, an open tube H_2 flow system was designed and constructed for epitaxial growth. Such a system has several advantages over the closed tube system in that the apparatus and materials can be additionally purified, an *in situ* etch can be used, less materials are used in each growth run, and the growth runs are more easy to control over shorter times.

Figure 6 Cross-section view of sealed tube LPE sample after chemical-mechanical polishing with 1% bromine-methyl alcohol.

2.2.2 Open Tube Flow System

The open tube LPE system shown schematically in Figure 7 was designed and constructed. This system consists of a high purity graphite sliding boat with stationary melt wells and a slider with 0.015" deep substrate wells. This boat sat in a 40 mm O.D. quartz furnace tube through which purified hydrogen flowed. Between growth runs the system was baked out for four hours at 600°C with a flow rate of 120 ml/min.

The {100} InP substrates used in these experiments were chemically-mechanically polished on one side and their backs were lapped using 5 μm and 2 μm grit to a thickness of 400 μm. These substrates were then cleaned and etched as described above. The final chemical etch removed approximately 30 μm of material from the surface. The {111} and {211} InP substrates were prepared by lapping both faces to produce substrates 400 μm thick with parallel flat faces followed by cleaning in boiling organic solvents and a chemical etch for two minutes in 1% bromine-methyl alcohol. Substrates prepared in this manner would fill the substrate wells so that most or all of the growth solution could be removed after growth. All substrates used in these experiments were Fe-doped semi-insulating InP.

The LPE boat was loaded by placing the substrates in the substrate wells, positioning them between the

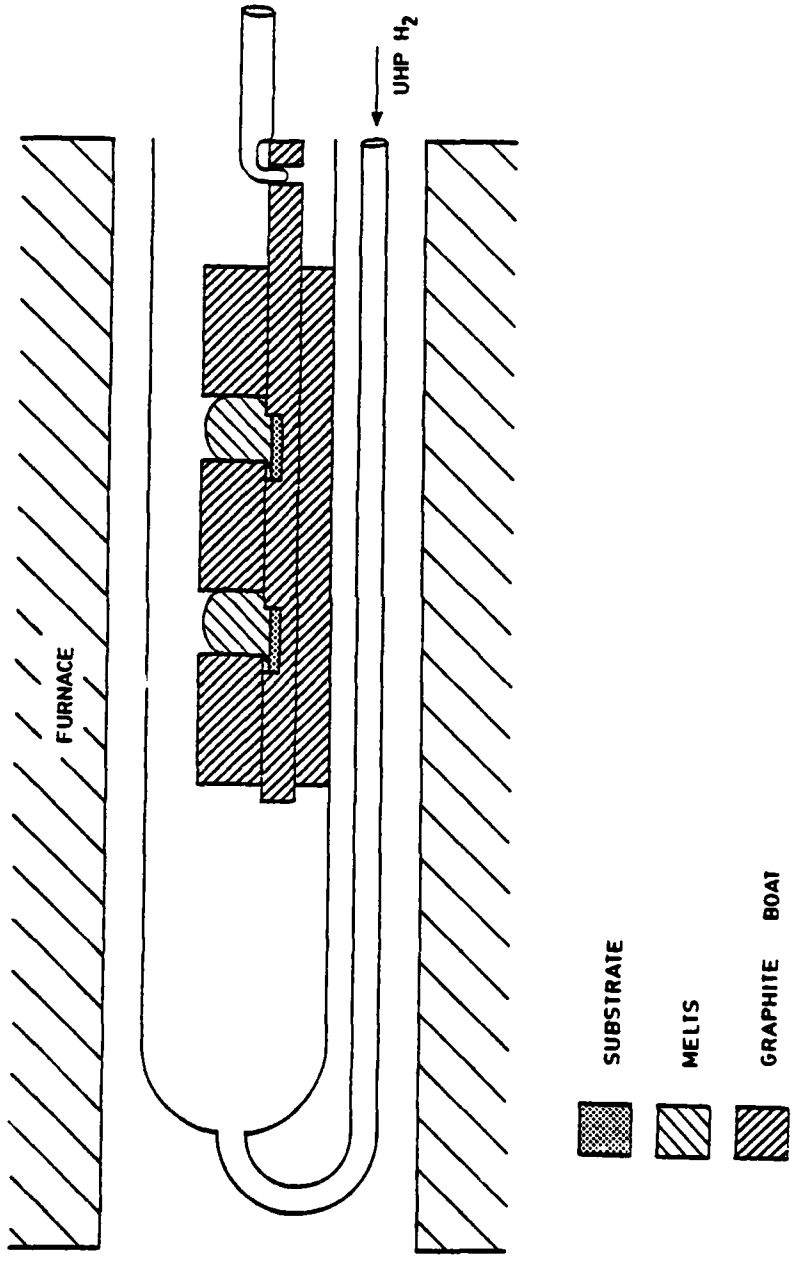

Figure 7 LPE sliding boat system.

melt wells, and then loading the melt wells with growth materials or etch materials. The boat was then loaded into the furnace tube and rapidly heated to the homogenization temperature. The melt was allowed to homogenize for one to two and a half hours and then cooled to the growth temperature: typically 20°C below the homogenization temperature. At this point the substrate was etched and moved to contact the growth solution. The furnace was then cooled at a constant rate: generally 5°C/hr or 10°C/hr. A twenty second etch of the substrate in pure Sn removed the top 5 μm of the surface and gave a much better surface for epitaxial growth than an unetched substrate. Such an etch was used in all of the growth runs except the initial few.

In the first forty-three growth runs the growth melt was made up of 99.999% purity ground red P_4, pellet Cd, and Sn shot with molar composition 15% P, 7% Cd, and 78% Sn. The homogenization temperature used was 540°C and the initial growth temperature varied between 490°C to 525°C, followed by a 10°C/hr cooling rate for four to ten hours. This procedure was discontinued because of the inability to consistently saturate the solution at a given temperature. This was due to loss of material from the melts before

the melts could be homogenized and during growth. Epitaxial material was grown in this system but this material was in the form of isolated single crystals and rough epitaxial layers. The best $CdSnP_2$ layer grown in this system is shown in Figure 8.

To better control the $CdSnP_2$ concentration in the melts so that the saturation temperature could be more accurately controlled, two changes in the procedure were made: First, a Cd_3P_2 source material was used in place of Cd and P_4 to allow for more complete dissolution of the source materials in the Sn solution. Second, the composition of Cd and P in the melt was reduced to lower the homogenization and initial growth temperatures and reduce the loss of volatile constituents from the melt.

The Cd_3P_2 source material was grown in a sealed tube system shown schematically in Figure 9. In this system a 25 mm O.D. 20 inch quartz ampoule was loaded with a boat of Cd pellets at one end, red P_4 at the other end, and sealed at a residual pressure of 3×10^{-6} torr. Stoichiometric amounts of Cd and P_4 were used with a slight amount of excess P_4 to provide a phosphorus overpressure in the ampoule. A total mass of 30 grams of the constituents was used per growth run. This ampoule was placed in a furnace and

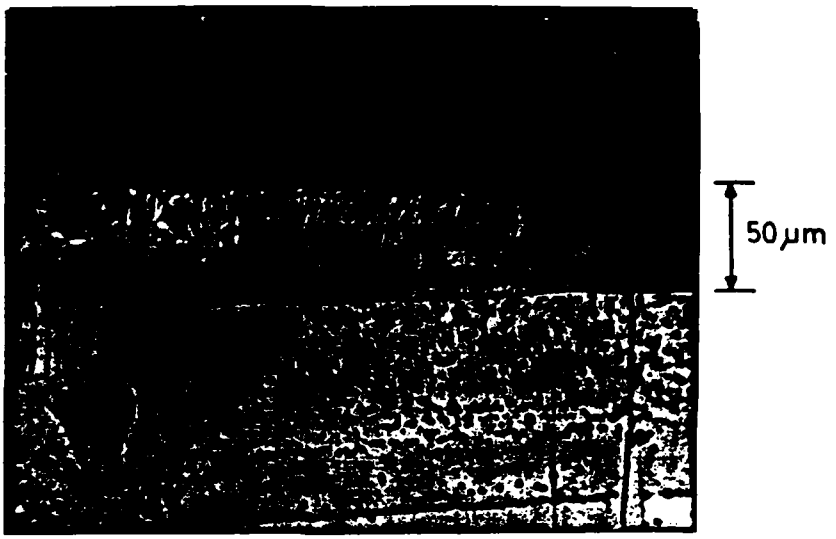

Figure 8 Cross-sectional view of $CdSnP_2$ layer grown from a solution of P_4 and Cd in Sn on {100} InP after chemical-mechanical polish.

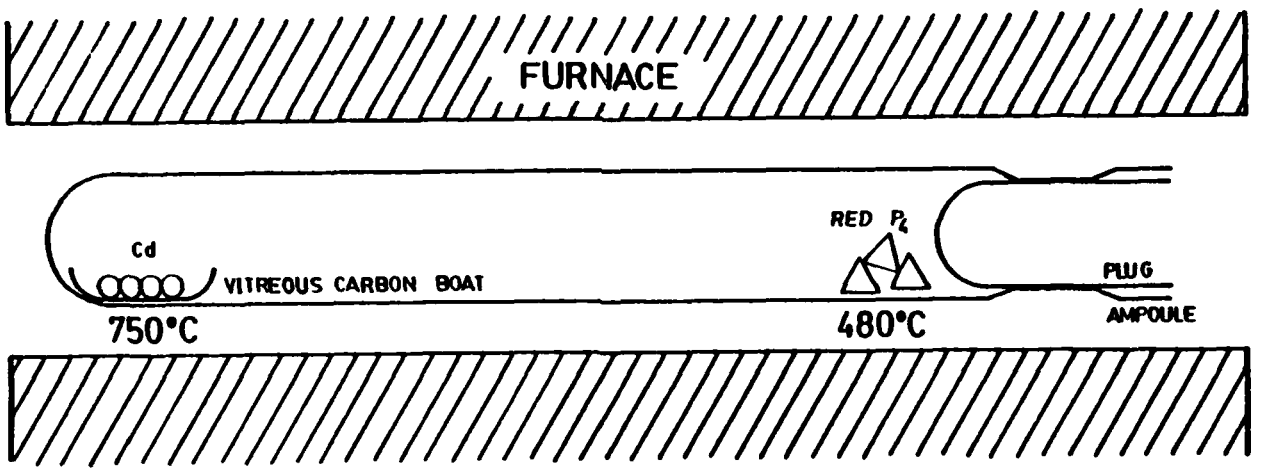

Figure 9 Schematic of sealed tube method for the growth of Cd_3P_2.

heated over eight hours with the cadmium at 750°C and the phosphorus at a mean temperature of 480°C. This cadmium temperature was chosen to be slightly above the melting point of Cd_3P_2 and the phosphorus temperature was used to give a phosphorus pressure of approximately two atmospheres in the ampoule. The ampoule was allowed to homogenize for 100 hours and was then cooled to room temperature. Cd_3P_2 growth was observed near the center of the ampoule in a region where the temperature had averaged 630°C. All of the cadmium and phosphorus had been consumed. Some of the Cd_3P_2 was in polycrystalline form adhering to the walls of the ampoule with large single crystals growing toward the center of the ampoule. These larger crystals were used for the source material.

Liquid phase epitaxial growth was resumed using a melt solution of molar composition 1.5% Cd_3P_2 and 98.5% Sn. The homogenization temperature was decreased to the 430°C to 455°C range with a two and a half hour homogenization time and the initial growth temperature was typically 420°C. Both 5°C/hour and 10°C/hour cooling rates were used with little effect on the growth. {100}, {111}, and {211} substrate surfaces were used and no preference for any orientation was observed. In these experiments the saturation temperatures were more stable although there were still some fluctuations.

At temperatures above 455°C excessive Cd and P loss from the melts was observed.

The layers grown in this manner again tended to have rough surfaces and dendritic growth. A typical layer is shown in Figure 10. Hall measurements on this material indicated that it was n type with a carrier concentration of 1 x $10^{18}cm^{-3}$ and a mobility of 200 cm^2/V-sec. The high temperature Hall measurements indicate that the poor material quality is due to depletion of volatile constituents from the melt.

X-ray diffraction measurements were made on some of the epitaxial layers and some of the data are plotted in Figures 11 and 12. The measurements indicated a mismatch of -0.4% to -0.6% as compared to calculated mismatches of -1.9% or +0.5% based on the lattice parameter measurements of Buehler *et al* [4]. The differences in measured and calculated values are probably due to differences in the growth techniques. The peak at -1.8% mismatch in Figure 12 is due to polycrystalline regions in that sample.

Figure 10. Cross section view of $CdSnP_2$ layer grown from a solution of Cd_3P_2 in Sn on {211} InP In face.

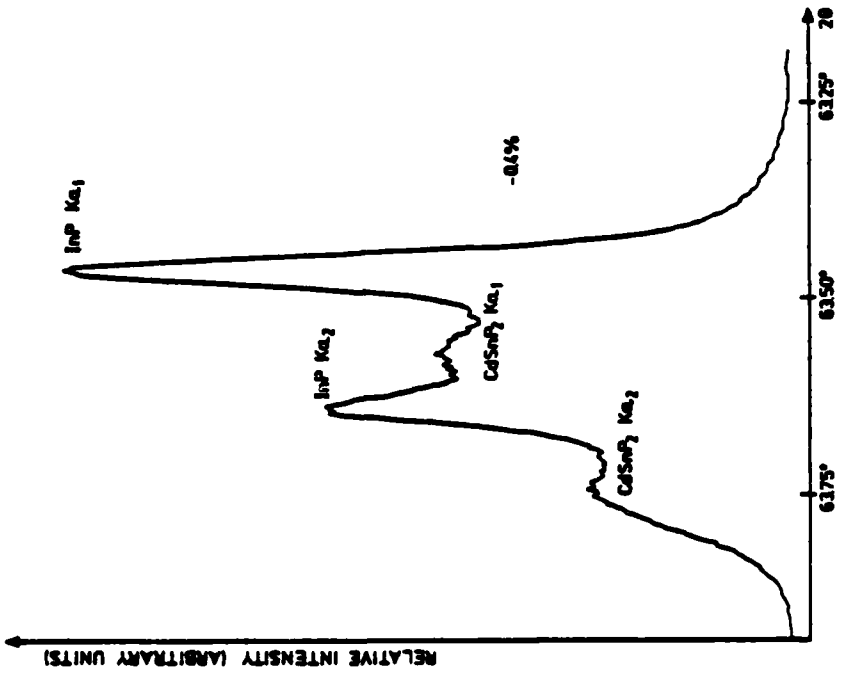

Figure 11 X-ray diffraction measurements for $CdSnP_2$ on {100} InP.

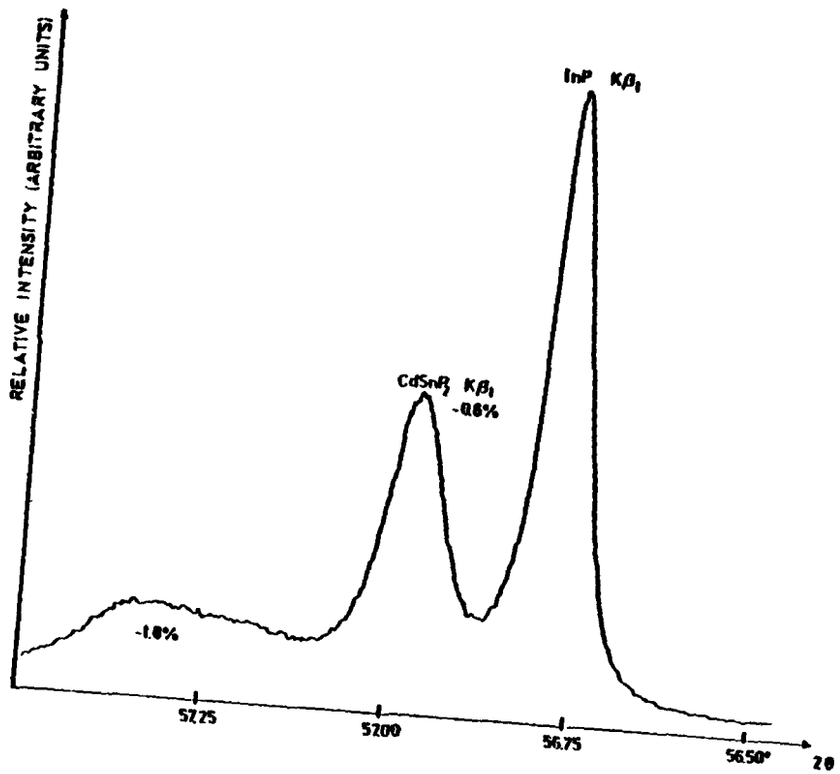

Figure 12 X-ray diffraction measurements for $CdSnP_2$ on {100} InP.

2.3 $Zn_xCd_{1-x}SnP_2$ GROWN ON InP

We believe that the poor quality of the layers grown with the previous systems can be attributed primarily to two factors: insufficient lateral mobility of the constituents at the growth surface and excessive lattice mismatch. The lateral mobility of the constituents can be increased by increasing their thermal energy: that is, by increasing the initial growth temperature. Because of the high rate of evaporation of constituents from the melt, several alterations were made to the system for higher temperature work. The lattice mismatch can be reduced by growing a suitable alloy of $CdSnP_2$ and another chalcopyrite so that the alloy lattice constant matches that of InP.

To minimize the number of system parameters, chalcopyrites differing from $CdSnP_2$ in only one constituent were reviewed for the alloy system. $ZnSnP_2$, $CdSiP_2$, and $CdGeP_2$ are all suitable choices for this purpose. $ZnSnP_2$ was chosen since the composition of the lattice matched alloy in this case is closer to $CdSnP_2$ than in the other alloys.

Since the chalcopyrites exhibit uniaxial compression it is not possible to lattice match both the a and c lattice constants simultaneously. Hence all growth experiments were performed using {100} oriented InP substrates so

that the a lattice constant could be matched with the c lattice constant extending normal to the growth interface. This type of growth could be anticipated from the x-ray measurements presented previously. Using Vegard's law, the composition of the alloy which should lattice-match InP is $Zn_{0.13}Cd_{0.87}SnP_2$.

2.3.1 Revised Open Tube System

The system shown schematically in Figure 13 was used for LPE growth of $Zn_xCd_{1-x}SnP_2$. This apparatus is identical to that of previous systems except for the graphite boat used. In the new boat the substrate well is in the base with the melt wells extending through the slider. During the melt homogenization process the slider melt wells are aligned with those in the top section and the substrate is covered by the graphite slider. This reduces the amount of volatile constituents transported to the substrat and reduces substrate pitting due to reactions with these constituents. To maintain a saturated solution during homogenization, excess source materials were added to the melt. This excess material floats at the top of the solution. To initiate growth the part of the growth solution contained in the slider is separated from the rest of the solution. This removes the excess source material before the melt is positioned over the substrate. In this position the growth solution is covered by the top of the graphite boat to reduce evaporation of the

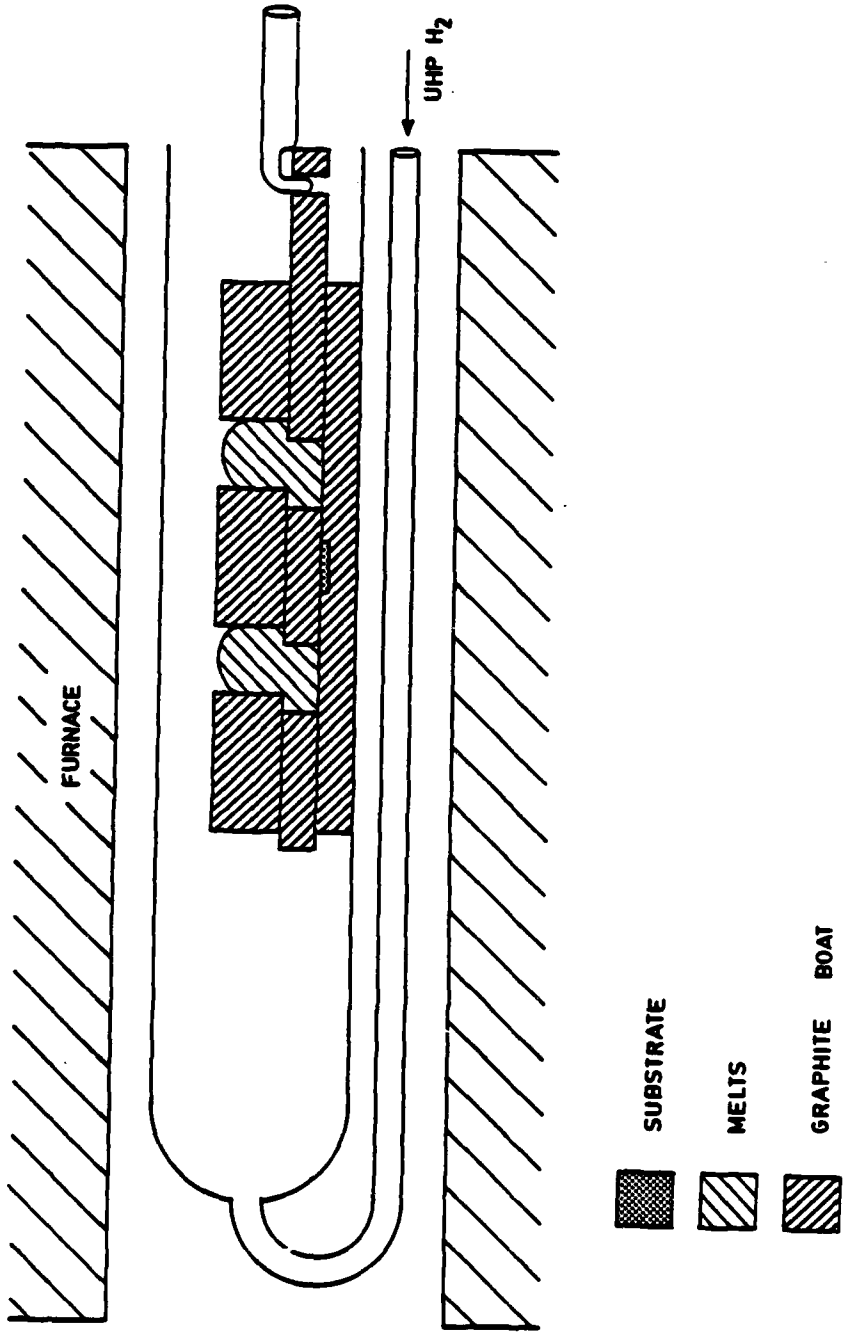

Figure 13 Schematic of LPE boat used to grow $Zn_xCd_{1-x}SnP_2$.

constituents. By using the apparatus in this manner the growth solution at the start of growth is saturated and the depletion of the melts by evaporation is reduced.

Because the vapor pressure of phosphorus is much higher than that of the other melt components, it is depleted from the melt faster. To compensate for this, it was decided to use separate sources of cadmium and phosphorus so that the initial phosphorus concentration in the melt could be increased. For this reason, elemental Cd and SnP_3 grown in a sealed tube system to be described, were chosen as sources of cadmium and phosphorus.

2.3.2 Sealed Tube Synthesis of SnP_3

SnP_3 was grown from elemental Sn and red P_4 using the apparatus shown schematically in Figure 14. It consists of a 20 mm I.D. x 25 mm O.D. x 9½ inch ampoule in which the Sn and P_4 are sealed after evacuation. These thick wall ampoules were required to withstand the high phosphorus pressures produced during growth. Prior to loading, the ampoules and sealing plugs were cleaned in aqua regia and boiling acetone and were then baked out under vacuum. Stoichiometric amounts of tin and phosphorus were used in each growth run with a few grams of excess phosphorus. A total mass of 20 grams were used per growth run. The ampoules were loaded and sealed at a residual pressure of 4×10^{-6} torr. The ampoules were placed into the furnace so that the Sn was in a 6 inch temperature zone

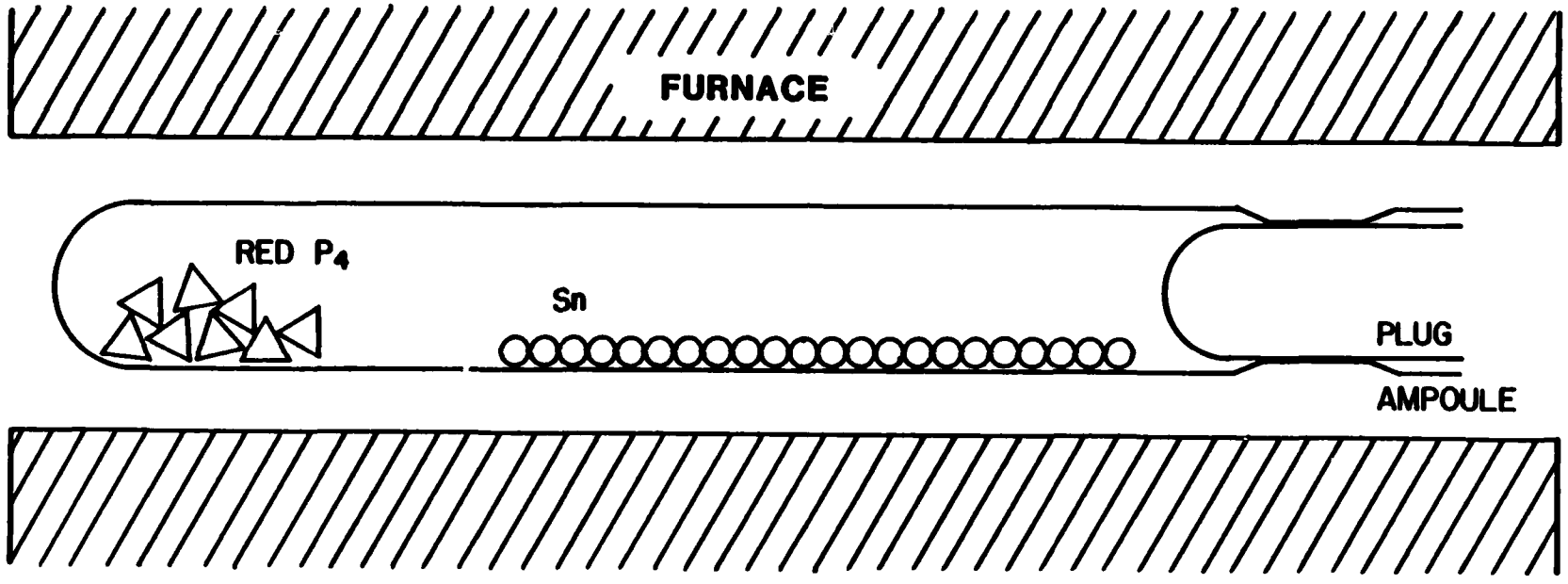

Figure 14 Apparatus used to grow SnP_3 source material.

flat to within 0.1° C; the total temperature variation over the ampoule being less than 2° C. The Sn was spread over a length of approximately 4 inches to give sufficient volume for the growth of the low density SnP_3. After loading an ampoule into the furnace it was heated to 500° C over a period of 24 hours. The system was allowed to homogenize for 100 hours and then was cooled to room temperature.

Upon removal from the furnace the ampoules were observed to contain SnP_3 and excess red and white P_4. The ampoules were opened in an argon atmosphere to prevent combustion of the phosphorus and the SnP_3 was decanted. Prior to use in the open tube epitaxial system, the SnP_3 was ground in a mortar and pestle to give material of a more convenient size. In some cases the SnP_3 was also cleaned in boiling organic solvents.

The stoichiometry of the SnP_3 was calculated from the initial mass of Sn and the mass of the product:

m_{Sn} = Mass of Sn loaded

m_{SnP_x} = Mass of product, composition SnP_x

M_{Sn} = Atomic mass of Sn = 118.69 gms/mole

M_P = Atomic mass of P = 30.9738 gms/mole

$$x = \frac{M_{Sn}}{M_P}\left(\frac{m_{SnP_x}}{m_{Sn}} - 1\right)$$

The values of x calculated in this manner averaged around 2.8 and were slightly smaller than the theoretical value due to loss of small amounts of the product during decanting.

2.3.3 $Zn-Cd-SnP_3-Sn$ System

Liquid phase epitaxial growth experiments were performed to grow the lattice-matched chalcopyrite alloy, $Zn_xCd_{1-x}SnP_2$, on {100} InP using the previously described apparatus. Elemental Zn, Cd, and Sn, all of 5N purity, and the synthesized SnP_3 were used as source materials for the system. The substrates used were generally Fe doped semi-insulating InP prepared as discussed previously with a few experiments performed on n type Sn doped substrates.

A typical growth run consisted of a one hour homogenization at 540° C, a second etch of the substrate in pure Sn, contact of the growth solution with the substrate, and cooling of the system at a linear rate of 5° C/hr. A typical melt charge consisted of 0.2254 gm of Cd, 0.3037 gm of SnP_3, 1.0000 gm of Sn, and 1.65 mg of Zn. The equivalent composition of such a melt is 19.85% $CdSnP_2$, 0.25% $ZnSnP_2$, 2.42% excess P, and 77.48% Sn. This gives a ratio of $ZnSnP_2$ to $CdSnP_2$ in the melt of 0.0125 which is about one tenth of the calculated ratio for the lattice matched solid. All growth experiments were carried out in an UHP H_2 atmosphere with a flow rate

through the tube of 30 ml/min. The cooling time for these experiments varied between 10 hours and 22 hours. A 10 hour cooling time gave between 1 μm and 2 μm of growth while a 22 hour time gave approximately 15 μm of growth for a 5° C/hour cooling rate.

A typical epitaxial layer is shown in Figure 15. This figure shows a fairly uniform epitaxial layer containing numerous pits which appear as dark regions in the surface view and as notches in the cross-sectional view. These pits were of variable depth and often extended through the epitaxial layer to the interface.

The morphology of the epitaxial layers is very dependent upon the system parameters. For an initial growth temperature of 530° C the growth was polycrystalline. A 10° C/hour cooling rate also gave polycrystalline material. A cooling rate of 4° C/hour would give no growth due to depletion of the melt by evaporation. The $ZnSnP_2$ to $CdSnP_2$ ratio in the melt is also fairly critical as can be seen in Figure 16. This figure shows cross sections of the epitaxial layers: one grown using the parameters given above; the other grown from a melt with a 6% larger Zn mass. The latter layer is polycrystalline. Values of growth parameters for optimum epitaxial growth in this system are summarized in Table 3.

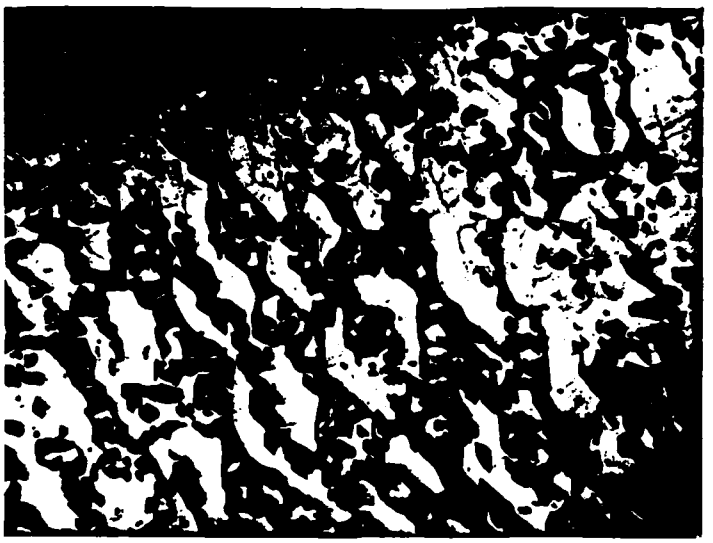

(a)

(b)

Figure 15 (a) surface and (b) interface of a typical $Zn_xCd_{1-x}SnP_2$ epitaxial layer grown on {100} InP.

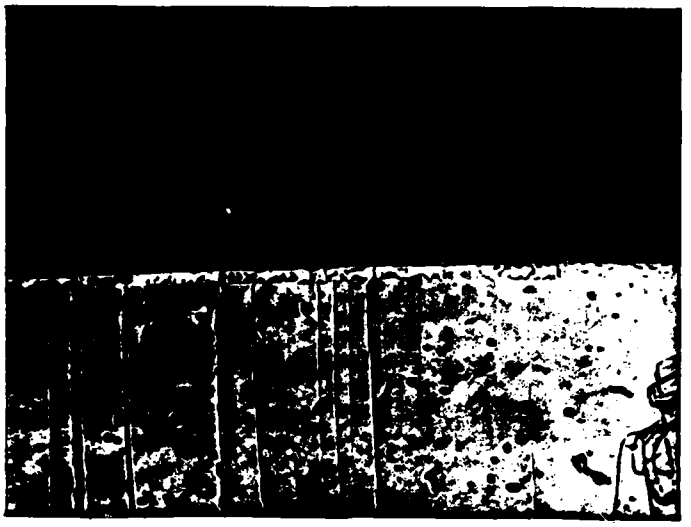

(a)

(b)

Figure 16 Epitaxial layers grown from
(a) a standard melt solution and
(b) a melt solution with a 6% larger Zn mass.

Table 3 Typical growth parameters for the Zn-Cd-SnP_3-Sn system.

SOURCE MATERIALS: Zn, Cd, SnP_3, Sn

Melt Composition

$CdSnP_2$	19.85	Molar %
$ZnSnP_2$	0.25	Molar %
Sn	77.50	Molar %
P	2.40	Molar %

$ZnSnP_2/CdSnP_2 \approx 0.0125$

Substrates: {100} Fe Doped InP

Homogenization Temperature: 540°C

Cooling Rate:	5°C/hour
Growth Duration:	10 to 22 hours
in situ Etch:	Pure Sn
Growth Atmosphere:	UHP H_2
Flow Rate:	30 ml/min

The morphologies of epitaxial layers grown in this system are greatly improved over those of the previous systems although still not suitable for device fabrication. The high segregation coefficient of $ZnSnP_2$ in $CdSnP_2$ suggests two possible impediments to growth of device quality epitaxial layers: Zn depletion from the melt due to its rapid incorporation into the growing layer and constitutional supercooling. Some experiments were performed in which we attempted to introduce a thermal gradient in the melt to relieve the problem of constitutional supercooling. This was done by placing the boat on a sealed chamber through which N_2 flowed to cool the bottom of the boat. It is not known whether or not this produced any thermal gradient in the melt. However, no substantial improvement in the epitaxial layers was observed. Another impediment to smooth layer growth may be the formation of antiphase boundaries. These boundaries are likely to form since the epitaxial material has a greater number of sublattices than the substrates. Possible solutions to this problem may be to grow on substrates oriented slightly off of the <100> direction or to grow on substrates of a higher index orientation. These experiments have not been performed.

2.3.4 Hall and Resistivity Measurements

Van der Pauw and Hall measurements were made for the layers grown on semi-insulating substrates with the results shown in Figure 17. All epitaxial layers were n type. Most had room temperature carrier concentrations around $10^{18} cm^{-3}$ and mobilities around 100 cm^2/V sec, similar to samples grown in previous systems. The resistivities were around 3×10^{-2} Ω cm. There are no substantial changes in these values for measurements made at 77 K. One layer had a mobility of 2000 cm^2/V-sec with a carrier concentration of 3×10^{19} cm^{-3}. The resistivity of this sample was 1×10^{-4} Ω cm. This sample is of interest because the mobility is about twice that which can be obtained for equivalent III-V compounds at similar carrier concentrations. This sample indicates one potential advantage of the low effective mass II-IV-V_2 chalcopyrites over the III-V sphalerite semiconductors: that is, higher mobilities can be achieved at similar carrier concentrations.

The solid line in Figure 17 shows the theoretical dependence of the mobility on the carrier concentration for scattering from ionized impurities with screening. This curve was calculated from the Brooks-Herring model for ionized impurity scattering [7] using degenerate statistics for the high carrier concentrations. The concentration of ionized impurities, N_I, in this model was

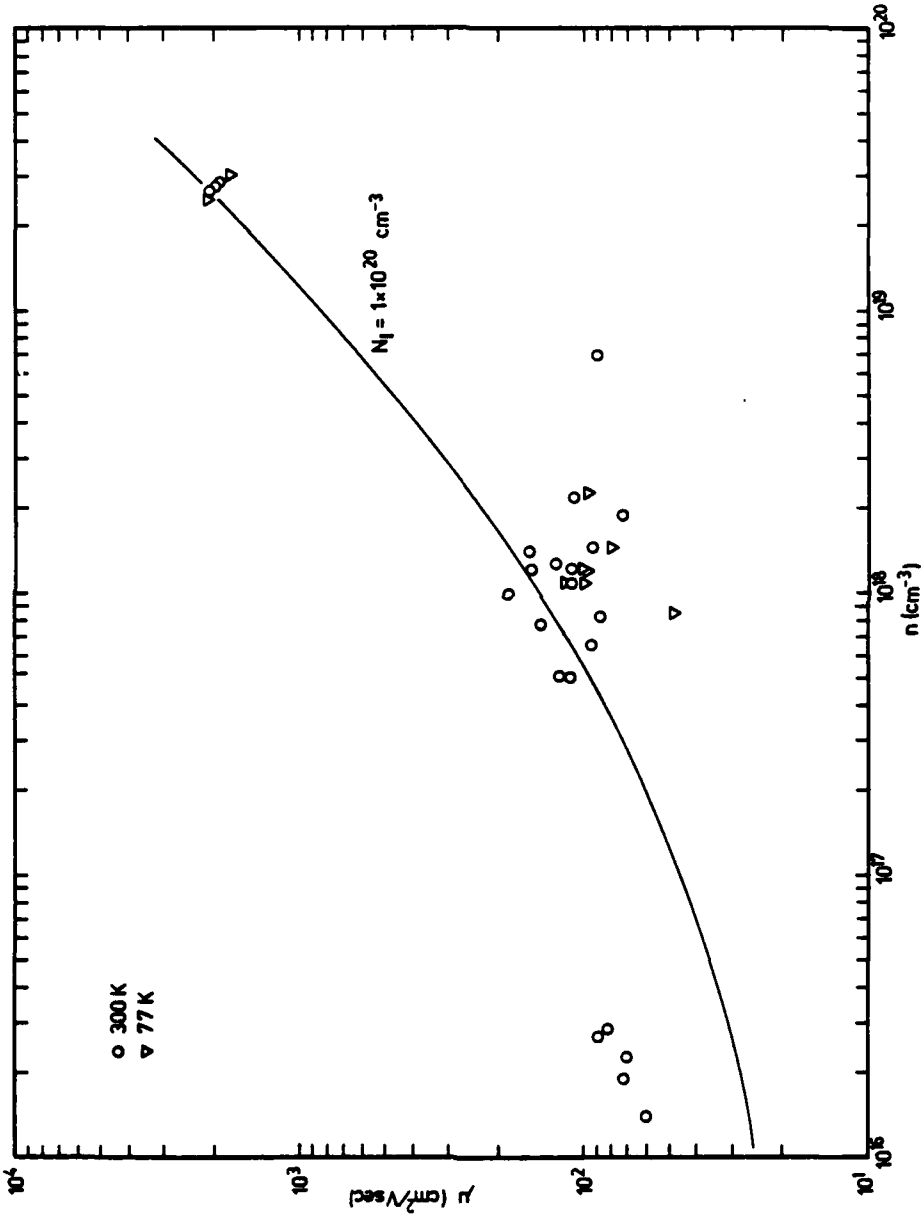

Figure 17 Mobility, μ, vs. carrier concentration, n, for $Zn_xCd_{1-x}SnP_2$ epitaxial layers.

used as an adjustable parameter which was set so that the curve matched the high mobility data points. The value of N_I obtained in this manner was $N_I = 1 \times 10^{20} cm^{-3}$. As can be seen, there is reasonable agreement between the experimental data and the theoretical curve. This indicates that the observed decrease in mobility with decreasing carrier concentration is mostly due to close compensation.

Because high conductivity inhomogeneities in an epitaxial layer can give anomalously high calculated mobilities [8], further experiments were performed on the high mobility sample to determine whether the mobility value was real. First, this sample was cleaved into four pieces and the pieces were remeasured. The effects of a conducting inhomogeneity on the resistivity and Hall measurements can usually be eliminated with this procedure. The mobilities and carrier concentrations of each piece, however, were very close to those of the original sample. This can be seen from the tight grouping of the data in the high concentration region of Figure 17. To further substantiate these data, measurements of the Hall constant as a function of magnetic field were performed. These results are plotted in Figure 18, where a decrease in the Hall constant with increasing magnetic field is shown. This behavior is typical of homogeneous n-type material. If there had been a conducting inhomogeneity, such as those which give an anomalously high apparent mobility,

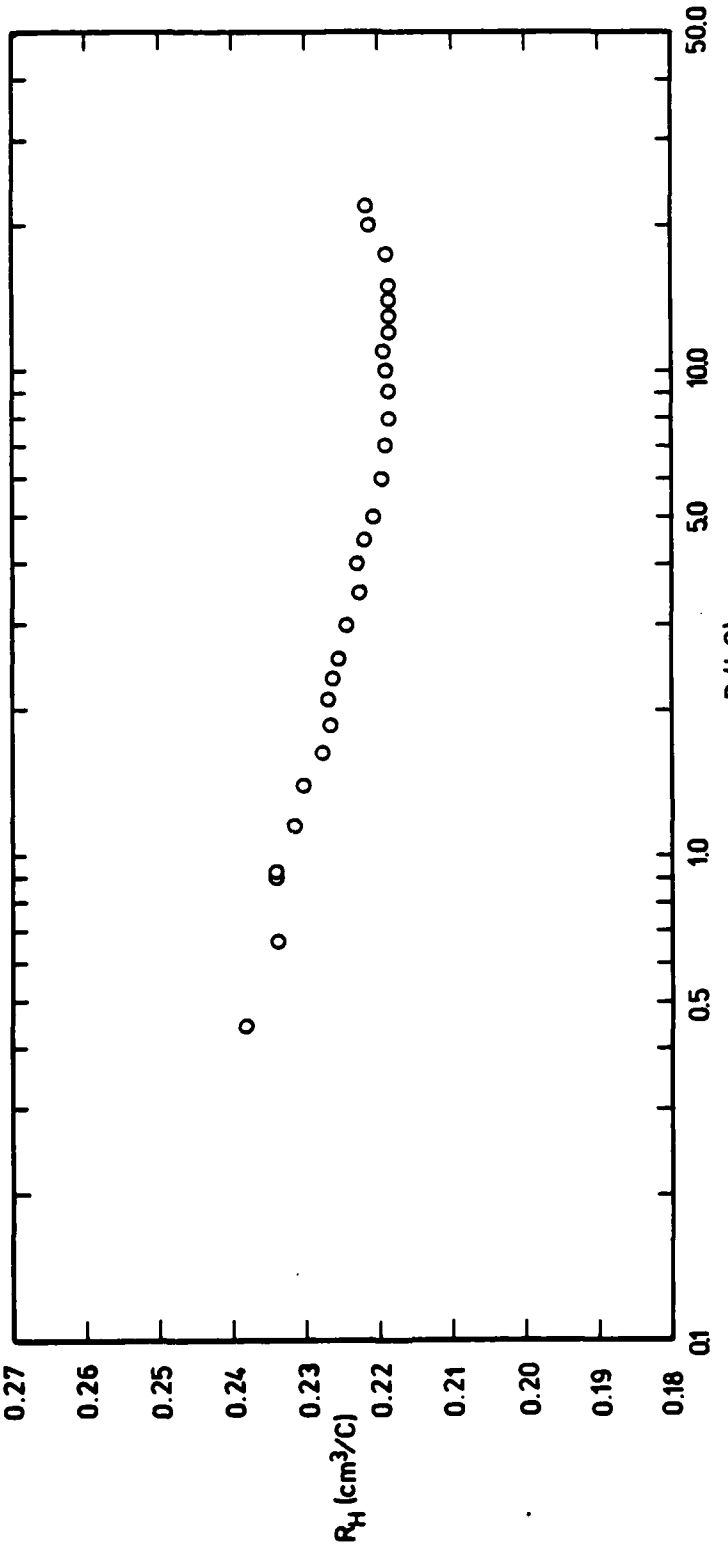

Figure 18 Measured Hall constant as a function of magnetic field.

the Hall constant would have increased with increasing magnetic field. Thus, the mobility and carrier concentration of this epitaxial layer are apparently not due to inhomogeneity effects and appear to be an accurate indication of the high mobility which can be attained in this material.

The high ionized impurity concentrations in these samples is probably due to loss of volatile constituents from the epitaxial layers during growth. This is supported by the results of the high temperature Hall measurements made on the platelets, which showed a decreased mobility and increased carrier concentration with annealing time. Thus, annealing the samples in a phosphorus or phosphorus and cadmium overpressure should give increased mobilities and decreased carrier concentrations as N_I is reduced. Such experiments are an appropriate subject for future investigation.

2.4 $ZnSnP_2$ GROWN ON GaAs

2.4.1 Zn-SnP_3-Sn System

Liquid phase epitaxial growth of $ZnSnP_2$ on GaAs was performed in the revised open tube system described in Section 4.1. The source materials used were 5N Sn and Zn and SnP_3 synthesized as described in Section 4.2. Growth experiments were performed using initial growth temperatures between 530°C and 640°C with linear cooling rates between

1°C/hr and 5°C/hr. The growth periods ranged from 6 to 18 hours.

For cooling rates of 5°C/hr the grown layers were thin (<5μm) and solid material was observed in the growh solutions at the end of the growth runs. This suggests that this cooling rate is too large to allow the melt constituents to propagate to the growing surface, resulting in supersaturation and crystal nucleation in the melt. For cooling rates of 1.0°C/hr and 1.5°C/hr the layers were thicker (5μm to 35μm) and no solid material was found in the growth solutions at the ends of the runs.

The melts used for the growth experiments had equivalent $ZnSnP_2$ concentrations ranging from 1% to 2% with slight (≲0.2%) excess P concentrations. Figure 19 shows the dependence of the initial growth temperature on equivalent $ZnSnP_2$ concentration in the melt for saturated or slightly supersaturated melts. All growth runs were performed in an UHP H_2 atmosphere at a flow rate of 30 ml/min. At this flow rate and temperature range it was found that the loss of phosphorus from the melt was not nearly as much of a problem as it was in the $Zn_xCd_{1-x}SnP_2$ ($x \simeq 0.125$) growth system. Consequently, the growth experiments were much more reproducible even at small cooling rates. Melt homogenizations of 1 to 2 hours at the initial growth temperature were used. Between growth runs the system was baked out for a minimum of 3 hours at 850°C.

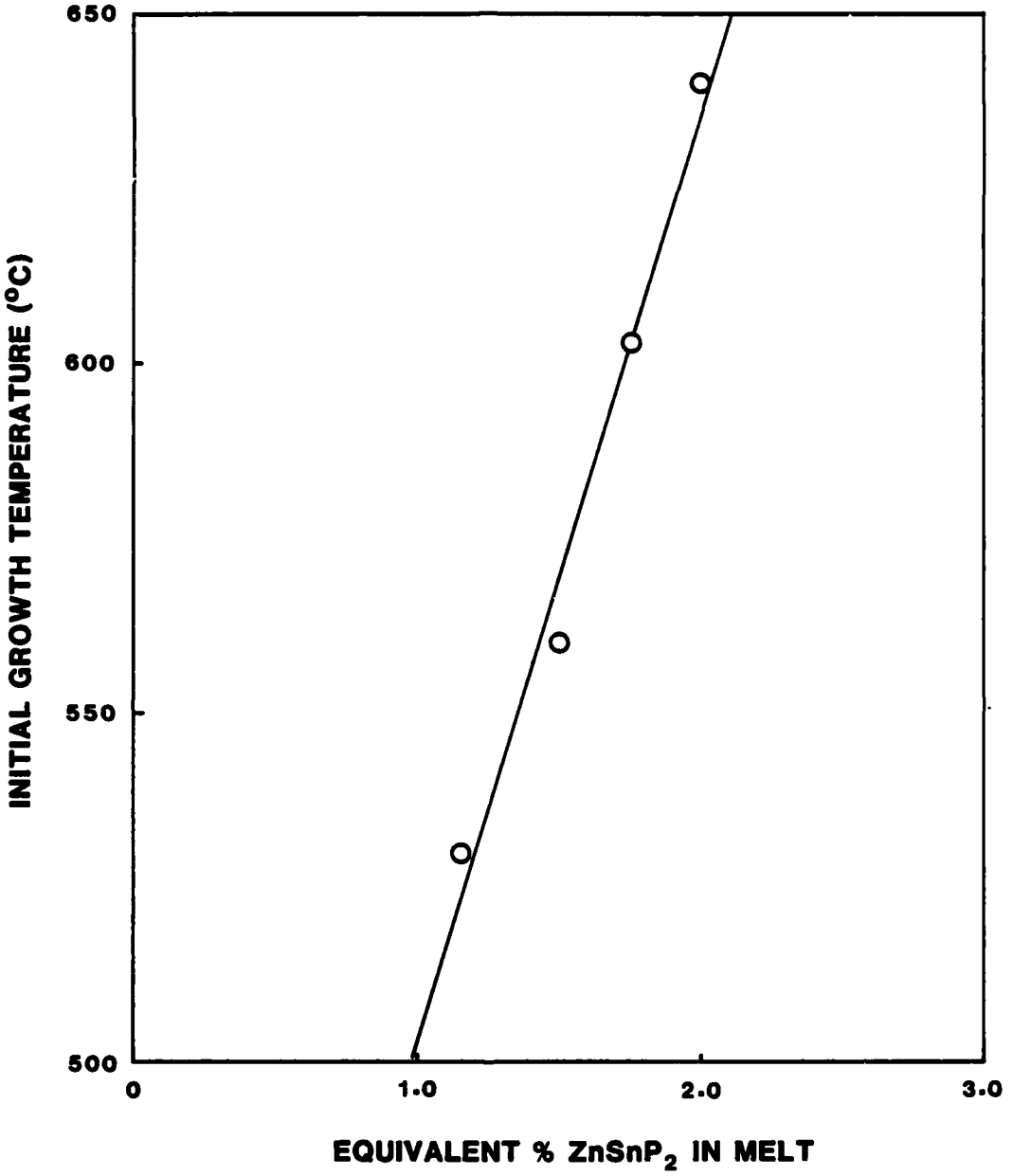

Figure 19 Initial growth temperature as a function of $ZnSnP_2$ concentration for slightly supersaturated solutions.

Initial growth experiments were performed on {100}, {110}, {111}, and {211} oriented substrates to determine the optimum orientation for growth. Typical growth on these orientations are shown in Figures 20, 21, and 22. All substrates were prepared as described previously except for the final chemical etch. The final 5:1:1 H_2SO_4:H_2O_2:H_2O etch cycle consisted of a 10 min. cool-down followed by a 2 to 4 min. etch.

{100}, {211}, and {111} Ga oriented substrates produced growth which was quite rough and generally unsuitable for electrical measurements. {110} and {111} As oriented substrates had rough interfaces but uniform surfaces with very good morphologies. This is consistent with the observation of predominant {111} facets in solution grown platelets [6] and with experiments in which we have observed low growth rates in the {111} direction. Layers grown on {110} oriented substrates revealed much better interfaces but had surfaces with more structure and tended to be of non-uniform thickness. Because of this the majority of latter growth experiments were performed using {111} As oriented substrates.

All layers grown on {110} and {111} As oriented substrates had a few small patches of Sn adhering to their surfaces. These were removed by ultrasonic cleaning in a solution of mercuric chloride in dimethyl formamide. This is in contrast to the layers of $Zn_xCd_{1-x}SnP_2$ grown on {100} InP and the layers of $ZnSnP_2$ grown on other substrate orientations which were found to be completely covered with a Sn layer upon removal from the LPE boat.

(a)

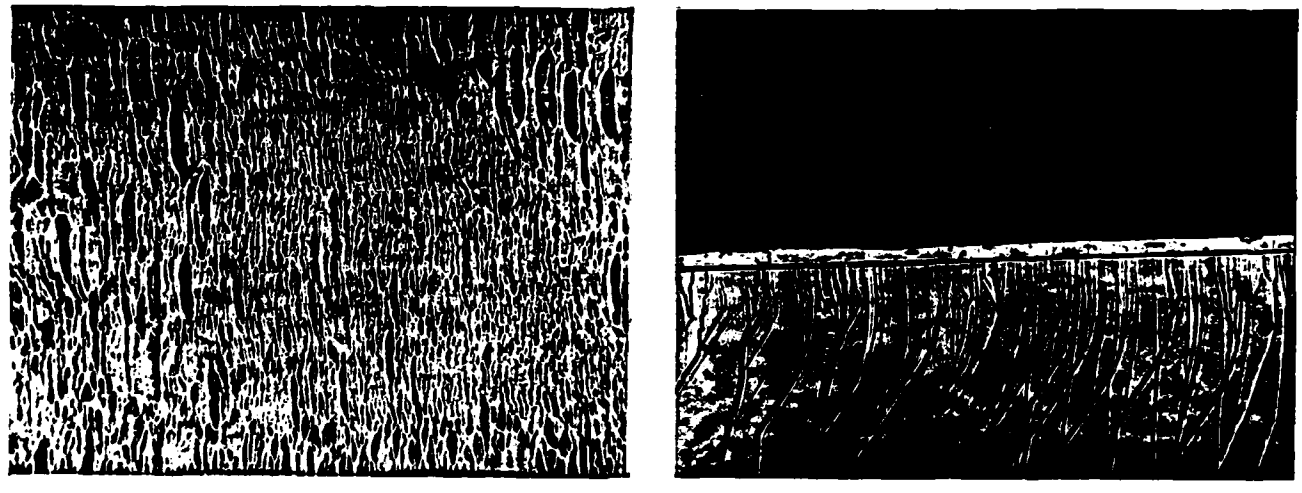

(b)

Figure 20 Surface (220x) and cross-sectional (450x) views of typical $ZnSnP_2$ growth on (a) {100} oriented GaAs and (b) {110} oriented GaAs. The {110} oriented layer is 4 μm thick.

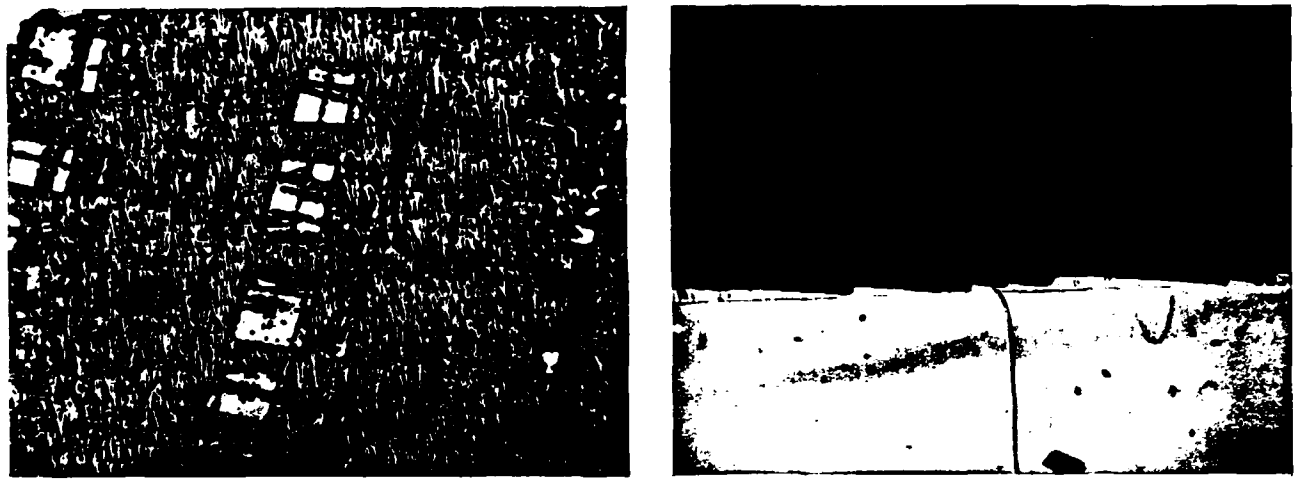

(a)

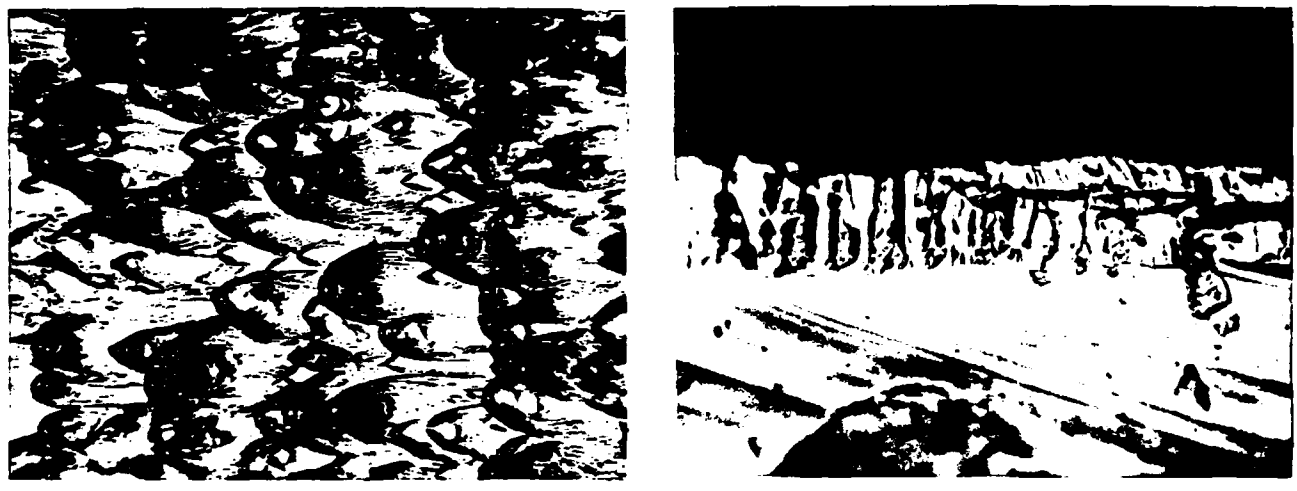

(b)

Figure 21 (a) Surface (220x) and cross-sectional (450x) views of $ZnSnP_2$ growth on {211} Ga oriented GaAs.

(b) Surface (110x) and cross-sectional (450x) views of a 40 μm $ZnSnP_2$ layer grown on {211} As oriented GaAs.

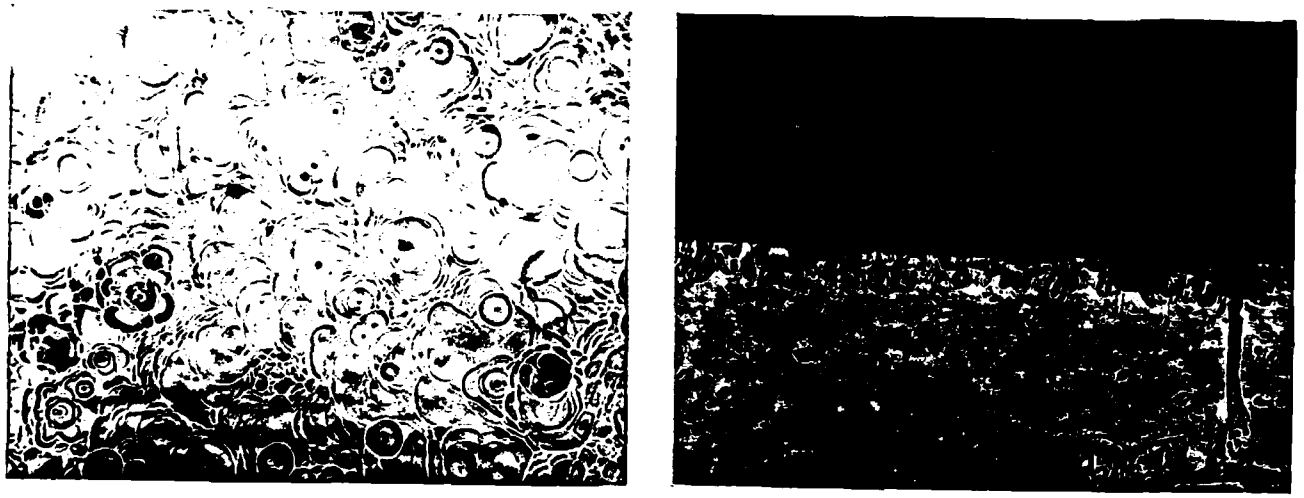

(a)

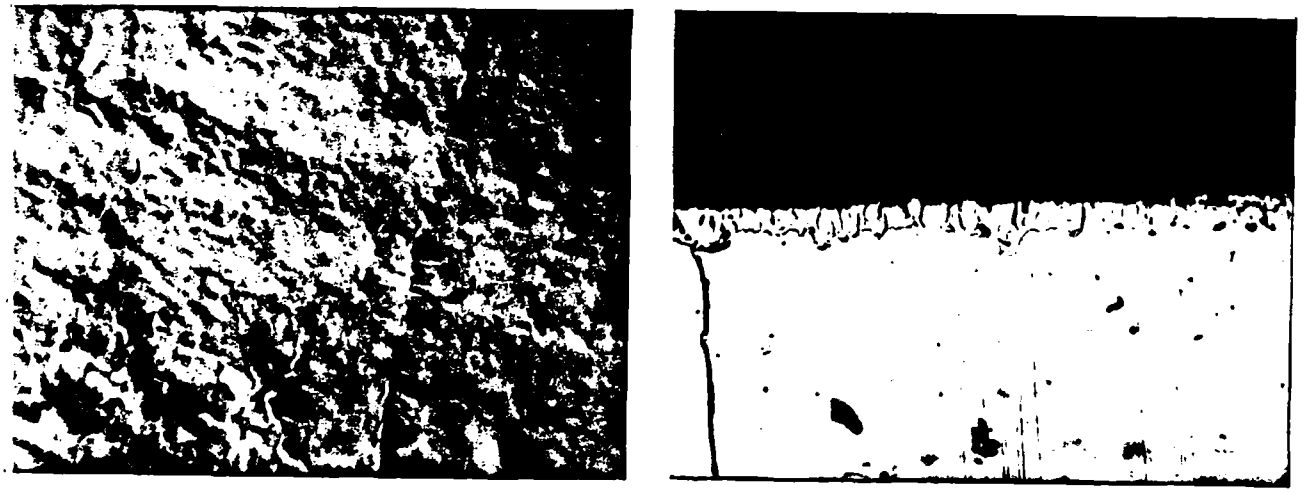

(b)

Figure 22 Surface (220x) and cross-sectional (450x) views of typical $ZnSnP_2$ layers grown on (a) {111} Ga oriented GaAs and (b) {111} As oriented GaAs. Both layers are about 5 μm thick. The structure of the surface view (b) was enhanced using a Nomarski interferometer.

For {111} As oriented substrates the best growth was obtained using an initial growth temperature of 560°C with a cooling rate of 1°C/hr, the smallest cooling rate used in these experiments. The melts for these growth runs had an equivalent $ZnSnP_2$ concentration of 1.4% to 1.5% with one gram of Sn used per run. For initial growth temperatures below 530°C no layers could be grown and for initial growth temperatures above 600°C the morphologies and electrical characteristics of the layers degraded although layers could be grown. This may be due to stoichiometric defects in the layers probably due to phosphorus loss. The grown layers were generally 5 μm to 15 μm thick except those grown at high temperatures which were up to 30 μm thick.

2.4.2 Hall and Resistivity Measurements

Van der Pauw resistivity and Hall measurements were made on the grown layers. All layers were found to be p type with carrier concentrations ranging from $1x10^{18}cm^{-3}$ to $1x10^{21}cm^{-3}$ and calculated mobilities ranging from $10cm^2/Vsec$ to $70cm^2/Vsec$. The resistivities of these layers ranged from $2.5x10^{4}\Omega cm$ to $1.2x10^{-1}\Omega cm$. A plot of carrier concentration as a function of inverse initial growth temperature is shown in Figure 23. The graph reveals a general increase in carrier concentration with increased initial growth temperature. The straight line interpolated through this data suggests that the stoichiometric defects which are thought to cause the high carrier concentration have an activation

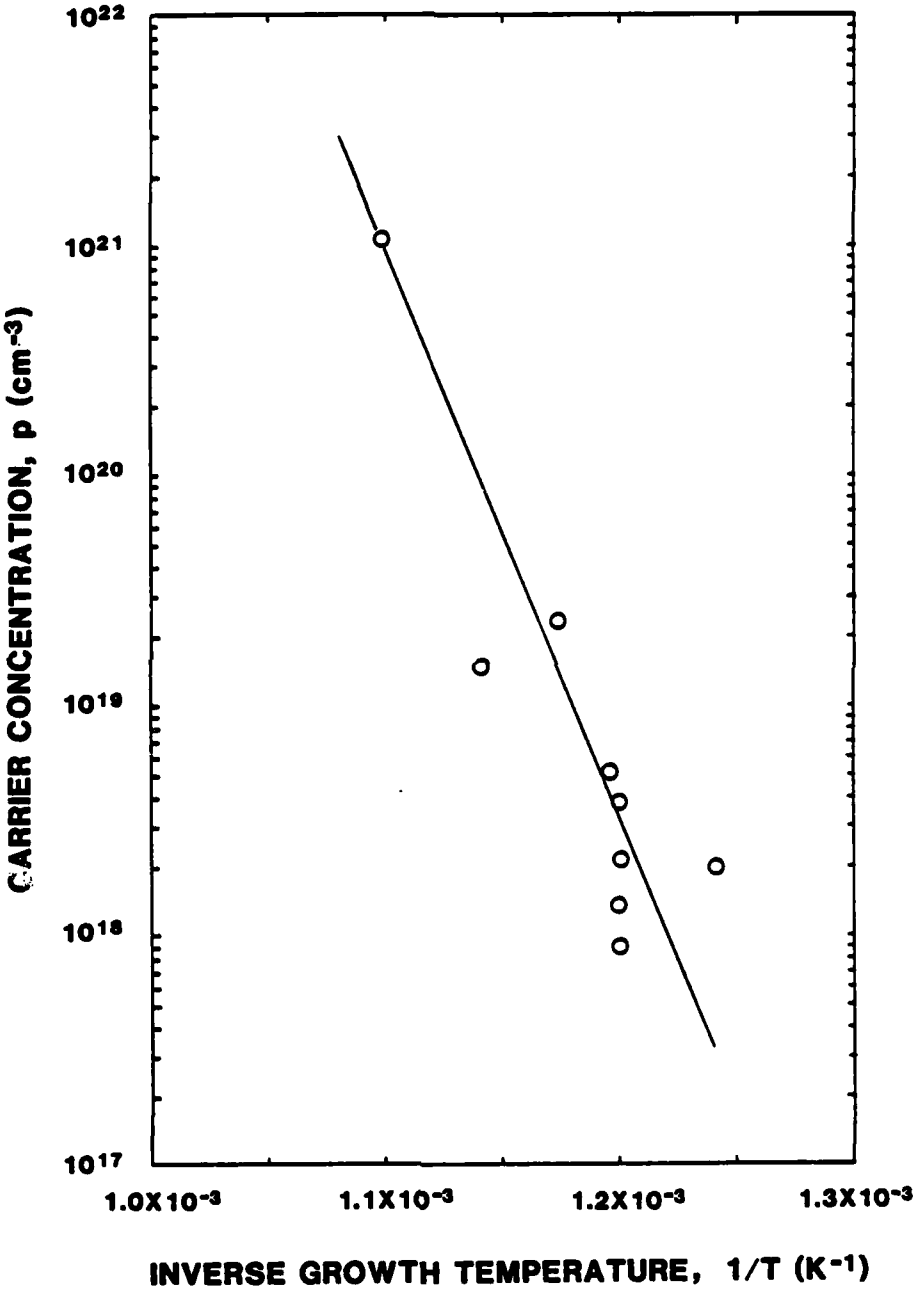

Figure 23 Carrier concentration of epitaxial layers versus inverse initial growth temperature.

energy of about 5eV. Only slight changes in these data were observed between 300K and 77K measurements.

A few experiments were performed in which Column VI dopants were added to the growth melts in an attempt to make the layers n type. Addition of as much as 0.133 mg of Te to the ≃ 1 gm melts had no noticeable effect on the electrical characteristics. This may be due to a large segregation coefficient of Te in this system. Doping experiments are an appropriate subject for future research since the usefulness of $ZnSnP_2$ as an electronic material depends on the ability to make it p and n type.

2.4.3 X-Ray Diffraction Measurements

X-ray diffraction measurements were made on the layers grown on {111} As oriented GaAs using a double crystal diffractometer aligned for the GaAs 333 reflection for Cu Kα radiation. Peak widths at half peak intensity of 10 seconds of arc were reproducibly obtained with {111} GaAs used for growth substrates. Some results of these measurements are shown in Figures 24 and 25.

Most of the samples measured revealed a single broadened GaAs peak with some slight background reflection as seen in Figure 24. This suggests that the epitaxial material lattice matches GaAs to within 5×10^{-3}% based on a 10 second resolution. The FWHM peak widths ranged from 45 seconds to 85 seconds. The low intensity background reflection may be due to the rough interface or strain incorporated in the layers.

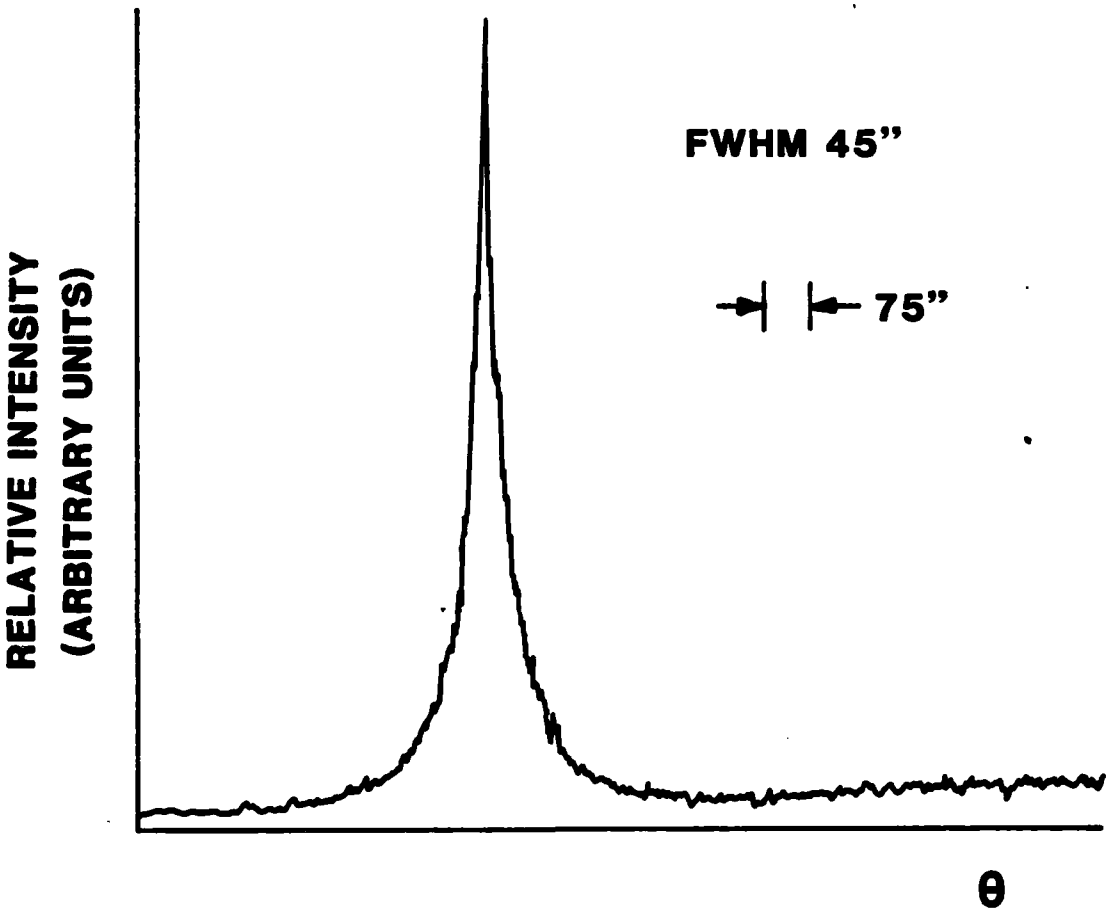

Figure 24 Typical double crystal x-ray diffraction scan for $ZnSnP_2$ on {111} GaAs.

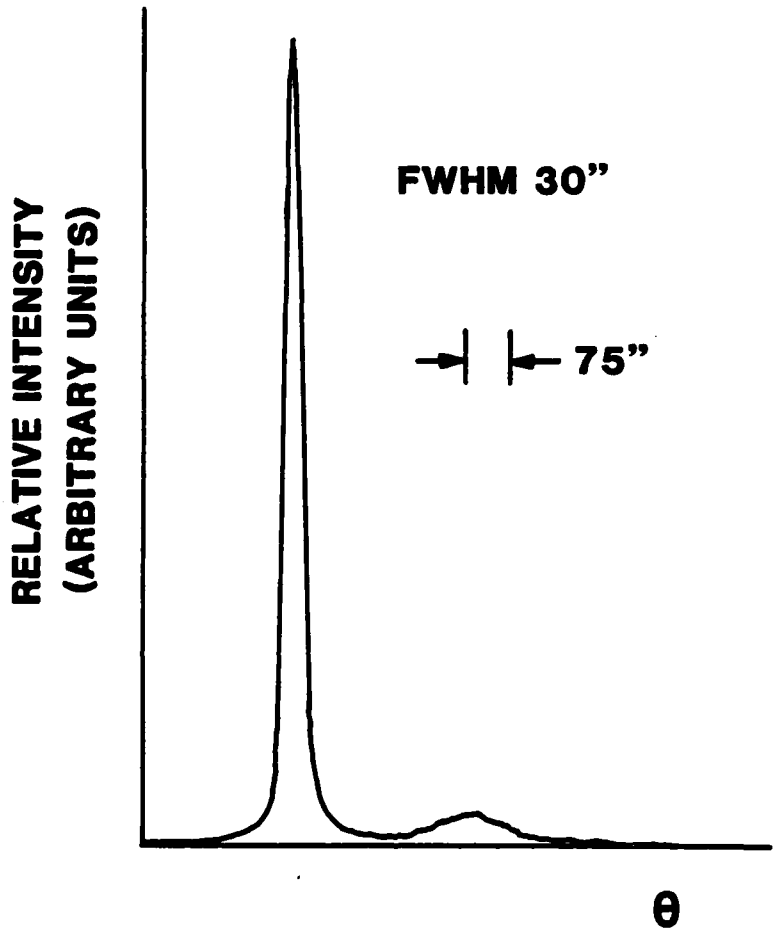

Figure 25 Double crystal x-ray diffraction scan of $ZnSnP_2$ layer grown on {111} GaAs with a cooling rate of 5°C/hr.

Some of the thinner layers revealed a secondary peak at about one tenth of the intensity of the main peak separated by 4.9 minutes of arc as seen in Figure 25. These layers were 3 μm thick and were grown using a 5°C/hr cooling rate. The layers had much smoother interfaces than those grown using smaller cooling rates and no broad background x-ray intensity was observed. The lattice constant of the layers calculated from these data is 5.645 Å which is 0.1% smaller than the 5.651 Å lattice constant observed by other researchers on solution grown platelets [6,9]. The FWHM peak widths of the main peaks were 20 to 30 seconds and those of the secondary peaks were around 120 seconds.

2.5 CONCLUSIONS

Several methods for the growth of $CdSnP_2$ platelets and epitaxial layers on InP have been presented. Work with these systems suggests that the lattice mismatch of $CdSnP_2$ on InP is a significant impediment to the liquid phase growth of device quality epitaxial layers.

Liquid phase growth of the chalcopyrite alloy, $ZnCd_{1-x}SnP_2$ was investigated as a method for obtaining device quality epitaxial layers. This alloy should have physical properties close to those of $CdSnP_2$ with the advantage of being lattice matched to {100} InP. An open-tube LPE system was used to obtain epitaxial layers of the alloy which were smoother than the $CdSnP_2$ grown with previous systems. The morphology of the $Zn_xCd_{1-x}SnP_2$ layers, however, was still not of device quality. A sample having a mobility of

2,000 $cm^2/Vsec$ with a carrier concentration of $3x10^{19}cm^{-3}$ was produced using this system. This suggests that it may be possible to effectively utilize the low electron effective mass of this material.

A method for the growth of $ZnSnP_2$ epitaxial layers on GaAs has been discussed. This growth was studied due to the small lattice mismatch between the materials and because the $ZnSnP_2$ structure is amenable to growth on high index orientations. The optimum orientations for growth were found to be {110} and {111} As. The $ZnSnP_2$ layers had improved morphologies over the $CdSnP_2$ and $Zn_xCd_{1-x}SnP_2$ ($x\simeq0.125$) growth.

2.6 REFERENCES

1. V.V. Podol'skii, I.A. Karpovich, and B.N. Zvonkov, "Hall Mobility of Electrons in $CdSnP_2$ Single Crystals", *Soviet Physics of Semiconductors* 10, No. 5, 594, (1976).

2. N.A. Goryunova, E.I. Leonov, V.M. Orlov, A.F. Rodionov, V.I. Sokolova, and V.P. Sondaevskii, "On Some Properties of $CdSnP_2$ in Strong Electric Field", *Physics Letters* 31A, No. 7, 393, (1970).

3. S. Knight, E. Buehler, and I. Camlibel, "Current Controlled Negative Resistance in $CdSnP_2$", *Journal of Applied Physics* 43, No. 8, 3422, (1972).

4. E. Buehler and J.H. Wernick, "The CdP_2-Sn System and Some Properties of $CdSnP_2$ Crystals", *Materials Research Bulletin* 6, 303, (1971).

5. J.L. Shay, K.J. Bachman, and E. Buehler, "Preparation and Properties of $CdSnP_2$/InP Heterojunctions Grown by LPE From Sn Solution", *Journal of Applied Physics* 45, No. 3, 1302, (1974).

6. J.L. Shay and J.H. Wernick, "Ternary Chalcopyrite Semiconductors: Growth, Electronic Properties, and Applications", Pergamon Press, Elmsford, New York, (1975).

7. Albert C. Beer, "Galvanomagnetic Effects in Semiconductors", Academic Press, New York, New York, (1963).

8. C.M. Wolfe, G.E. Stillman, and J.A. Rossi, "High Apparent Mobility in Inhomogeneous Semiconductors", *Journal of the Electrochemical Society* 119, No. 2, 250, (1972).

9. A.A. Vaipolin, N.A. Goryunona, L.I. Kleshchinskii, G.V. Loshakova, and E.O. Osmanov, "The Structure and Properties of the Semiconducting Compound $ZnSnP_2$", *Phys. Stat. Sol.* 29, 435, (1968).

3. VAPOR PHASE EPITAXIAL GROWTH OF $ZnGeAs_2$

$ZnGeAs_2$ crystallizes in the chalcopyrite structure which has tetragonal symmetry. It can be viewed as two stacked zincblende unit cells as illustrated in Figure 1. $ZnGeAs_2$ may be considered as an isoelectronic analog of GaAs in which the Ga is replaced by equal proportions of Zn and Ge to give, on an average, the same total number of bonding electrons per atom. In addition, the a lattice constant of $ZnGeAs_2$ (5.671Å) is close to that of GaAs, and epitaxial growth of $ZnGeAs_2$ on {100} GaAs should produce a lattice mismatch of about 0.32%. The close structural similarity and small lattice mismatch suggest that the growth of epitaxial layers of $ZnGeAs_2$ on GaAs surfaces is feasible.

$ZnGeAs_2$ has previously been grown in bulk form. The large solid solubility of Ge in this material and the high melting point of Ge tend to preclude the use of liquid epitaxy to grow $ZnGeAs_2$. Vapor phase techniques, however, have been applied with great success to the epitaxial growth of III-V compounds. The objective of this part of the work is to attempt to grow $ZnGeAs_2$ epitaxially on GAs with a VPE open tube flow system.

(a) Two GaAs zincblende cubic unit cells

(b) One $ZnGeAs_2$ chalcopyrite cubic unit cell

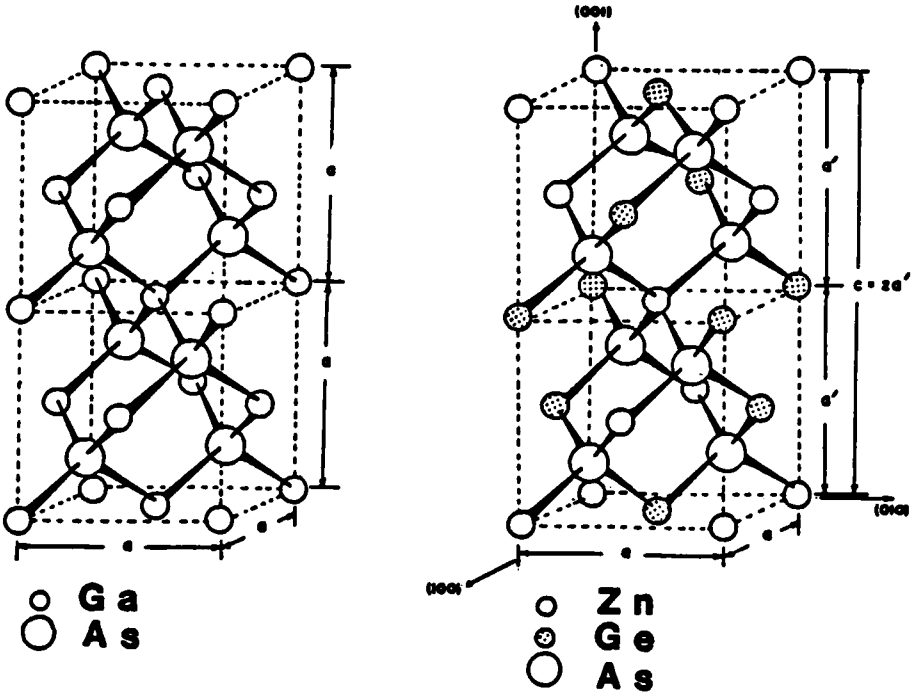

(c) Physical properties of GaAs and $ZnGaAs_2$

	a (Å)	c (Å)	c/a	Eg (ev)	M.P. (°C)
GaAs	5.653	—	—	1.43	1237
$ZnGeAs_2$	5.670	11.153	1.967	1.15	850
	5.672	11.153	1.966		875

Figure 1 Crystal structures and physical properties of GaAs and $ZnGeAs_2$.

3.1 $Zn-Ge-AsCl_3$ METHOD

$ZnGeAs_2$ is one of the least studied II-IV-V_2 chalcopyrite compounds. Vapor phase epitaxial growth of $ZnGeAs_2$ was investigated for the first time with a $Zn-Ge-AsCl_3$ system [2]. It was an open flow system. The reactor is shown schematically in Figure 2. The Zn is transported by passing H_2 over it. The $AsCl_3$ is reduced to As_4 and HCl upon entering the hot furnace, and the HCl reacts with solid Ge to produce $GeCl_2$. At lower temperatures the $GeCl_2$ will undergo a disproportionation reaction to transport the Ge. Epitaxial layers with varying quantities of Zn, Ge, and As were obtained. None of these layers had the proper stoichiometric composition and were apparently Ge epitaxial layers with high doping concentrations of Zn and As. Because of the problems associated with this method, other growth processes were investigated.

3.2 $Zn-GeCl_4-Ge-As_4$ METHOD

Selection of a chemical process for epitaxial growth is based on a number of factors, including availability of suitably pure reactants, their compatibility with the growth apparatus, and the thermodynamics of the process. A chemical analysis is essential not only to arrive at the optimum growth conditions but also for the proper apparatus design. In order to qualitatively predict the direction of a chemical reaction as a function of temperature, it is necessary to know the Gibbs free energy change ΔG for the reaction. The Gibb free energy change ΔG for a reaction is related to the equilibrium constant K by,

$$\Delta G = - RT \ln K = - 4.574T \log K \text{ [3].}$$

In the usual formulation of a chemical reaction if ΔG is

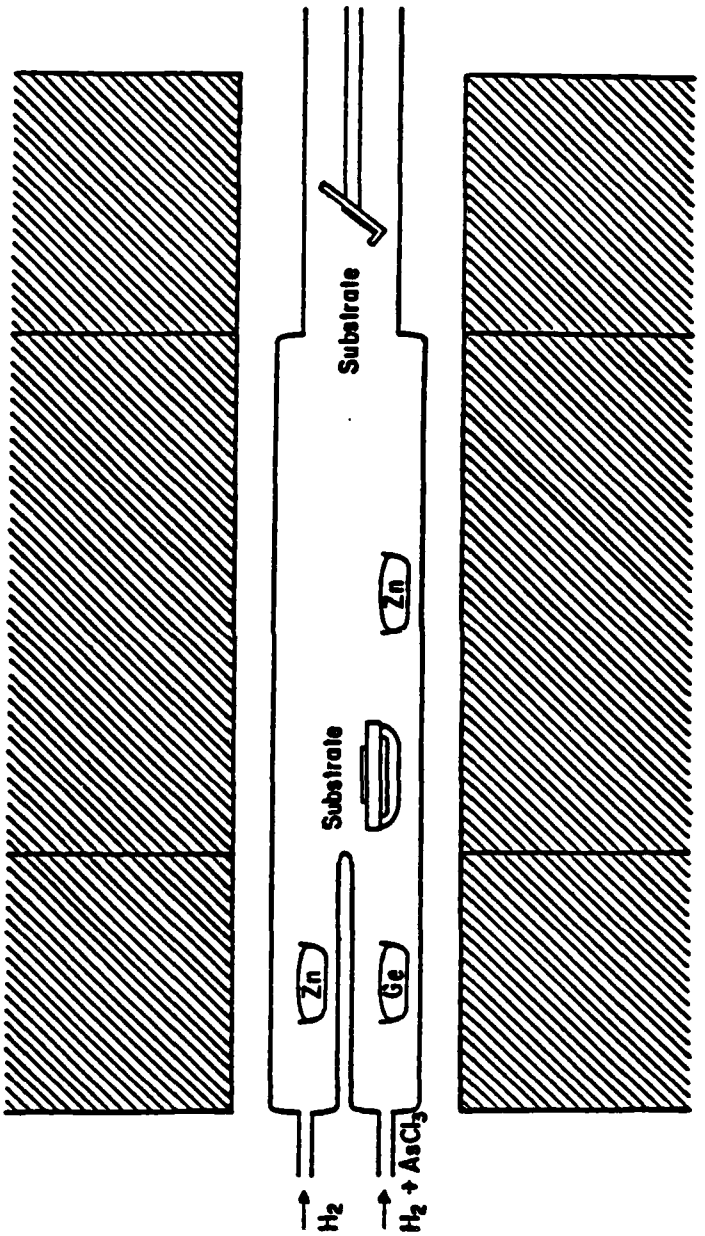

Figure 2 The Zn-Ge-$AsCl_3$ reactor system.

negative, the reaction proceeds to the right and $K > 1$, while if ΔG is positive the reaction proceeds to the left and $K < 1$. To determine a suitable reactor system, the chemical equilibrium constants for the reactions of Ge in a chloride system [2,4] are shown in Figure 3.

In the $Zn\text{-}GeCl_4\text{-}Ge\text{-}As_4$ system, the $GeCl_4$ serves as a source of Ge and Cl_2 for Ge and Zn transport. The $GeCl_4$ is kept in an external bubbler. Since $GeCl_4$ is a volatile liquid at room temperature, palladium purified hydrogen is bubbled through the $GeCl_4$ to saturate it with $GeCl_4$ vapor. This forms the input to the part of the reactor containing the Ge boat. The primary reaction that takes place is,

$$GeCl_4 + Ge \rightarrow 2\ GeCl_2.$$

The equilibrium constant K for this reaction is given [7] by the equation,

$$\log K = \frac{-7660}{T} + 10.25$$

and

$$K = \frac{P^2(GeCl_2)}{P\ (GeCl_4)}\ ,$$

where T is temperature in degrees Kelvin, and the vapor pressures used are in atmospheres. The $GeCl_2$ serves as a means of transport for the Ge.

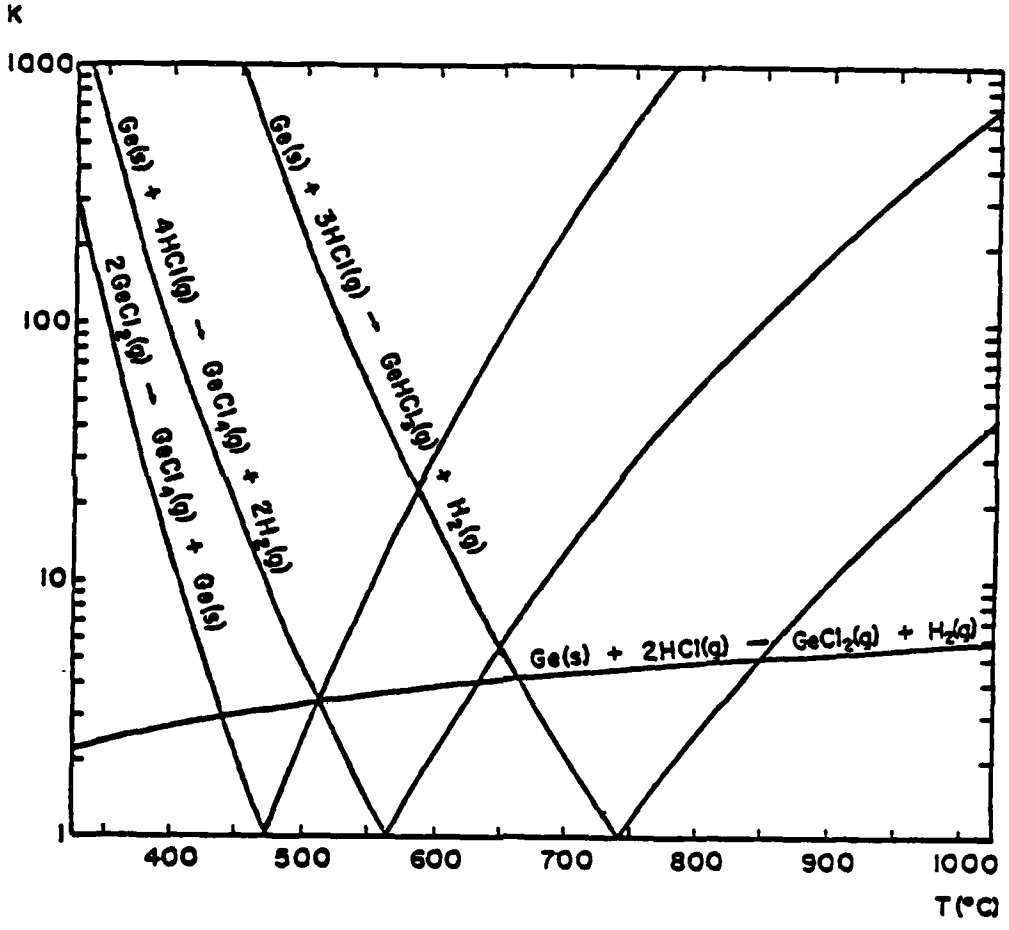

Figure 3 Chemical equilibrium constants for reactions of Ge in a chloride system.

Hydrogen is passed over the As_4 boat to transport As_4 vapor. The vapor pressure is determined by the temperature of the As_4 boat.

The Zn vapor reacts with the $GeCl_2$ vapor to deposit solid Ge and form $ZnCl_2$ vapor according to the reaction,

$$GeCl_2 + Zn \rightarrow Ge + ZnCl_2.$$

The equilibrium constant K for this reaction is given [6] by the equations,

$$\log K = \frac{1}{-4.574}\left[\frac{-52536.91}{T} - 1.98 \log T + 42.91288\right]$$

and

$$K = \frac{P(ZnCl_2)}{P(GeCl_2)P(Zn)},$$

where T is in degrees Kelvin and the vapor pressures are in atmospheres.

By applying this chemical analysis and mass conservation laws, reactant partial pressures and molar ratios for a given set of growth parameters are calculated. It is assumed that the total pressure is independent of temperature and constant throughout the system at 760 torr.

3.2.1 Growth Experiments

Attempts to synthesize $ZnGeAs_2$ were carried out by employing high purity Zn, Ge, As_4, and $GeCl_4$. Figure 4 shows the reactor which was used for this purpose. It consists of a quartz tube in a furnace with three independently controllable zones. The left hand zone controls the As_4 vapor pressure, the center zone controls the Zn vapor pressure, and the right hand zone is the reaction zone. The substrate holder and boats are fabricated from fused quartz. The ultra high purity H_2 is obtained using a palladium diffusion cell and is used as a carrier gas in the reaction tube to move the reactants into the reaction zone. Each H_2 flow is controlled by independent needle valves and pneumatic flow controllers and monitored using rotameters with pyrex or 316 stainless steel floats. The Zn and As_4 sources are contained in quartz boats and inserted in the furnace tube. The $GeCl_4$ is contained in a bubbler and its temperature could be varied from -20° to $30^{\circ}C$. A hydrogen dilution line which bypasses the $GeCl_4$ bubbler is also provided. It is therefore possible to vary the mole fraction of $GeCl_4$ flowing into the reaction tube by either changing the vapor pressure at the $GeCl_4$ source while keeping the total flow constant, or by adding pure hydrogen through the dilution line at a fixed $GeCl_4$ source temperature.

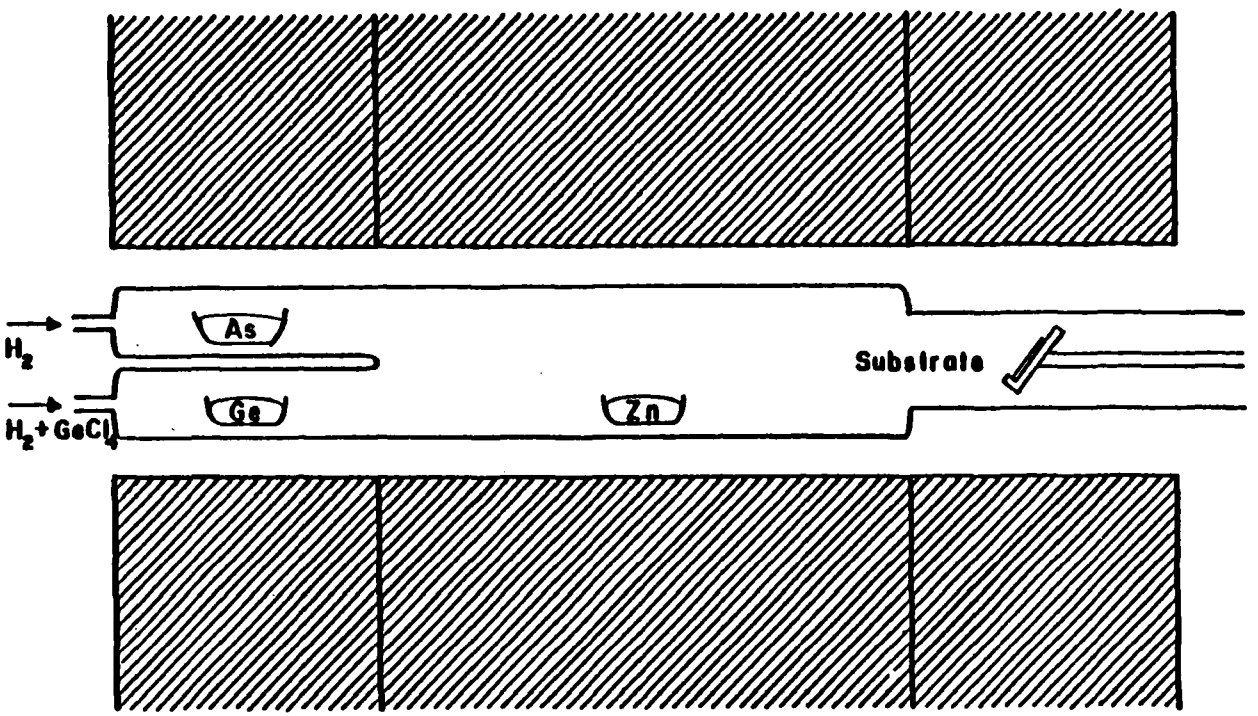

Figure 4 The Zn-$GeCl_4$-Ge-As_4 reactor system.

Epitaxial layers were grown on chromium-doped GaAs semi-insulating substrates, oriented 2^{o} off the {100} planes. The measured resistivity for these substrates was typically 10^{7} ohm-cm. Before preparing the substrates, the wafers were cleaved into the desired size. These were then degreased by boiling successively in trichloroethylene, acetone, and methanol. The samples were then dried with bibulous paper and nitrogen gas. Prior to insertion of a sample into the reactor, a chemical etch was performed to give a clean surface. An etchant consisting of 5 H_2SO_4:1 H_2O_2:1 H_2O was mixed and allowed to cool for 4 minutes. The sample was then etched for 6 minutes and rinsed in deionized water while being careful not to expose it to air. After rinsing, the sample was again dried with bibulous paper. The sample was then immediately placed in the sample holder and inserted in the furnace.

Following the insertion of the seed crystal into the reactor, the entire system was flushed with hydrogen at a high flow rate for 30 minutes. The reaction tube was then heated to the growth temperature profile and the hydrogen flow rates for both barrels were set at 100 ml/min. The whole system was allowed to stabilize

for one hour, then the hydrogen in the first barrel was diverted through the $GeCl_4$ to start growth. There was no vapor etching of the sample before growth. Growth was allowed to continue for 2 hours. To terminate growth, the hydrogen was diverted around the $GeCl_4$ and the hydrogen flow rates were reduced to 30 ml/min for both barrels. The furnace was turned off immediately and allowed to cool by opening it.

To try to find the experimental conditions under which $ZnGeAs_2$ could be grown, the Zn and As_4 temperatures were set at 600° and 580°C, respectively. These temperatures provided a large enough flux of these species to essentially flood the reaction zone. With the Ge temperature set at 560°C to produce the disproportionation reaction with $GeCl_4$, the temperatures of $GeCl_4$ and the reaction zone were systematically varied. Over most of the range of these experiments, little or no growth occurred on the {100} GaAs substrates. With substrate temperatures around 720°C and $GeCl_4$ temperatures in the range from 4 to 10°C, a number of good quality epitaxial layers were obtained.

3.2.2 Material Properties

The properties of the layers grown with this method were established by analysis of surface morphology and

interfacial characteristics, Hall and resistivity measurements, and x-ray diffraction.

Surface morphologies and interfacial characteristics of epitaxial layers were studied with a metallurgical microscope. The back surface of the sample was lapped with 5 and 2 μm grits to remove the epitaxial growth from the back of the sample and to facilitate cleaving the sample. The interface between the epitaxial layer and substrate was made visible by a delineation etch. The delineation etch consisted of 1 HF:4 H_2O:3 HNO_3. Figure 5 shows the upper surface and interface of one of the epitaxial layers. The layers have a very high degree of preferred orientation and their interfaces are quite flat and smooth.

Ohmic contacts were made to the sample using 20 mil diameter Sn spheres alloyed at 220°C for two minutes in a high purity hydrogen atmosphere. Van der Pauw Hall and resistivity measurements were then used to determine the resistivity, carrier concentration, and Hall mobility of the grown layers. The results indicate that these epitaxial layers were all n-type. Typical values of electron concentration and mobility were $5\times10^{19}cm^{-3}$ and 100 $cm^2/V\text{-}sec$, respectively. Some of these n^+ layers

(a) Surface

(b) Interface

Figure 5 Epitaxial layer grown in the $Zn\text{-}GeCl_4\text{-}Ge\text{-}As_4$ system.

were also grown on $10^{15}cm^{-3}$ n-type GaAs. The specific contact resistance of these n-n^+ heterostructures was about 0.1 Ω cm^2.

A Geiger diffractometer was used to examine material deposited in regions near the seedholder in the reactor. This material was prepared for diffraction analysis by grinding it into a fine powder and placing it on a flat plate. This plate was then inserted into the specimen holder of the diffractometer. The materials were identified from their diffraction patterns with the aid of a Hanawalt index and file. Analysis of this material indicated that the epitaxial layers grown in the same region were mostly germanium. Figure 6 shows a diffraction pattern of these Ge deposits.

3.2.3 Discussion

Although these Ge layers are quite good, we were not able to grow the compound $ZnGeAs_2$ under these conditions. The preparation of this compound appears to be very critically dependent upon the reaction conditions. Therefore, several growth runs were made with different growth parameters, and x-ray diffraction measurements were made to determine the composition of the material deposited at various places in the reactor. Some of these results are shown in Table 2.

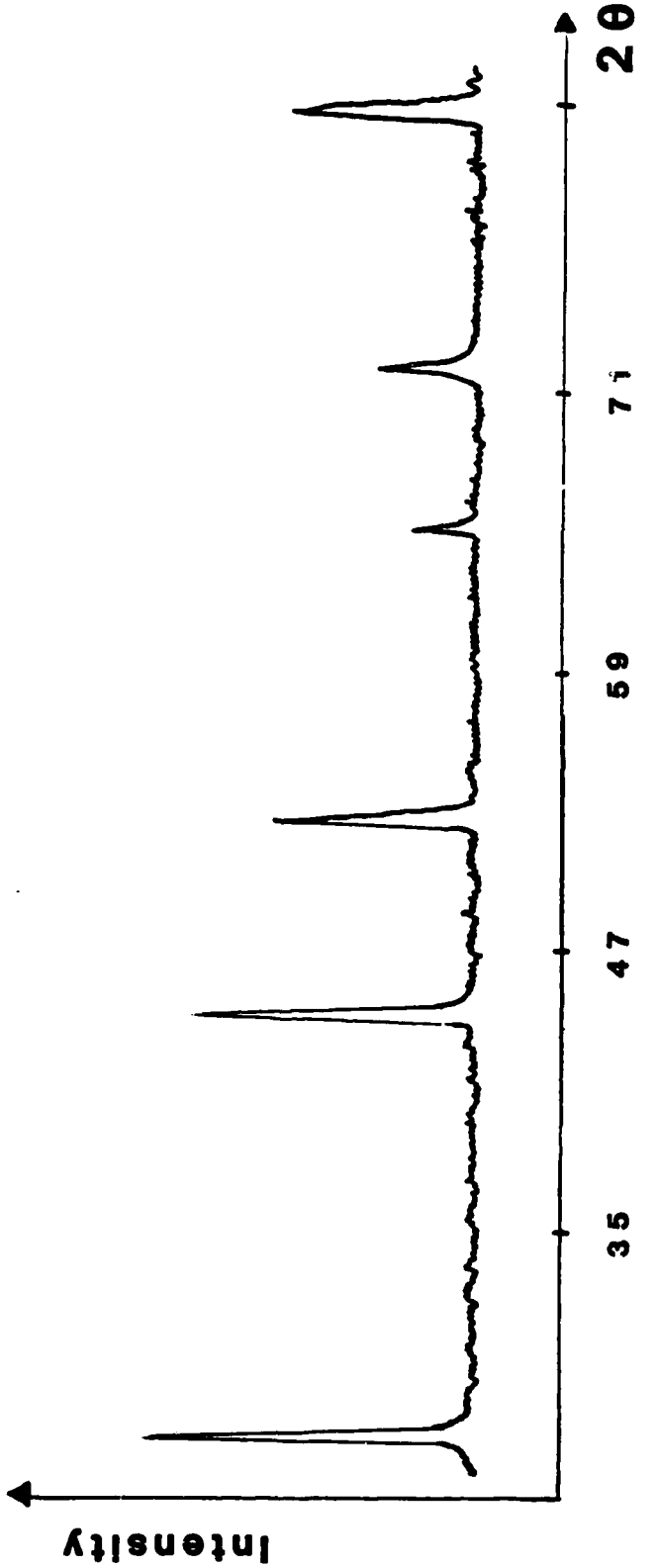

Figure 6 Diffraction pattern of Ge deposits.

Table 2 An investigation with x-ray diffraction.

Sample	T_{Zn} (^{o}C)	T_{GeCl_4} (^{o}C)	T_{As} (^{o}C)	Reactant vapor pressure (torr)			$\frac{Ge}{H_2}$	$T_{substrate}$ (^{o}C)	Growth composition
				P_{ZnCl_2}	P_{GeCl_2}	P_{As_4}			
1	600	4.1	580	7.66	11.35	261.18	0.0237	360	Poly As_4
2	600	4.1	580	7.66	11.35	261.18	0.0237	720	10.1μm Ge layer
3	600	10.1	460	11.66	23.39	13.09	0.0329	720	18μm Ge layer
4	600	5.3	500	29.84	0.48	35.47	0.0006	660	Ge and Zn_3As_2

Typically, the factors which affected the nature of the deposits most were substrate temperature and reactant ratio. Polycrystalline As_4 was formed at lower temperatures while Ge and Zn_3As_2 were formed at high temperatures. The Ge/H_2 ratio or Ge input flux variations were achieved by changing the vapor pressure at the $GeCl_4$ source while keeping the total flow constant. The data show a strong Ge growth rate dependence with Ge/H_2 ratio. The choice of reactant vapor pressure ratio $Zn:GeCl_4:As_4$ appears to be important. When the molar ratio of $GeCl_2$ in the reactant mixture is high, $GeCl_2$ is further transported down the reactor tube, and Ge is deposited out by reaction of $GeCl_2$ with H_2. When the molar ratio of $GeCl_2$ in the mixture is low, large quantities of Zn_3As_2 platelets form inside the Zn boat together with Ge platelets.

In summary, the preparation of $ZnGeAs_2$ with the $Zn\text{-}GeCl_4\text{-}Ge\text{-}As_4$ system was found to be much too strongly dependent upon the various growth parameters. When As_4 was transported over the Zn boat, Zn_3As_2 platelets were formed. Apparently, this greatly reduces further transport of Zn or As_4 vapor and results in the depletion of Zn or As_4 in the reaction zone. This appears to be the main problem with this $Zn\text{-}GeCl_4\text{-}Ge\text{-}As_4$ system:

it gives excellent control of the Ge flux, but very little control for Zn and As_4. Previous to this study, we investigated a Zn-Ge-$AsCl_3$ reactor and found that it produced good As_4 control. For these reasons, we attempted to synthesize the compound in a Zn-$GeCl_4$-$AsCl_3$ reactor, which should incorporate the best features of the two previous systems without their disadvantages.

3.3 Zn-$GeCl_4$-$AsCl_3$ METHOD

In the Zn-$GeCl_4$-$AsCl_3$ system, the $AsCl_3$ serves as a source of As_4 vapor while the $GeCl_4$ serves as a source of Ge. The $AsCl_3$ is kept in an external bubbler. Palladium purified hydrogen is bubbled through the $AsCl_3$ and the $AsCl_3$ saturated vapor is passed into the first barrel of the reaction tube. The initial reaction taking place when the $AsCl_3$ and H_2 gas mixture enters the hot reaction tube is,

$$4\ AsCl_3 + 6\ H_2 \rightarrow As_4 + 12\ HCl.$$

Since the equilibrium constant is very large, this reaction is assumed to go to completion. Therefore, the input pressures for As_4 and HCl are computed as,

$$P(As_4) = 1/4\ P(AsCl_3),$$

and

$$P(HCl) = 3\ P(AsCl_3).$$

These input pressures are then normalized for a total system pressure of 760 torr.

In the second barrel of the reactor system, hydrogen is passed over a Zn boat to transport elemental Zn vapor. The vapor pressure of the Zn is determined by the temperature of the Zn boat.

The $GeCl_4$ is kept in an external bubbler. Hydrogen is bubbled through the $GeCl_4$ to saturate it with $GeCl_4$ vapor. Various reactions of Ge in a chloride system were examined carefully (Figure 3). The two chemical reactions involved in the third barrel of this reactor system are,

$$GeCl_4 + 2\ H_2 \rightarrow Ge + 4\ HCl,$$

and

$$Ge + 2\ HCl \rightarrow GeCl_2 + H_2.$$

When the $GeCl_4$ and H_2 gas mixture enters the hot reactor tube, the $GeCl_4$ readily reacts with H_2 at the temperature of the first zone and deposits out Ge. HCl vapor then reacts with solid Ge to produce $GeCl_2$ vapor. The $GeCl_2$ vapor then serves as a means of transport for the Ge. Calculations of the reactant partial pressure and mole ratio are based on the above analysis.

3.3.1 Growth Experiments

The growth system employs Zn, $GeCl_4$ and $AsCl_3$ as reactants with ultra high purity H_2 as the carrier gas.

High purity elemental Zn (99.999%) and electronic grade $GeCl_4$ and $AsCl_3$ are used as starting materials. The reactor consists of a 44 mm OD quartz tube having separate reactant inlets and a furnace with three independently controllable zones (Figure 7). The left hand zone controls the Zn vapor pressure, while the right hand zone is the reaction zone. The Zn boat and substrate holder are fabricated from fused quartz. The $GeCl_4$ and $AsCl_3$ enter the reactor downstream from the Zn source. Both $GeCl_4$ and $AsCl_3$ are contained in gas saturators held at the same temperature by using a refrigerated circulator. An additional H_2 flow is also provided to dilute the $GeCl_4$ if necessary. H_2 flow rates through different inlets of the reactor are adjusted by needle valves and monitored with rotameters specifically calibrated for H_2.

Attempts were made to grow epitaxial layers on Cr-doped semi-insulating GaAs substrates. The substrate is etched in a 5 H_2SO_4:1 H_2O_2:1 H_2O solution as previously discussed. After etching, the substrate is placed on the sample holder and inserted in the furnace. The reaction tube is then flushed with H_2 and heated to the growth temperature profile. There is no vapor etching of the sample before growth. The reactant flows of

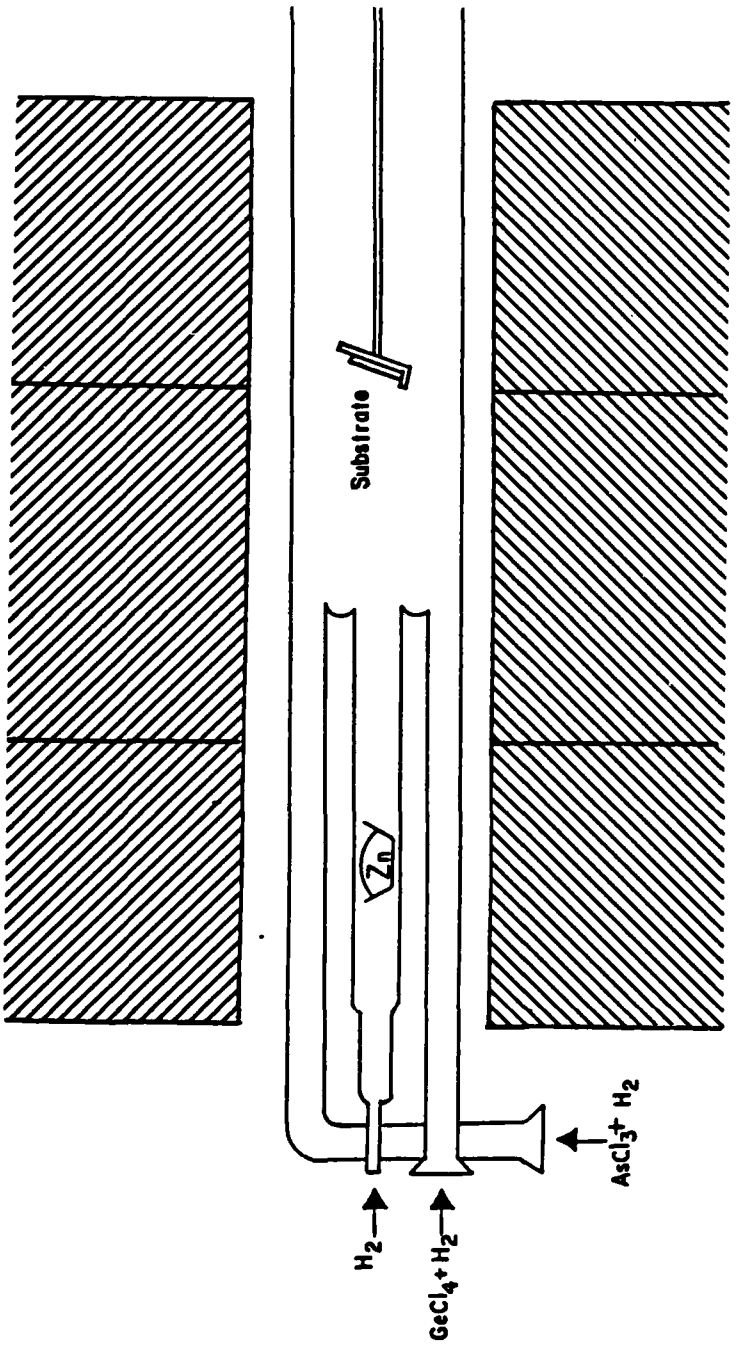

Figure 7 The Zn-$GeCl_4$-$AsCl_3$ reactor system.

$GeCl_4$ and $AsCl_3$ are initiated and terminated simultaneously. Following deposition at the growth temperature, the reaction tube is then cooled to room temperature rapidly to terminate the transport of Zn and minimize surface erosion of the sample. A systematic study of the many experimental parameters was carried out. The growth parameters used are shown in Tables 3 and 4, in which we specify the temperature profile in which growth was achieved, the reactant flows, total flow rates, growth composition, and other parameters.

3.3.2 Material Properties

The properties of the material grown by this process were established by analysis of surface morphology and interfacial characteristics, Hall and resistivity measurements, Auger electron spectroscopy, and x-ray diffraction. This analysis, however, indicated that these layers were either Ge or Zn_3As_2.

Figure 8 shows the upper surface and interface of one of the Ge layers which appears to be polycrystalline. A significant amount of Zn diffusion into the GaAs substrate is revealed in the cross-sectional view. Zn_3As_2 layers were also synthesized in this system. Figure 9 shows the surface morphology of a Zn_3As_2 layer.

Table 3 Growth parameters for the Zn-$GeCl_4$-$AsCl_3$ system.

Sample No.	Temperature profile			Temperature of $GeCl_4$ & $AsCl_3$ (°C)	H_2 flow rates through different barrels (ml/min)				Substrate temperature (°C)	Total flow (ml/min)	Growth composition
	CP_1 (°C)	CP_2 (°C)	CP_3 (°C)		$GeCl_4$	Dilution line	Zn	$AsCl_3$			
J14.5	700	740	700	5.4	74	38	102	84	728	298	Ge
J14.6	700	740	700	5.4	78	16	102	88	728	284	Ge
J14.7	700	740	700	5.4	78	60	98	84	728	320	Ge
J14.8	700	740	700	5.4	76	80	102	82	728	340	Ge
J14.9	700	740	700	5.4	76	102	102	86	728	366	Ge
J15.0	700	640	700	5.4	78	102	102	88	630	370	Ge
J15.1	700	680	700	5.4	78	102	102	82	668	364	Ge
J15.2	700	700	700	5.4	76	102	102	82	688	362	Ge
J15.3	700	720	700	5.4	78	102	102	82	707	364	Ge
J11	600	640	720	5.4	78	0	114	70	630	262	Ge
J20.1	700	620	620	5.4	78	104	140	88	610	410	Ge

Table 4 Growth parameters for the Zn-$GeCl_4$-$AsCl_3$ system.

Sample No.	Temperature profile			Temperature of $GeCl_4$ & $AsCl_3$	H_2 flow rates through different barrels (ml/min)				Substrate temperature	Total flow	Growth composition
	CP_1 (°C)	CP_2 (°C)	CP_3 (°C)	(°C)	$GeCl_4$	Dilution line	Zn	$AsCl_3$	(°C)	(ml/min)	
J6	780	710	650	5.4	76	80	98	86	708	340	Zn_3As_2
J7	780	710	650	5.4	80	0	102	84	708	266	Zn_3As_2
J19.0	780	710	650	5.3	140	0	106	82	708	328	Ge
J19.1	780	710	650	5.4	100	0	100	82	708	282	Ge

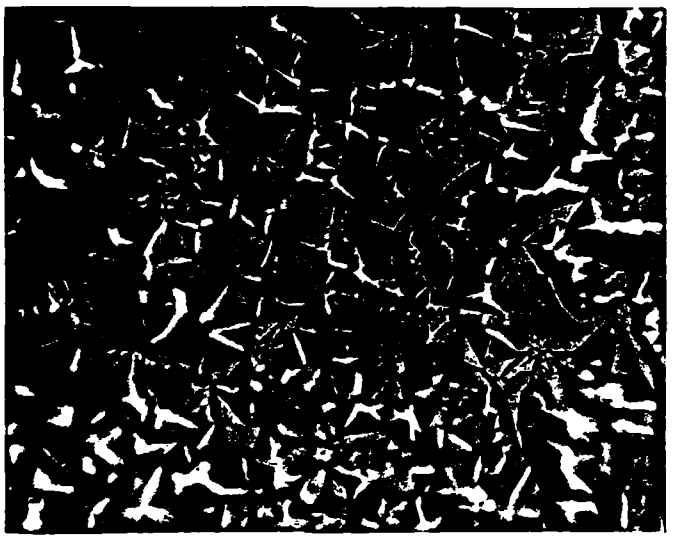

(a) surface

(b) interface

Figure 8 Ge layer grown in the $Zn-GeCl_4-AsCl_3$ system.

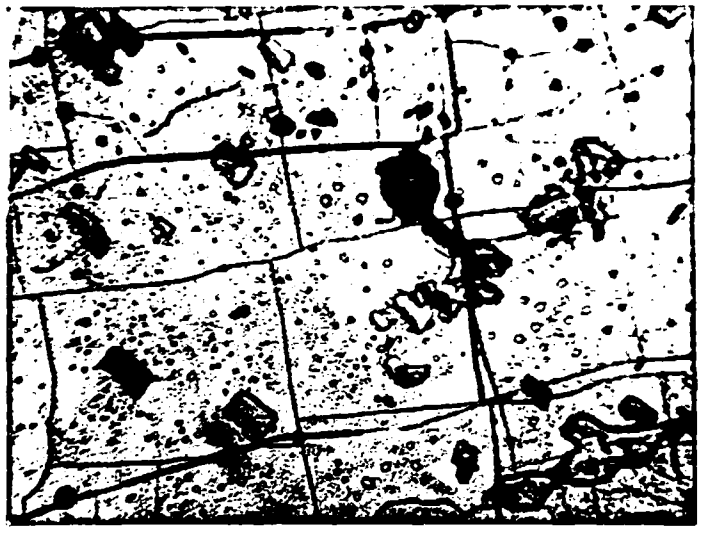

Figure 9 Surface morphology of a Zn_3As_2 layer.

Localized stresses in the layer results from large lattice mismatch between the Zn_3As_2 layer and GaAs substrate.

The Ge layers on Cr doped GaAs substrates were typically p-type with carrier concentrations of about $7\times10^{19}cm^{-3}$ and hole mobilities of 40 $cm^2/V\text{-}sec$. The Zn_3As_2 layers tend to crack easily. Therefore, no Hall and resistivity measurements were made on these layers.

The composition of the material synthesized was confirmed by Auger electron spectroscopy and x-ray powder diffraction analysis.

Auger electron spectroscopy was performed to determine the composition of the sample surfaces. Figure 10 shows the polycrystalline surface morphology of Sample J14.6. The sample appears to have a solid, although multi-crystalline surface. Auger spectra for this layer before and after sputter etching are shown in Figure 11. The spectra indicate that the large crystals on the surface are germanium. The surface morphology of Sample J14.7 (Figure 12) shows dendritic structure with white patches present on the surface. The Auger spectra of Sample J14.7 in the area of the white precipitate are shown in Figure 13.

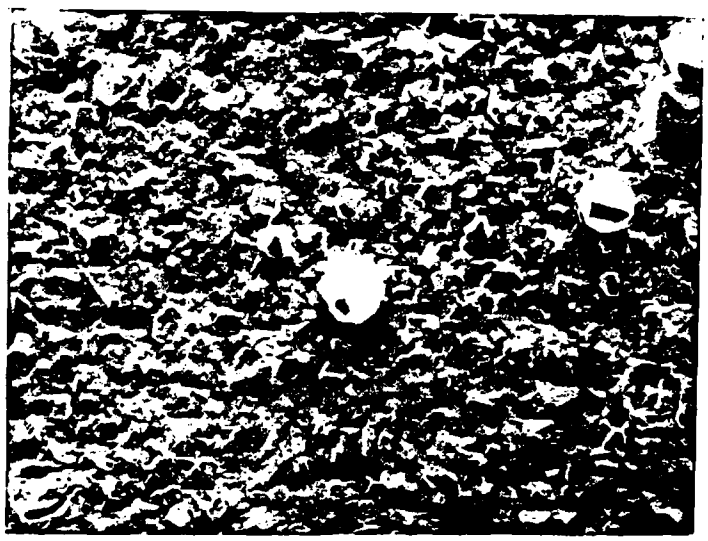

Figure 10 Solid polycrystalline structure of Sample J14.6.

AD-A120 416 II-IV-V2 CHALCOPYRITES FOR HIGH SPEED DEVICES(U) 2/2
WASHINGTON UNIV ST LOUIS MO SEMICONDUCTOR RESEARCH LAB
C M WOLFE ET AL. 31 JUL 82 WU/SRL-59457-5
UNCLASSIFIED AFOSR-TR-82-0906 AFOSR-79-0096 F/G 20/2 NL

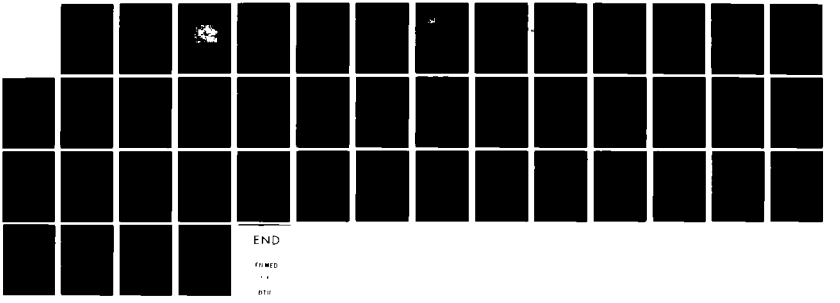

END

FILMED

DTIC

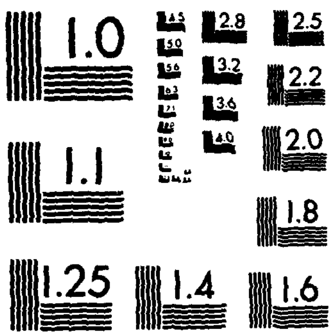

MICROCOPY RESOLUTION TEST CHART
NATIONAL BUREAU OF STANDARDS-1963-A

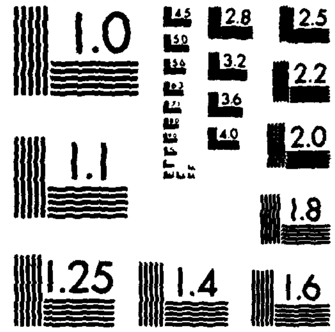

MICROCOPY RESOLUTION TEST CHART
NATIONAL BUREAU OF STANDARDS-1963-A

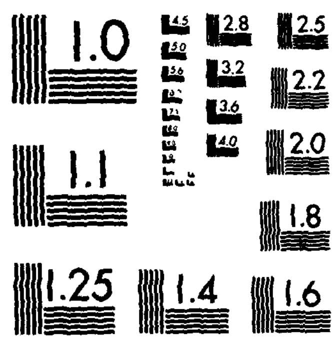

MICROCOPY RESOLUTION TEST CHART
NATIONAL BUREAU OF STANDARDS-1963-A

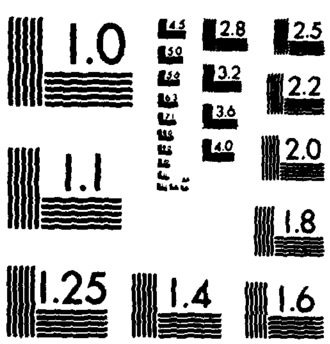

MICROCOPY RESOLUTION TEST CHART
NATIONAL BUREAU OF STANDARDS-1963-A

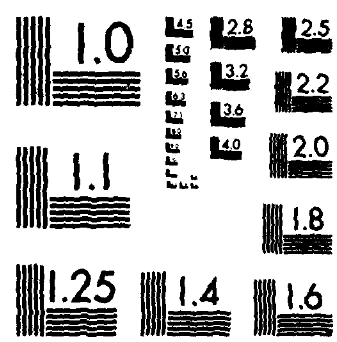

MICROCOPY RESOLUTION TEST CHART
NATIONAL BUREAU OF STANDARDS-1963-A

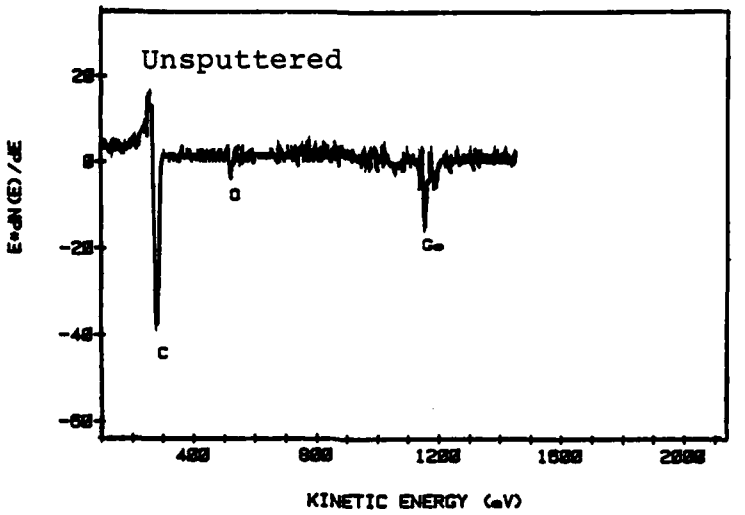

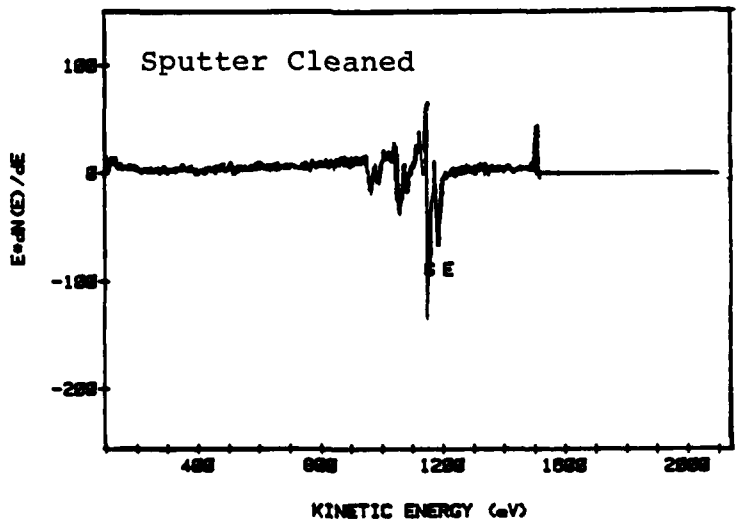

Figure 11 Auger spectra for the surface of Sample J14.6.

Figure 12 Dendrite-like structure with white patches for Sample J14.7.

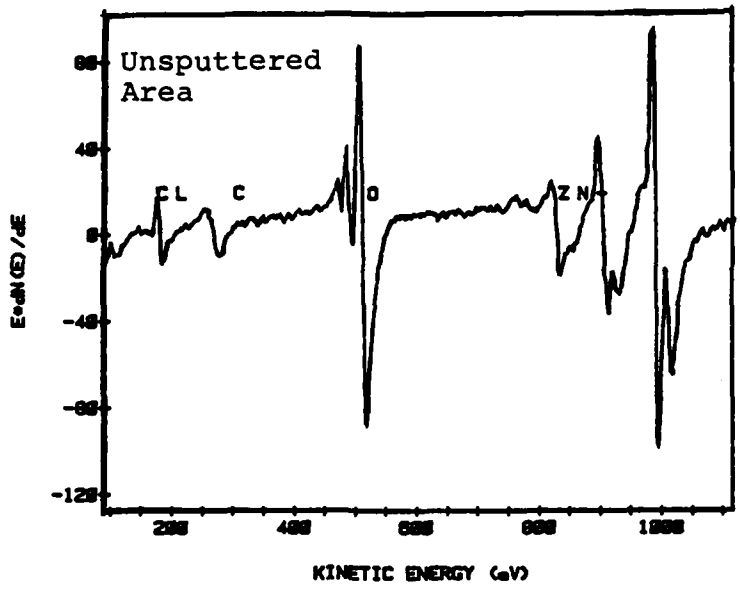

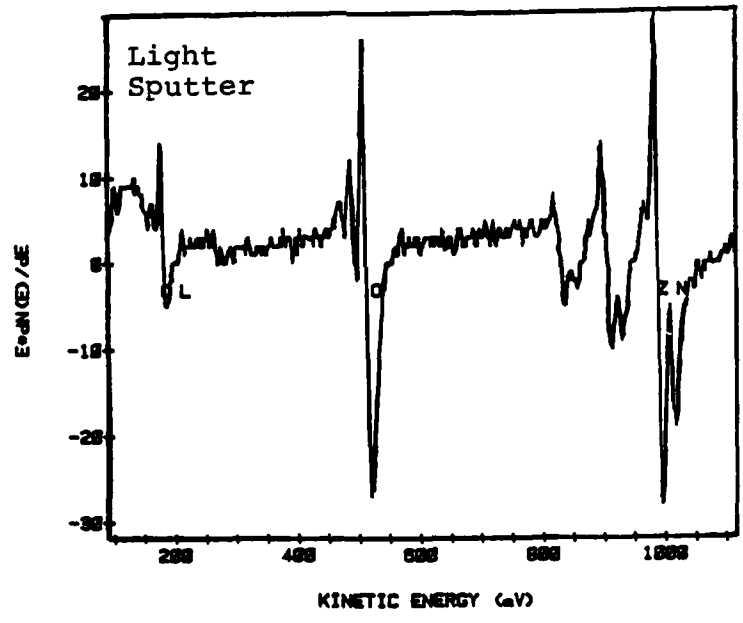

Figure 13 Auger spectra for Sample J14.7 in the area of the white precipitate.

The spectra show that the patches of lighter material are Zn_x, O_x, and Cl_x. Both samples are contaminated by carbon and oxygen.

The Debye-Scherrer powder x-ray diffraction method was employed to analyze the composition of the material grown. Cu K radiation with a Ni filter was used as the x-ray source at a wavelength of 1.5405 Å. Platelets deposited in the region near the substrate in the reactor were prepared for diffraction analysis by grinding them into a fine powder. The powder was mixed with a small amount of glue and then rolled or extruded into a small cylinder. The powder specimen was then inserted into the specimen holder of the Debye camera. Compounds are identified by comparison of their powder x-ray diffraction spectra with data in the ASTM x-ray powder data file [5] Several powder diffraction patterns were obtained.

The powder photograph yields a set of numerical values for various interplanar spacing of the crystal sample. The interplanar spacing of the sample can be calculated from the Bragg equation,

$$d = \frac{\lambda}{2 \sin \theta}$$

where d is the interplanar spacing, λ is the wavelength of the x-ray source, and θ is the angle.

Figure 14 shows powder diffraction photographs of Samples J14.6 and J23.5. Table 5 shows the ASTM powder data and d values of Sample J14.6 calculated from its diffraction pattern. Table 6 shows the ASTM powder data for Zn_3As_2 and d values of Sample J23.5 calculated from its diffraction photograph. Results show that Sample J14.6 is Ge and Sample J23.5 is Zn_3As_2.

3.3.3 Discussion

Ge and Zn_3As_2 layers have been synthesized in the Zn-$GeCl_4$-$AsCl_3$ system with different growth parameters. The existence of these materials was confirmed with Auger electron spectroscopy and x-ray powder diffraction analysis. A transition from Ge to Zn_3As_2 with growth conditions was observed as indicated in Table 4. All these layers were synthesized with the same growth temperature profile but different input reactant flow rates. Also, the substrates were located very close to the three barrel section of the reactor.

The growth parameters were examined to see what determines whether Ge or Zn_3As_2 will be deposited on the substrate. Reactant partial pressures, reactant mole ratios, and the growth composition of the samples are summarized in Table 7. From the data in Table 7 it was found that: (1) considerable excesses of Zn and HCl vapors exist in the growth process; (2) Ge will deposit on the substrate if the molar content of $GeCl_2$ in the

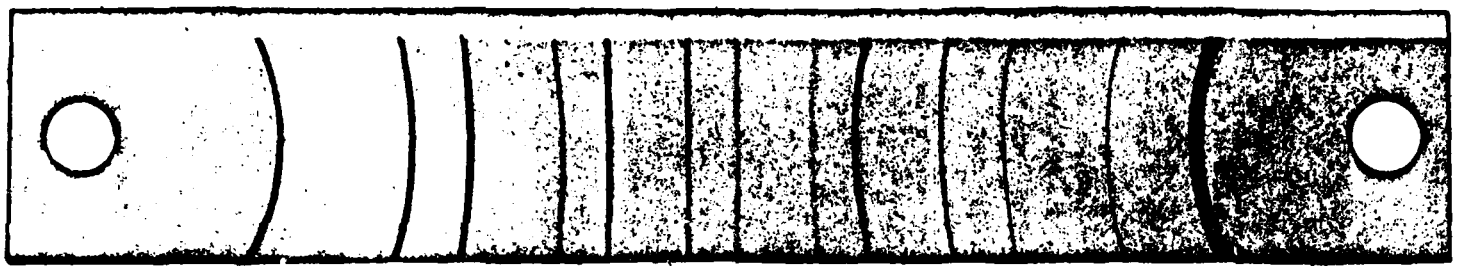

(a) Sample J14.6

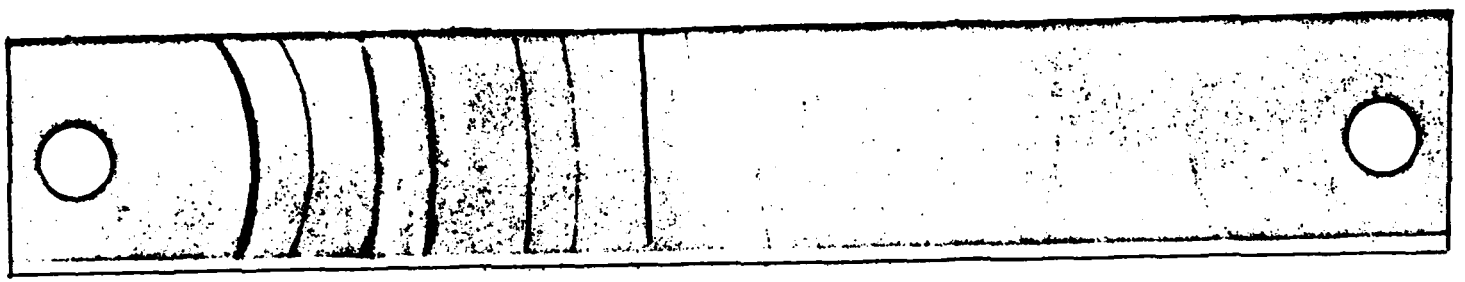

(b) Sample J23.5

Figure 14 X-ray powder diffraction photographs for Samples J14.6 and J23.5.

Table 5 Interplanar spacing values for Sample J14.6.

(a) ASTM power data for Ge

d 4-0545	3.266	2.000	1.706	3.266	Ge
I/I$_1$ 4-0545	100	57	39	100	GERMANIUM

Rad. Cu λ 1.5405 Filter Ni
Dia. Cut off Coll.
I/I$_1$ d corr. abs.?
Ref. SHAMON AND TAYOR, J.C. FEL. REPORTS, FDS (1961)

Sys. Cubic (r.c.) S.G. O_h^7 - Fdm
a_o 5.6576 b_o c_o A C
α β γ Z 4
Ref. Ibid.

εα nωβ ε$_\gamma$ Sign
2V D_x 5.325 mp Color
Ref.

"NITKA, PHYS. Z. 38, 896-901 (1937)
SPECTROGRAPHIC ANALYSIS SHOWS FAINT TRACES OF Ag, Na, Cu, AND Fe
AT 26°C
TO REPLACE 3-0478, 3-0186

d Å	I/I$_1$	hkl	d Å	I/I$_1$	hkl
3.266	100	111			
2.000	57	220			
1.706	39	311			
1.414	7	400			
1.298	10	331			
1.1547	17	422			
1.0988	7	511			
1.0000	3	440			
0.9567	11	531			
.8946	6	620			
.8628	4	533			
.8176	2	444			
.7923	8	711			

(b) Interplanar spacing values for Sample J14.6 calculated from its diffraction photograph

Lines	2θ(°)	Intensity	d(Å)
1	27.6	strong	3.229
2	45.7	very strong	1.984
3	54.1	medium	1.694
4	66.35	medium	1.408
5	73.15	strong	1.293
6	83.9	very strong	1.152
7	90.4	medium	1.086
8	101.2	medium	0.997
9	107.6	strong	0.955
10	119.25	medium	0.893
11	126.9	weak	0.861
12	141.7	weak	0.815
13	153.6	weak	0.791

Table 6 Interplanar spacing values for Sample J23.5.

(a) ASTM powder data for Zn_3As_2

d	3.42	2.10	1.79	3.42	Zn_3As_2
I/I_1	100	80	50	100	Zinc Arsenide

Rad. MoKα λ 0.7107 Filter Zr Dia.
Cut off I/I_1 Visual
Ref. Banus and Lavine, High Temperatures - High Pressures, 1 269 (1969)

Sys. Cubic S.G.
a_o 11.82 b_o c_o A C
α β γ Z Dx
Ref. Ibid.

εα nω β εγ Sign
2V D mp Color
Ref.

d A	I/I_1	hkl	d A	I/I_1	hkl
3.42	100	222			
2.988	5	400			
2.726	20	331			
2.097	80	440			
1.791	50	622			
1.478	20	800			
1.358	20	662			
1.309	5	911			
1.205	40	844			
1.146	10	1022			

(b) Interplanar spacing values for Sample J23.5 calculated from its diffraction photograph

Lines	2θ(°)	Intensity	d(Å)
1	26.35	very strong	3.379
2	33.45	weak	2.677
3	43.45	very strong	2.081
4	51.45	strong	1.775
5	63.15	weak	1.471
6	69.70	weak	1.348
7	79.70	medium	1.202
8	85.65	weak	1.133

Table 7 Reactant partial pressures, reactant mole ratios, and growth composition for samples listed in Table 4.

Sample No.	Reactant vapor pressure (torr)					Reactant mole ratio	Growth composition
	P_{Zn}	P_{GeCl_2}	P_{As_4}	P_{HCl}	P_{H_2}	$Zn:GeCl_2:As_4$	
J6	46.297	5.0586	0.5674	25.380	682.69	1:0.109:0.012	Zn_3As_2
J7	61.592	9.1224	0.7083	28.053	660.52	1:0.148:0.011	Zn_3As_2
J19.0	51.909	12.946	0.5608	34.480	660.10	1:0.249:0.010	Ge
J19.1	59.723	10.713	0.6496	30.761	658.15	1:0.179:0.010	Ge

reactant mixture is high enough. In addition, large numbers of Ge platelets were always formed at the outlet of the third barrel in the reactor during the growth experiments. The equilibrium constant of the reaction,

$$GeCl_2 + Zn \rightarrow Ge + ZnCl_2,$$

was then examined.

The chemical equilibrium calculation and experimental results indicated that $GeCl_2$ vapor readily reacts with Zn vapor to deposit solid Ge and form $ZnCl_2$ in the reaction zone. If the vapor pressure of $GeCl_2$ is large enough, Ge will also deposit on the substrate which is located very close to the three barrel section of the reactor.

The premature reaction of $GeCl_2$ with Zn results in the depletion of $GeCl_2$ vapor in the reactant gas mixture and this is the explanation for the failure to synthesize $ZnGeAs_2$ in this system.

3.4 PROPOSED HYDRIDE METHODS

Two serious problems are found in the chloride methods of synthesizing $ZnGeAs_2$: (1) premature reactions prevent further transport of source materials; (2) the complexity of the chemical reactions increase the difficulties in controlling growth parameters and synthesizing the desired compound. However, two proposed hydride growth syste can be used to overcome these disadvantages.

3.4.1 Zn-GeH_4-AsH_3 Method

The first proposed hydride system employs elemental Zn, GeH_4 and AsH_3 as reactants with H_2 as the carrier gas. The reactor system is shown in Figure 15. The reactor consists of a quartz tube having separate reactant inlets. The Zn is transported into the deposition region by passing H_2 gas over a Zn melt. The GeH_4 and AsH_3 reactants enter the reactor downstream from the Zn source, and the overall growth reaction is as follows:

$$Zn + GeH_4 + 2\ AsH_3 \rightarrow ZnGeAs_2 + 5H_2.$$

The thermal decomposition of GeH_4 and AsH_3 was chosen for several reasons:

(1) Both GeH_4 and AsH_3 are commercially available in high purity and are stable gases at room temperature.

(2) Deposition can be achieved at relatively low temperatures.

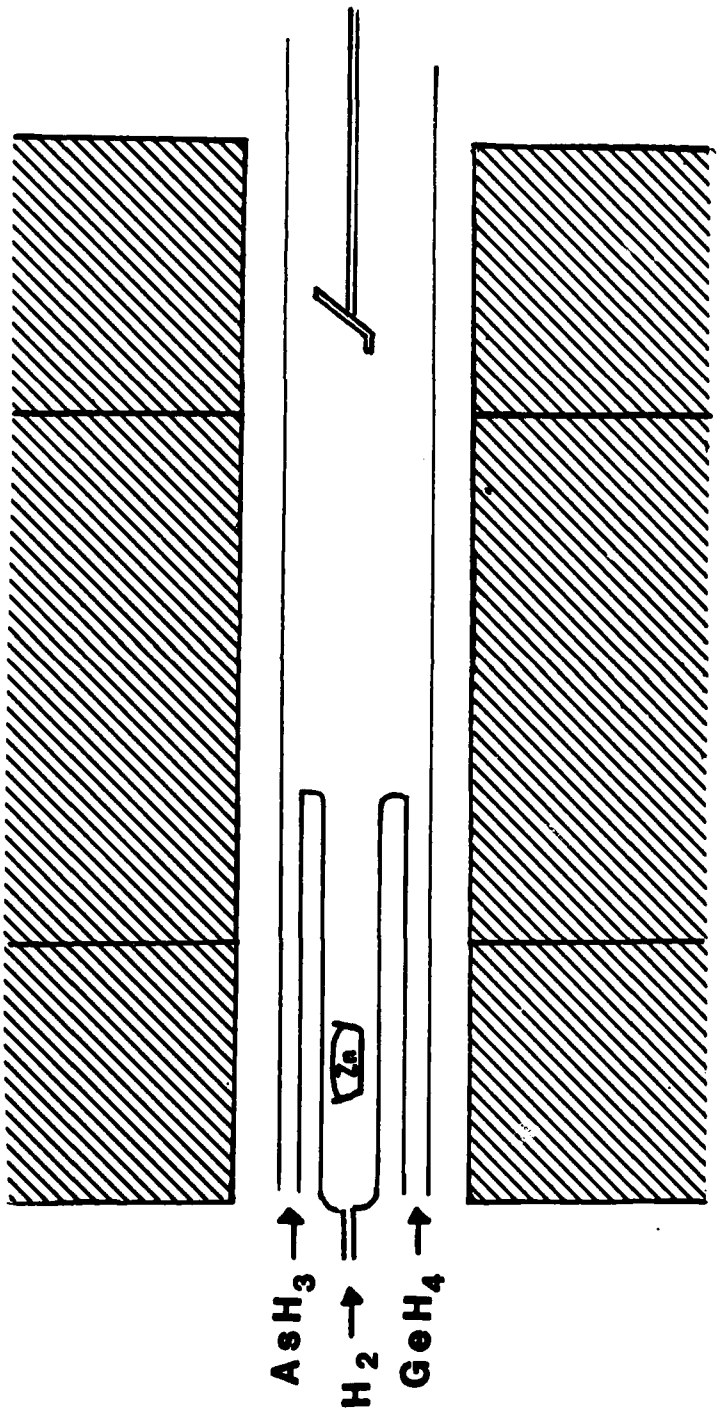

Figure 15 The Zn-GeH_4-AsH_3 system.

(3) There are no reactive by-products of the decomposition reactions.

3.4.2 $Zn(CH_3)_2$-GeH_4-AsH_3 METHOD

The second growth system proposed to synthesize $ZnGeAs_2$ is a horizontal, RF induction heated, open tube chemical vapor deposition system. The reactants are $Zn(CH_3)_2$, GeH_4, and AsH_3 with H_2 as the carrier gas. The liquid dimethylzinc (DMZn) is kept in a bubbler and the hydrogen carrier gas is bubbled through the liquid to saturate and transport its vapor. The deposition of $ZnGeAs_2$ involves the pyrolysis of these reactants according to the overall reaction,

$$Zn(CH_3)_2 + GeH_4 + 2\ AsH_3 \rightarrow ZnGeAs_2 + 2\ CH_4 + 4\ H_2.$$

The advantage of using these reactants is that all three can be transported in the gas phase to the deposition region. Furthermore, transport of $Zn(CH_3)_2$ vapor is readily and almost as easily controlled as the gaseous reactants, GeH_4 and AsH_3.

3.5 CONCLUSIONS

Two chloride systems, Zn-$GeCl_4$-Ge-As_4, and Zn-$GeCl_4$-$AsCl_3$ were employed for the epitaxial growth of $ZnGeAs_2$ on GaAs. Since the preparation of $ZnGeAs_2$ was so critically dependent upon various growth parameters, there was little success. With careful choice of reactant, the Zn-GeH_4-AsH_3 and $Zn(CH_3)_2$-GeH_4-AsH_3 systems could be used to overcome the difficulties encountered in the chloride systems. Both systems should provide easy transport of reactants and precise control of reactant ratio. It is believed that epitaxial $ZnGeAs_2$ could be successfully deposited on GaAs with either of these hydride systems.

3.6 REFERENCES

1. A.S. Borshchevskii, N.A. Goryunova, F.P. Kesamanly, and D.N. Nasledov, "Semiconducting $A^{II}B^{IV}C_2^V$ Compounds", *Physica Status Solidi* 21, 9 (1967).

2. Camellia M.L. Yee, "Vapor Phase Epitaxial Growth of $ZnGeAs_2$ on GaAs", M.S. Thesis, Washington University, St. Louis (1980).

3. O. Kubaschewski and E. Evans, *Metallurgical Thermochemistry*, Pergamon Press, New York (1967).

4. V.J. Silvestri, "Growth Rate and Surface Morphology Studies in the $GeCl_4$-H_2 System", *Journal of the Electrochemical Society* 116, 81 (1969).

5. *ASTM Handbook*, American Society for Testing Materials, X-ray Dept., Philadelphia, Pa.

4. HETEROJUNCTION THERMODYNAMICS

The recent interest in heterostructures for lasers, transistor emitters, real-space transfer devices, quantum well lasers, modulation-doped superlattices, and other devices, has prompted a re-examination of basic heterojunction theory. To understand quantitatively the operation of these devices it is necessary to determine how the discontinuity in the energy gaps of a heterostructure is divided between the conduction and valence bands:

$$\Delta\varepsilon_g = \Delta\varepsilon_c + \Delta\varepsilon_v \qquad (1)$$

The basic assumption of heterostructure theory is the "electron affinity rule": that is, the conduction band discontinuity is simply the difference between the electron affinity of the two materials,

$$\Delta\varepsilon_c = \chi_1 - \chi_2 \ , \qquad (2)$$

presumably referenced to the infinite vacuum level.

4.1 CURRENT PROBLEMS

Kroemer [1] has pointed out a number of problems with this concept, the most important of which are: (1) assuming the rule is valid, the band discontinuities need to be known to an accuracy of about a kT, while the affinities, usually referenced to a near vacuum level, cannot be measured that accurately; (2) the basic differences between free surfaces and solid interfaces are so great that there

is no fundamental reason for expecting any relationship between electron affinities and band discontinuities. Thus, to resolve this problem, it is necessary to forget about phenomenological surface properties and look at the interface problem from a microscopic point-of-view.

In spite of these arguments, Shay *et al* [2] compared measured band discontinuities for several heterojunctions with measured electron affinities from photoemission data and calculated affinities from the dielectric two-band model. They found that the agreement between the measured discontinuities and those calculated from the affinity rule was very good. In addition, Frensley and Kroemer [3] found from a pseudopotential calculation of a heterojunction interface that the affinity rule is approximately correct. Although this is a somewhat surprising result, Kroemer's original objections are, of course, still valid.

More recently, Adams and Nussbaum [4] have examined the affinity rule from an electrostatic point-of-view. They suggest that instead of keeping the vacuum level continuous (the electron affinity rule) it may be more appropriate to assume continuity of the intrinsic level. This paper is interesting because it also, although unintentionally, demonstrates another problem with heterojunction theory: the usual equilibrium and non-equilibrium formulations in the depletion approximation are not self-consistent. This inconsistency occurs regardless of which basic assumption is used.

The problem arises in the following manner: For simplicity assume an abrupt p-n heterojunction. In equilibrium, the built-in potential of the space-charge region is given by,

$$V_0 = \frac{kT}{q} \ln\left(\frac{N_d N_a}{n_{in} n_{ip}}\right), \tag{3}$$

where N_d and N_a are the donor and acceptor concentrations on the n and p side of the heterojunction, respectively, and n_{in} and n_{ip} are the intrinsic concentrations. When the heterojunction is forward-biased with a voltage V, in the depletion approximation the holes injected into the n-side at the edge of the depletion region is usually found to be,

$$p_n = p_p \exp\left[\frac{q(V-V_0)}{kT}\right] . \tag{4}$$

If V is turned off, the excess holes disappear and

$$p_n = \frac{n_{in}^2}{N_d} \quad , \quad p_p = N_a ,$$

and

$$V_0 = \frac{kT}{q} \ln\left(\frac{N_d N_a}{n_{in}^2}\right) . \tag{5}$$

Comparing Eqs. (3) and (5), we see that this analysis is only valid for a p-n homojunction.

The problem we wish to consider is the latter one, although the electron affinity rule is a natural consequence of our analysis. We will show that the inconsistency arises from the neglect of a thermodynamic force term, which is well understood but, apparently, not widely known.

4.2 THERMODYNAMIC ANALYSIS

For any solid it can be shown [5] that the entropy source strength (entropy production rate per unit volume) is,

$$\sigma_s = \vec{J}_Q \cdot \vec{\nabla}\left(\frac{1}{T}\right) + \sum_i \vec{j}_i \cdot \left[\frac{\vec{F}_i}{T} - \vec{\nabla}\left(\frac{\mu_i}{T}\right)\right] + \sum_j \frac{A_j}{T} v_j \geq 0. \qquad (6)$$

In this equation $\vec{J}_Q$ is the heat flux (flux of internal energy), $\vec{j}_i$ are the particle fluxes for each i component, $\vec{F}_i$ are the forces, μ_i are the chemical potentials, A_j are the chemical affinities of the j quasi-chemical reactions, and v_j are the reaction rates. From the second law of thermodynamics, the entropy source strength is positive definite and equal to zero in equilibrium.

The basic assumption underlying this model is the concept of "local equilibrium". That is, although the whole system may be far from equilibrium, the particles in each differential volume are in equilibrium with each other. If one considers the small distances and interaction times among particles within a differential volume and the large distances and interaction times among particles from different differential volumes of a system, the concept of local equilibrium is a reasonable one.

For our purposes here we neglect any temperature gradients or quasi-chemical reactions and assume that the only force on the particles is an electrostatic potential gradient. Equation (6) then reduces to,

$$\sigma_s = -\frac{1}{T}\sum_i \vec{j}_i \cdot \vec{\nabla}\zeta_i \geq 0, \tag{7}$$

where ζ_i is the electrochemical potential. Consider the form of σ_s near equilibrium by expanding it in a series of the generalized forces around $\vec{\nabla}\zeta_i = 0$. The first term is zero because $\sigma_s = 0$ in equilibrium, and the second term, linear in $\vec{\nabla}\zeta_i$, is zero because σ_s is positive definite. The third term, quadratic in $\vec{\nabla}\zeta_i$, is the first non-zero term. Retaining only this term we can see that, to first order, near equilibrium,

$$\vec{j}_i \alpha - \vec{\nabla}\zeta_i \ . \tag{8}$$

Going from particle current to electric current, Eq. (8) tells us that the correct expression for the equation-of-state of this isothermal system is,

$$\vec{J}_i = n_i \mu_i \vec{\nabla}\zeta_i \ , \tag{9}$$

where n_i and μ_i are the concentration and mobility of the i particles. Equation (9), of course, is a well-known result. We went through this analysis to show that it is correct to first order, under the assumptions discussed, and that it can be derived from the second law of thermodynamics. In general, all of the quantities in Eq. (9) can vary with position and time.

We now need to obtain an expression for the electrochemical potential for indistinguishable particles. For a

grand canonical ensemble of particles near equilibrium, it can be shown [6] that the distribution function is approximately,

$$f = \left[1 + \exp\left(\frac{\varepsilon-\zeta}{kT}\right)\right]^{-1} \tag{10}$$

That is, it has the same form as the Fermi-Dirac distribution except that, in general, f, ε, ζ, and T can vary in time and position. Equation (10) is obtained under the local equilibrium assumption and is valid only to first order. Thus, Eqs. (9) and (10) are derived with the same assumptions and approximations, and we can use them to analyze heterostructures keeping this in mind.

4.3 HETEROJUNCTION MODEL

Let us apply Eq. (10) to obtain an expression between the concentration of electrons in the conduction band and their electrochemical potential. In the usual way, we multiply the distribution function times the density-of-states and integrate over the band to obtain,

$$n = \int_{\varepsilon_c}^{\infty} g(\varepsilon) f(\varepsilon) d\varepsilon \ , \tag{11}$$

where ε_c is the bottom of the conduction band. For a dilute distribution of electrons, Eq. (11) gives,

$$n = N_c \exp\ (\zeta - \varepsilon_c), \tag{12}$$

where N_c is the effective density-of-states of the conduction band. In general, all four quantities in Eq. (12) can vary with time and position.

Using Eqs. (9) and (12), we have the general near-equilibrium equation-of-state for electron flow in a heterojunction,

$$\vec{J}_n = n\mu_n \vec{\nabla}\left(\varepsilon_c + kT \ln \frac{n}{N_c}\right) \quad (13)$$

Notice, that all of the quantities in this equation can, in general, vary with position and time including N_c. It is the neglect of the term $-\vec{\nabla}(\ln N_c)$ which leads to the inconsistency mentioned previously. A similar expression can be obtained for the hole current:

$$\vec{J}_p = p\mu_p \vec{\nabla}\left(\varepsilon_v - kT \ln \frac{p}{N_v}\right) \quad (14)$$

Let's examine each of the thermodynamic forces in Eqs. (13) and (14). The forces $\vec{\nabla}\varepsilon_c$ and $\vec{\nabla}\varepsilon_v$ represent variation in composition or bandgap as well as applied and built-in electric fields due to space charge. The component of these forces which has equal and opposite effect on electrons and holes can be associated with electric field, with the rest associated with band-gap variations. The forces $\vec{\nabla}(\ln n)$ and $-\vec{\nabla}(\ln p)$ are the usual diffusion terms. The thermodynamic forces $-\vec{\nabla}(\ln N_c)$ and $\vec{\nabla}(\ln N_v)$ can be regarded as entropy forces: that is, they act to drive the electrons and holes to regions of higher density-of-state or higher entropy. These forces are required, therefore, by the second law of thermodynamics, and must be included in a heterostructure analysis.

We will now show that including these entropy forces eliminates the inconsistancy in the analysis of an abrupt p-n heterojunction. In equilibrium, from Eqs. (13) and (14) the built in potential of the space charge region is,

$$qV_0 = \Delta\varepsilon_c + kT\ln\left(\frac{n_n N_{cp}}{N_{cn} n_p}\right) , \tag{15}$$

or

$$qV_0 = -\Delta\varepsilon_v + kT\ln\left(\frac{p_p N_{vn}}{N_{vp} P_n}\right) . \tag{16}$$

Using Eq. (1) these two expressions can be shown to be equal. When the junction is forward-biased, the holes injected into the n-side in the depletion approximation are,

$$P_n = P_p \frac{N_{vn}}{N_{vp}} \exp\left[\frac{q(V-V_0)-\Delta\varepsilon_v}{kT}\right] . \tag{17}$$

Turning the applied voltage off in Eq. (17), we obtain Eq. (16) and the inconsistancy is removed.

Notice that in this analysis we have made no assumptions about the continuity of the infinite vacuum level (electron affinity rule) or any other level. However, if we refer to Eqs. (7) and (8), in equilibrium there is no entropy production and

$$\sum(\vec{\nabla}\zeta_i)^2 = 0 , \tag{18}$$

or

$$\vec{\nabla}\zeta_i = 0 . \tag{19}$$

If the electrochemical potentials are referenced to the infinite vacuum level, then it must be continuous.

4.4 REFERENCES

1. H. Kroemer, "Problems in the Theory of Heterojunction Discontinuities", *Critical Reviews of Solid State Science* 5, 555, (1975).

2. J.L. Shay, S. Wagner, and J.C. Phillips, "Heterojunction Band Discontinuities", *Applied Physics Letters* 28, 31, (1976).

3. H.R. Frensley and H. Kroemer, "Prediction of Semiconductor Heterojunction Discontinuities from Bulk Band Structures", *Journal of Vacuum Science and Technology* 13, 810, (1976).

4. M.J. Adams and A. Nussbaum, "A Proposal for a New Approach to Heterojunction Theory", *Solid-State Electronics* 22, 783, (1979).

5. P. Glansdorff and I. Prigogine, *Thermodynamic Theory of Structure, Stability, and Fluctuations*, (Wiley-Interscience, London, 1971).

6. D.N. Zubarev, *Nonequilibrium Statistical Thermodynamics*, (Consultants Bureau, New York, 1974).

5. INERTIAL TRANSPORT DEVICES

Since the primitive unit cell of the II-IV-V_2 chalcopyrites is four times as large as that of their III-V sphalerite analogs, the first Brillouin zone is one-fourth as large. For this reason and because of their small effective masses, a potential application for these chalcopyrites may be in inertial transport devices such as space-charge limited diodes or Zener oscillators. In this section the physics of these devices is described.

5.1 SPACE-CHARGE LIMITED DIODES

The following reprint describes the current-voltage characteristic of a space-charge limited diode in a semiconductor with non-parabolic bands.

Collisionless Space-Charge Limited Currents in Semiconductors with Nonparabolic Bands

M. W. MULLER

Abstract—The current-voltage relation for space-charge limited collisionless flow is computed for a model semiconductor with a hyperbolic band structure as deduced from two-band $\bar{k} \cdot \bar{p}$ perturbation theory. The expected current is reduced significantly below the constant effective mass value for voltages in excess of the bandgap, and the high-voltage asymptotic relation is V rather than $V^{3/2}$.

Manuscript received October 27, 1980; revised December 5, 1980. This work was supported by ONR Contract N00014-79-C-0840 and AFOSR Contract 79-0096.

The author is with the Department of Electrical Engineering, Washington University, St. Louis, MO 63130.

In devices that use high-mobility, low effective mass semiconductors, the mean free time between collisions of a carrier can become equal to, or longer than an oscillation period, or the mean free path between collisions equal to or longer than a typical device dimension.

Under such conditions the carrier transport in semiconductors is not governed by the traditional friction-dominated Ohm's law behavior. The motion of the carriers for the short times or distances of primary interest for device operation may be more accurately described by the inertial or ballistic equation of motion.

The simplest device for studying inertial transport is the short space-charge limited semiconductor diode. Calculations of the behavior of such diodes, without collisions, and with few collisions [1] have been reported. These calculations assume that the carrier effective mass is independent of energy.

In a device that operates in a collision-free, or nearly collision-free regime, the carriers that contribute to the device current reach energies corresponding to the voltages applied to the device. In small and fast devices, these are of the order of 1 V. In most semiconductors, especially those with small effective mass carriers, the bands depart from parabolicity at energies well below 1 eV. The effective mass generally increases with energy. Thus the current is smaller than one would predict for a parabolic band structure.

To assess the magnitude of this effect, we use the conduction band structure of a model narrow-gap semiconductor as computed by two-band $\bar{k} \cdot \bar{p}$ perturbation theory. Such a model can provide a fair approximation to the real band structure in the vicinity of the conduction band extremum.

Assuming a direct-gap semiconductor, and placing the zero of energy at the conduction band minimum, the theory gives the hyperbolic band structure

$$\epsilon = \frac{1}{2}\epsilon_g \left[\sqrt{1 + \frac{2\hbar^2 k^2}{m^* \epsilon_g}} - 1 \right]. \tag{1}$$

The theory also provides a relation between the effective mass m^* and the bandgap ϵ_g, but for the present purpose these two parameters may be chosen independently, for instance to fit a measured band structure.

To obtain the carrier velocity as a function of energy, we use

$$\frac{\partial \epsilon}{\partial k} = \frac{\hbar^2 k}{m^*} \left(1 + \frac{2\hbar^2 k^2}{m^* \epsilon_g} \right)^{-1/2} \tag{2}$$

and then solve (1) for k^2

$$k^2 = \frac{2m^*}{\hbar^2} \left(\epsilon + \frac{\epsilon^2}{\epsilon_g} \right). \tag{3}$$

Substituting this in (2) gives

$$\frac{\partial \epsilon}{\partial k} = \sqrt{\frac{2}{m^*}} \frac{\hbar(\epsilon + \epsilon^2/\epsilon_g)^{1/2}}{1 + \epsilon/\epsilon_g} = 2\hbar v_s \frac{\epsilon/\epsilon_g + \epsilon^2/\epsilon_g^2}{1 + 2\epsilon/\epsilon_g}$$

$$= \hbar v_s \frac{(2m^* v_s^2 \epsilon + \epsilon^2)}{m^* v_s^2 + \epsilon} \tag{4}$$

0018-9383/81/0500-0604$00.75

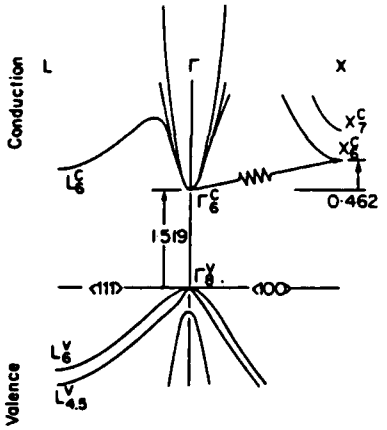

Fig. 1. GaAs band structure with parabolic and hyperbolic conduction band approximation.

where we have defined a band-structure limited velocity

$$v_s \equiv (\epsilon_g/2m^*)^{1/2}. \tag{5}$$

Fig. 1 shows the current best plot of the GaAs band structure [2] with both (1) using the experimental ϵ_g and m^*, and a $\hbar^2k^2/2m^*$ parabola superposed on the plot. The hyperbola of (1) is evidently a much better fit.

The Poisson equation for a semiconductor uniformly doped with n_0 donors/cm^3 carrying an electron current density J is

$$\frac{d^2V}{dx^2} = \frac{\rho}{\epsilon} = -\frac{qn_0}{\epsilon} + \frac{J}{\epsilon v} \tag{6}$$

where ϵ is the dielectric constant and v is the electron velocity.

Electrons injected at $x = 0$ acquire a velocity

$$v = \frac{1}{\hbar}\frac{\partial \epsilon}{\partial k} \tag{7}$$

when their energy $\epsilon = qV \equiv \phi$.

Using the band structure gradient from (4) brings the Poisson equation into the form

$$\phi'' = -\frac{q^2n_0}{\epsilon} + \frac{Jq}{\epsilon v_s}\,\frac{(m^*v_s^2 + \phi)}{(2m^*v_s^2\phi + \phi^2)^{1/2}} \tag{8}$$

where a prime denotes d/dx. Equation (8) can be integrated once to give

$$(\phi')^2 - (\phi'(0))^2 = \frac{2Jq}{\epsilon v_s}(\phi^2 + 2m^*v_s^2\phi)^{1/2} - \frac{2q^3n_0}{\epsilon}\phi. \tag{9}$$

Assuming space charge limitation $\phi'(0) = 0$, and changing to reduced variables

$$u \equiv \frac{\phi}{2m^*v_s^2}, \quad j = \frac{J}{qn_0v_s}, \quad \lambda = \frac{x}{(\epsilon m^*/n_0q^2)^{1/2}v_s} \tag{10}$$

we can write the diode equation, the integral of (9), in the form

$$\int_0^v du[j(u^2 + u)^{1/2} - u]^{-1/2} = l$$

where $u = v(V = V_0$, the applied voltage) at $\lambda = l(x = L$, the diode length). The normalized variables are: diode voltage in units of $2m^*v_s^2/q$—four times the kinetic energy the carriers would have if their effective mass were constant at the band edge value, and they were moving with the limiting velocity v_s; if the $\vec{k}\cdot\vec{p}$ perturbation theory is taken literally, this unit is equal to ϵ_g/q; current density in units of qn_0v_s—the current that would flow if the mobile carriers from the doping were moving with velocity v_s; diode length in units of $v_s\tau_p$, with τ_p the plasma oscillation period of the semiconductor.

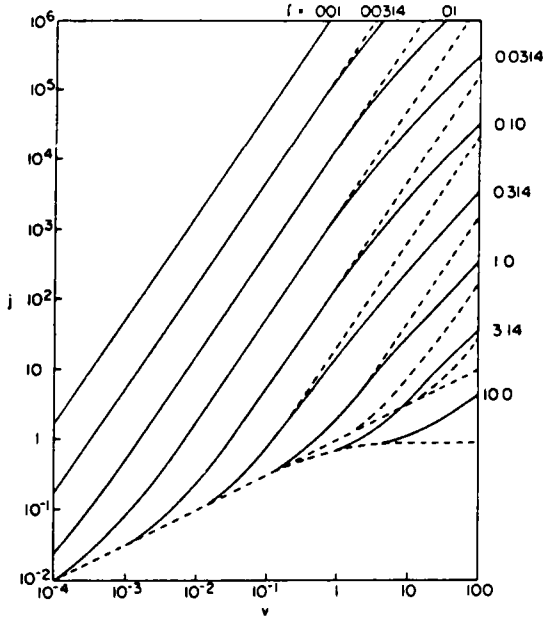

Fig. 2. Space-charge limited current-voltage relation of a collisionless semiconductor.

Curves of current density versus voltage are shown in Fig. 2 as full curves. For comparison the current density-voltage curves one would compute assuming constant effective mass are shown dashed.

The vacuum diode analog 3/2 power law holds only for $V_0 \lesssim \epsilon_g$, and then only for $l \lesssim 1$. That means very short diodes—for GaAs with $n_0 = 10^{16}$, shorter than 0.25 μm. The limiting higher voltage behavior is $J \propto V$ rather than $J \propto V^{3/2}$; the J–V curves bend over.

In the typical size and operating voltage range of GaAs devices the corrections indicated here appear significant but not dramatic. They are likely to be rather more important in devices made from smaller bandgap, lower m^* material.

We have not extended the diode characteristics into the low-current region at the lower ends of the curves. The problems encountered by modeling this operating regime are rather complicated, involving multiple-valued functions and possibly spatial and temporal instabilities [3]. Moreover, the neglect of collisions and thermal energies is less justifiable in this low-voltage region.

References

[1] M. S. Shur and L. F. Eastman, *IEEE Trans. Electron Devices*, vol. ED-26, p. 1677, 1979; and *IEEE Electron Device Lett.*, vol. EDL-1, p. 147, 1980.

[2] D. E. Aspnes, in *Proc. 6th Internat. Symp., GaAs and Related Compounds*, L. F. Eastman, Ed. London: Inst. Phys., 1977.

[3] B. Abraham-Shrauner, in Rep. ONR 80-1, Washington Univ., unpublished.

5.2 PHASE FOCUSING OF ZENER OSCILLATIONS

In the absence of scattering and interband tunneling the motion of a carrier in a crystalline solid subjected to a steady uniform electric field is described by a rectilinear trajectory in reciprocal space, traversing the extended Brillouin zone at a constant rate proportional to the field. The corresponding motion in direct space is periodic with a frequency proportional to the field, and is called a Zener oscillation [4]. Zener oscillations are a possible source of electromagnetic radiation. They are most likely to be useful at extremely high frequencies, in the millimetric and submillimetric region of the spectrum, where oscillation periods are comparable with or shorter than the scattering lifetime, so that an appreciable fraction of the carriers present complete one or more cycles of oscillation before they are scattered.

The well-known equation of motion of a carrier in a steady uniform electric field $\bar{E}$ is

$$\hbar\dot{\bar{k}} = q\bar{E} \tag{1}$$

where q is the charge of the carrier and $\hbar\bar{k}$ its crystal momentum. The carrier's velocity $\bar{v}$ is

$$\bar{v} = \frac{1}{\hbar}\nabla_k E_n(\bar{k}) \tag{2}$$

where E_n is the momentum-dependent energy in the band of index n. If $\bar{k}$ lies along a principal crystal direction, the period of the Zener oscillation is

$$\tau = \frac{h\kappa}{q\bar{E}} \quad , \tag{3}$$

where κ is the diameter of the first Brillouin zone in the direction $\bar{k}$, and the length of the Zener orbit is

$$\ell = \frac{E_{nmax} - E_{nmin}}{qE} \tag{4}$$

where E_{nmax} and E_{nmin} are respectively the maximum and minimum energy attained by the carrier in the course of its traversal of the Brillouin zone.

For a typical cubic semiconductor of lattice constant of order 5Å, in an electric field of order 10^5V/cm the Zener oscillation frequency is of order 10^{12}Hz, and if the energy width of the band is, say, 5eV, the length of the Zener orbit is 0.5 μm. (It is convenient to remember that the length of the Zener orbit is equal to the distance in which the electrostatic potential of the applied field drops by the energy width of the band.)

These equations, numbers, and statements are to be understood in terms of a quasi-classical picture of the crystal electrons. This picture is commonly accepted for the heuristic description of carriers in solid state electron devices, and with appropriate caution it can be used here. It is well established that interband tunneling is negligible in applied potentials which differ by much less than the bandgap at adjacent lattice sites, in the sense that the tunneling probability per Zener period is much less than unity. We shall show elsewhere that in such fields crystal electrons can indeed be localized simultaneously in momentum in a region small compared with a Brillouin zone, and in position in a region small compared with the Zener orbit [5]. The localization is not independent of time, but like a coherent state of a harmonic oscillator [6] (and unlike a wave packet representing a free electron) it does not spread indefinitely but recurs with the Zener period. This property arises from the equal energy spacing of the Stark ladder

states that constitute the wave packet. We also accept here as plausible (and shall demonstrate elsewhere) that a small change in the field orientation only slightly affects the Zener spectrum [5].

The power radiated by oscillating charges is small unless they oscillate in phase. A striking if trivial example is presented by the charges in filled bands of a solid. If a field is applied to the solid, each of these charges moves according to Eq. (1), executing Zener oscillations (without being scattered, because all the final states are full). Of course, these oscillations are electromagnetically unobservable, since the "radiated" fields of all the charges cancel because of their uniform distribution over 2π radians of phase.

In order to use the Zener oscillations of carriers in a partially filled band for the coherent generation of radiation, it is necessary to start all the carriers oscillating together - phase initialization - and to maintain them in step as they oscillate - phase focusing.

We propose to meet both these requirements by means of a device which is schematically represented in Fig. 1. In Fig. 1(a) is shown band diagram typical of a semiconductor heterojunction quantum well. Such planar structures have been fabricated by heteroepitaxy in a variety of semiconductors [7]. They can be designed by varying the relative stoichiometry and doping of the constituent materials and the thickness of the layer comprising the well to contain one or a few one-dimensionally bound electron and/or hole states, as indicated in the figure. In Fig. 1(b)the band diagram of the same structure is shown with a uniform steady electric field applied at right angles to the plane of the epitaxial layer. In the presence of such a field, it becomes energetically possible for the bound electron to tunnel

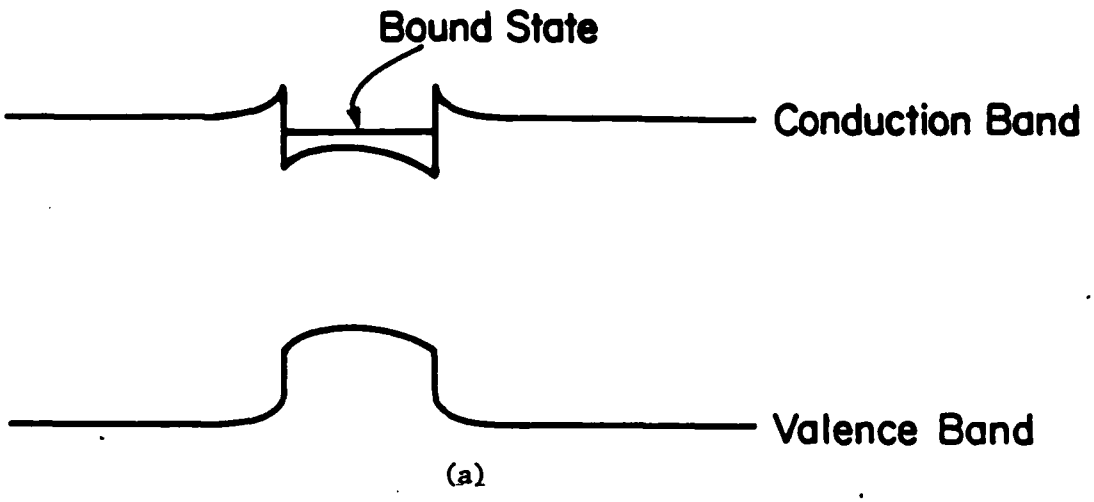

Figure A. Quantum Well Structure

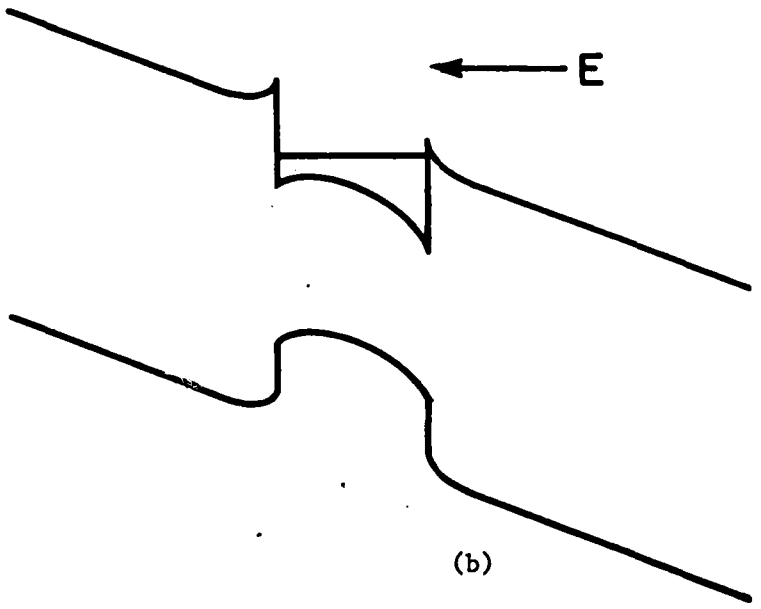

Figure B. Quantum Well In Transverse Electric Field.

Figure 1 Schematic band diagram of a heterojunction quantum well: (a) in equilibrium; (b) with an applied transverse electric field.

through the energy barrier confining it to the quantum well, i.e. to be internally field-emitted into the conduction band of the "host" semiconductor, to the right of the quantum well in the figure. Once the electron has been field-emitted into the conduction band, it will execute Zener oscillations until it encounters a scattering event.

Upon being scattered, the electron will resume its oscillatory motion, in general with a new phase unrelated to the phase prior to the scattering event, thus becoming useless or harmful. But observe that the motion of these dephased electrons in general resumes "downhill" from the original starting point, so that their Zener oscillation orbits extend to the right beyond the maximum excursion of the favorably phased carriers. If an appropriate collecting structure is placed in this region a distance just in excess of ℓ in Eq. (4) away from the quantum well it will eliminate the dephased carriers from the interaction region. This constitutes the phase focusing mechanism of the device concept. From the parenthetical remark made above in connection with Eq. (4) it follows that the length of the interaction region becomes equal to ℓ when the voltage across it reaches $q^{-1}(E_{nmax} - E_{nmin})$; thus the spacing of the collecting electrode sets the lower frequency limit of the device through Eqs. (4) and (3).

It is convenient to discuss the oscillation of the planar charge density and the associated time-varying electromagnetic fields in lumped-circuit terms. In this language, the continuity of the total (conduction and displacement) current associated with the oscillating charge requires a current to flow in any external circuit surrounding it. This current in turn will induce a voltage that alters the field in the interaction region. If the external circit impedance is a

capacitance, the phase of this voltage is such as to increase the applied steady voltage at those times when we wish to have carriers field-emitted across the potential barrier forming the edge of the quantum well in order to oscillate in synchronism with carriers field-emitted during earlier cycles of oscillation. Since the tunneling probability depends very sensitively on the width of the potential barrier, and since the width is smallest when the voltage is largest, the feedback from the external circuit serves to maintain coherence in the phase initialization.

The capacitive load required for the appropriate phasing of the feedback can be supplied in a variety of ways. Because of the high operating frequency of the device, it may be convenient to use quasi-optical circuitry together with a junction capacitance. Alternatively, a microwave-type implementation could have the device operate into a short-circuited transmission line between a quarter and a half wavelength long.

The collecting structure should be an interface with an effectively infinite recombination velocity. This suggests a reverse-biased semiconductor-metal junction as the positive electrode, which also serves as the bias supply.

Fig. 1(b) has been drawn with the assumption that the field in the interaction region is uniform. This implies that the semiconductor is intrinsic. Design considerations may make it advantageous to use doped material. In this case the field in the interaction region would be non-uniform, implying trivial modification of the equations. Whether intrinsic or doped, the interaction region is depleted under operating conditions, that is to say, the device is operated in punch-through.

Another simplifying feature of Fig. 1 is the symmetry of the walls of the quantum well, by no means a necessary condition. By varying the doping on the "upstream" side, it is possible to control the design and the high-frequency circuit function of the junction at the negative contact which resupplies carriers to the well.

In the mode described here the proposed device will function best at frequencies above the scattering rate, which is typically of order 10^{12}/sec, that is to say, in the Terahertz region of the spectrum. As seen in the numerical estimate following Eq. (4), the dimensions and operating parameters of a 10^{12}Hz device are quite reasonable. Operation at lower frequencies should be possible, since the proposed phase-focusing mechanism eliminates scattered carriers. The efficiency, however, would suffer, since the scattered carriers contribute to the total current and hence to the input power.

The scattering, of course, also contributes to the heat input to the device. One may expect a lower-frequency limit to the operation to be set by this heating. Since a lower-frequency device also needs to be thicker, it may reach the avalanching threshold, also setting a low-frequency limit.

5.3 TERAHERTZ ZENER OSCILLATOR

5.3.1 Device Concept

Zener oscillations are the real-space oscillations that correspond to the uniform rectilinear reciprocal-space trajectory of a crystal electron in a steady applied electric field. Such oscillations have a period τ given by

$$\tau = \hbar\kappa/qE$$

and an amplitude ℓ given by

$$\ell = (1/qE)(E_{max} - E_{min})$$

where q is the electronic charge, E the electric field, κ the "diameter" of the Brillouin zone along the field direction, and E_{max} and E_{min} respectively the maximum and minimum of the band structure traversed along the electron's trajectory. These expressions assume the absence of scattering and interband tunneling events during time intervals of interest, assumptions to be discussed below.

Oscillations of this type are capable of generating high-frequency electromagnetic radiation. If the charge carriers are to radiate efficiently, they should oscillate in phase. We propose a scheme whereby carriers in a semiconductor are injected into a depleted interaction region periodically, with the period of the Zener oscillations, and are automatically removed if they are scattered and lose phase coherence.

The principle of the proposed device is schematically illustrated in Fig. 1. Fig. 1a is the thermal equilibrium band diagram of a structure consisting of a wide-bandgap intrinsic semiconductor interaction region between a narrower-gap n-doped semiconductor on the left and a metal contact on the right. In Fig. 1b the structure is shown with a positive voltage applied to the metal. It is now possible for electrons to tunnel through the n-i heterojunction barrier (to be internally field-emitted) into the interaction region, where they will execute Zener oscillations.

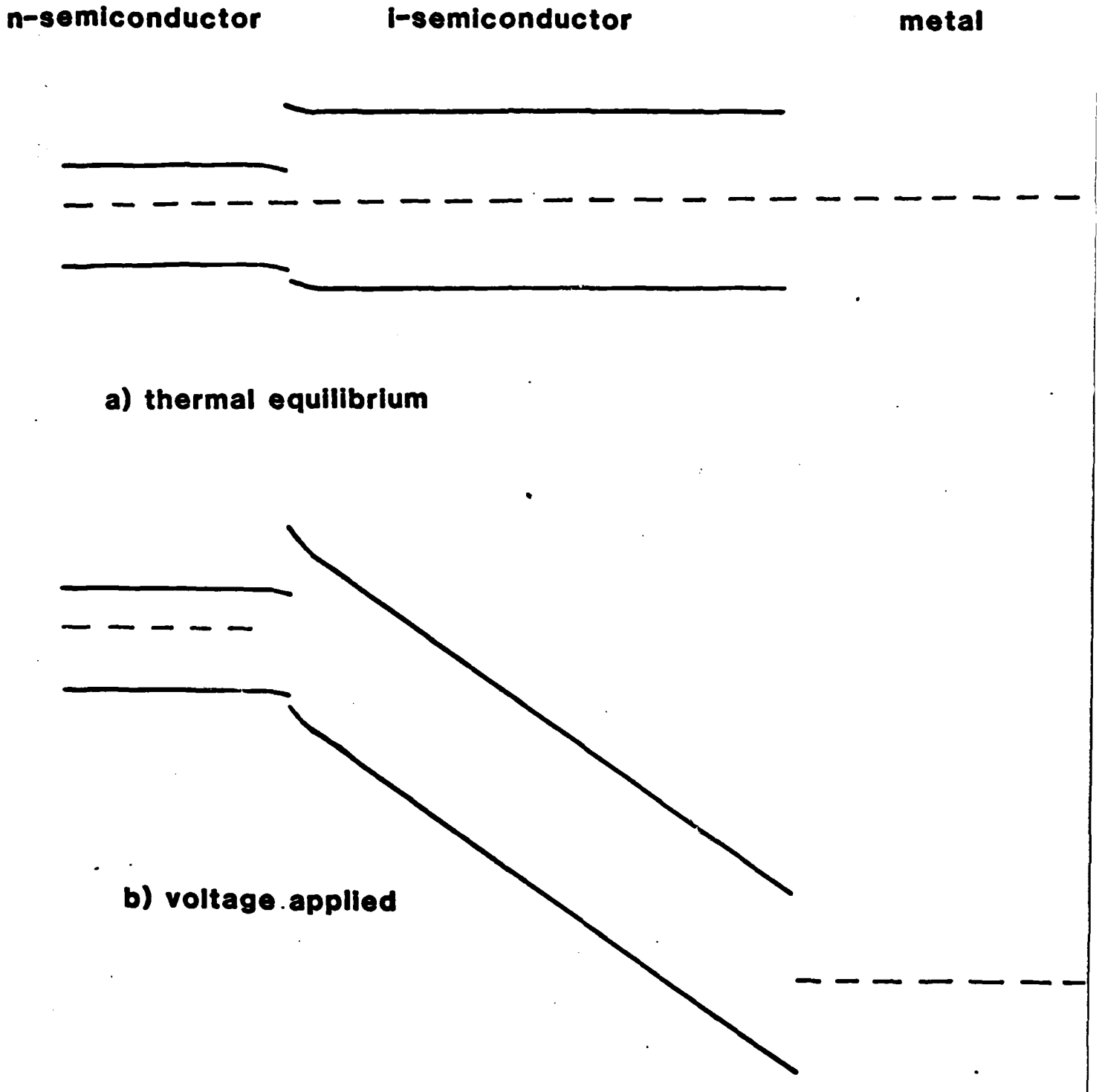

Figure 1 Schematic band diagram of a heterojunction quantum well: (a) in equilibrium; (b) with an applied transverse electric field.

A moment's thought reveals that the length of the Zener orbit ℓ becomes equal to the width of the interaction region when the voltage across it is equal to $V_c = (1/q)(E_{max} - E_{min})$. Thus with a voltage equal to or greater than V_c across the interaction region, a conduction electron's Zener orbit remains confined to that region, unless it experiences a scattering event.

If it is scattered, the electron will resume its oscillatory motion, in general with a new phase unrelated to the phase prior to the scattering event, thus becoming useless or harmful. But observe that the motion of these dephased electrons in general resumes "downhill" from the original starting point, so that their Zener orbits extend to the right, beyond the maximum excursion of the favorably phased carriers. Thus if the voltage across the interaction region exceeds V_c only slightly, these dephased carriers will be collected at the metal contact and eliminated from the interaction region.

The oscillating planar charge density of conduction electrons and the associated time-varying electric fields constitute a current. The total (convection plus displacement) current must be continuous across the junctions and in the external return circuit. The current in the external circuit in turn induces a voltage which appears across the interaction region. If the reactance of the external circuit is a capacitance, the phase of this voltage is such as to increase the applied steady voltage at those times when we want the n-region to inject new carriers into the interaction region to oscillate in synchronism with carriers emitted during earlier cycles. Since the tunneling probability depends very sensitively on the width of the heterojunction potential barrier, and since thewidth is smallest when the voltage is largest, the feedback from the external circuit serves to maintain coherence in the phase initialization.

The feedback loop is analogous, in some measure, to that of an IMPATT oscillator. The transit-time phase delay is similar in both devices. The

IMPATT's delay due to the avalanchemultiplication is replaced here by the phase shift of the circuit reactance.

5.3.2 Discussion

The description of the proposed device has been couched in terms of a quasi-classical picture of the crystal electrons. This picture is commonly accepted for the heuristic description of carriers in solid-state electron devices, and with appropriate caution it can be used here. It is well established that interband tunneling is negligible in applied potentials which differ by much less than the bandgap at adjacent lattice sites, in the sense that the tunneling probability per Zener period is much less than unity.

We have also assumed that the crystal electron can be localized simultaneously in momentum in a region small compared with the Brillouin zone, and in position in a region small compared with a Zener orbit. Such localization is routinely taken for granted in low fields, but must be examined more carefully in the present context. For reasons to be discussed presently, we shall assume a Zener oscillation frequency in excess of 10^{12} Hz. In a typical cubic semiconductor of lattice constant of order 5Å, this requires a field of order 10^5V/cm, and if the energy width of the band is, say, 5eV, the length of the Zener orbit is 0.5μm. We have constructed gaussian wavepackets of one-band solutions of the Schroedinger equation (Stark and Houston states) for a model tight-binding band structure, and verified that in a field of 10^5V/cm such wave packets can be simultaneously confined to less than 1% of the Brillouin zone and to less than 1/30 of a Zener orbit length. The localization in position is not independent of time, but like a coherent state of a harmonic oscillator [8] (and unlike a wave packet representing a free electron) it does not spread indefinitely but recurs with the Zener period. This property arises from the equal energy spacing of the Stark states that

constitute the wave packet. (In the numerical example given above, the position uncertainty fluctuates by about 50% in the course of a cycle of oscillation.)

Some concern has been expressed in the literature about the stability of the Stark ladder spectrum "in the sense that the slightest change in the direction of E completely alters the level system" [9]. Although this statement is strictly true - indeed, the Zener oscillations are aperiodic unless E lies along a reciprocal lattice vector - it has little bearing on our present concerns. Using a realistic GaAs conduction band structure [10] we have determined that the effect of a small change in the direction of E is akin to a slow frequency modulation of the Stark spectrum.

We have chosen a Zener frequency of order 10^{12}Hz and a corresponding field of order 10^{5}V/cm as appropriate for the testing of our device concept. This choice is supported by the experimental results of Koss and Lambert [11], who, in fields of this order of magnitude, claimed to observe the Stark ladder in the GaAs conduction band. The result consisted of a step-like modulation of the Franz-Keldysh effect on the interband optical absorption. Although the resolution of the experiment was not very good, and thus the evidence is not entirely conclusive, it implies that the lifetime of a Stark level is of order 10^{-12}s.

A lifetime of this order of magnitude appears to be in conflict with a variety of experimental and theoretical results [12] on high-field transport and avalanche ionization which yield scattering rates, mainly associated with phonon emission, of at least 10^{14}/s. Although we are unable at present to account for this apparent discrepancy, we can suggest a direction in which a resolution might be found.

Existing high-field transport theory is based on calculations involving the interaction of quasi-particles represented as plane waves. Such theories are strictly valid only in effectively infinite homogeneous media.

Although for many experimental situations this is a quite reasonable approximation, it may be expected to fail when the scale of the non-uniformities becomes small enough. In particular, in the device proposed here we deal with very tightly localized quasi-particles. This localization must be at least partially conserved in a scattering event. One may expect that this requirement places a constraint, in effect a set of selection rules, on the type of scattering event that may occur. As is generally true of any constraint, the restrictions thus imposed must reduce the probability of occurrence of the event and increase the lifetime. Moreover, the allowed events may have less drastic experimental consequences than a complete randomization. For example, coherent forward scattering, even with the loss of a phonon energy, may not be fatal to the usefulness in the interaction region of a Zener oscillating carrier. Such qualitative arguments have a good deal of plausibility, to render them quantitative will require methods that have recently been developed to deal with high-field, small-device transport phenomena [13].

Both the magnitude and the field sensitivity of the heterojunction tunneling current will be satisfactory for this application. These quantities can be estimated using the Fowler-Nordheim equation. With a barrier height of a few hundred meV and a field of 10^5 V/cm we find current densities comparable with those of tunnel diodes. The fractional field sensitivity is

$$\frac{E}{I}\frac{dI}{dE} = 2 + \frac{4\sqrt{(2mH)}}{3\hbar}\frac{H}{qE}$$

where I is the tunneling current, m the carrier effective mass, and H the barrier height. This ratio can be adjusted by varying the doping, and it will generally exceed 10.

The capacitive load required for the appropriate phasing of the feedback can be designed in a variety of ways. Because of the high operating frequency of the device, it may be convenient to use quasi-optical cir-

cuitry. Then the capacitance might be provided by a reverse-biased junction on the narrower-gap side of the heterojunction. Alternatively, a microwave-type implementation could have the device operate into a short-circuited transmission line between a quarter and a half wavelength long.

Fig.1 has been drawn with the assumption that the interaction region is intrinsic. This is not a necessary condition, and design considerations may make it advantageous to use doped material. In this case the field in the interaction region would be non-uniform, implying trivial modification of the equations. Whether intrinsic or doped, the interaction region under operating conditions is depleted, that is to say, the device is operated in punch-through.

5.4 REFERENCES

1. M.S. Shur and L.F. Eastman, IEEE Trans. Electron Devices, vol. ED-26, p. 1677, 1979; and IEEE Electron Device Lett., vol. EDL-1, p. 147, 1980.

2. D.E. Apnes, in Proc. 6th Internat. Symp., GaAs and Related Compounds, L.F. Eastman, Ed. London: Inst. Phys., 1977.

3. B. Abraham-Shrauner, in Rep. ONR 80-1, Washington Univ., unpublished.

4. C. Zener, Proc. Roy. Soc. A145, 523 (1934).

5. P. Roblin and M.W. Muller, unpublished work.

6. R. Glauber, Phys. Rev. 131, 2766 (1963).

7. See for example, H. Kroemer, Jap. Jl. Appl. Phys. 20, 9 (1981).

8. R. Glauber, Phys. Rev. 131, 2766 (1963).

9. G.H. Wannier, Rev. Mod. Phys. 34, 645 (1962).

10. We are indebted to Prof. K. Hess for providing these band structure data.

11. R.W. Koss and L.M. Lambert, Phys. Rev. B5, 1479 (1972).

12. See for example H. Shichijo, K. Hess, and G.E. Stillman, Appl. Phys. Lett. 38, 80 (1981); T.P. Pearsall, R.E. Nahory, and J.R. Chelikowski, Phys. Rev. Lett. 39, 295 (1977); J.R. Barker, J. Phys. C6, 2663 (1973).

13. K.K. Thornber, Sol. St. Electr. 21, 259 (1978); D.K. Ferry and J.R. Barker, Sol. St. Electr. 23, 545 (1980).

6. PUBLICATIONS

1. M.W. Muller, "Collisionless Space-Charge Limited Currents in Semiconductors with Nonparabolic Bands", IEEE Transactions on Electron Devices 28, 604, (1981).

2. G.A. Davis and C.M. Wolfe, "Liquid Phase Epitaxial Growth of $Zn_xCd_{1-x}SnP_2$ on InP", J. Electronic Materials 11, 505 (1982).

3. M.W. Muller, P. Roblin, and D.L. Rode, "Proposal for a Terahertz Zener Oscillator", Proceedings of Workshop on Physics of Submicron Devices (Plenum Press, to be published).

4. M.W. Muller and D.L. Rode, "Phase Focusing of Zener Oscillations", submitted to Appl. Phys. Letters.

5. C.M. Wolfe, N. Holonyak, Jr., and G.E. Stillman, "Nonequilibrium Thermodynamics of Heterostructures", Semiconductors and Semiconductor Devices (Prentice Hall, to be published).

6. G.A. Davis and C.M. Wolfe, "Liquid Phase Epitaxial Growth of $ZnSnP_2$ on GaAs", to be submitted to J. Electrochem. Soc.

7. G.A. Davis and C.M. Wolfe, "Effective Masses and Nonparabolic Band Structure of $Zn_xCd_{1-x}SnP_2$", to be submitted to J. Phys. Chem. Solids.

8. G.A. Davis and C.M. Wolfe, "Raman Scattering and Optical Phonon Spectra of $Zn_xCd_{1-x}SnP_2$", to be submitted to J. Phys. Chem. Solids.

7. MEETING TALKS

1. Camellia M.L. Yee, Heidi J. Carroll, and C.M. Wolfe, "Chemical Vapor Deposition of $ZnGeAs_2$ on GaAs", Electronic Materials Conference, Ithaca, NY, 24-27 June 1980.

2. G.A. Davis and C.M. Wolfe, "Liquid Phase Epitaxial Growth of $CdSnP_2$", Electronic Materials Conference, Ithaca, NY, 24-27 June 1980.

3. M.W. Muller, "Inertial Transport with Non-Parabolic Bands", Late News Paper, International Symposium on GaAs, Vienna, Austria, 22-24 September 1980.

4. C.M. Wolfe, "Amphoteric Dopants and Compensation in GaAs", Workshop on Shallow Impurities in Semiconductors, Wright-Patterson AFB, Ohio, 21-22 May 1981.

5. G.A. Davis and C.M. Wolfe, "Liquid Phase Epitaxial Growth of $Zn_xCd_{1-x}SnP_2$", Electronic Materials Conference, Santa Barbara, California, 24-26 June 1981.

6. M.W. Muller, P. Rodlin, and D.L. Rode, "Proposal for a Terahertz Zener Oscillator", Workshop on Physics of Submicron Devices, Champaign, Illinois, 28-30 June 1982.

8. PERSONNEL

The personnel who worked on this grant at various times during the three-year period were:

Prof. C.M. Wolfe, Principal Investigator

Prof. M.W. Muller, Faculty Associate

Mr. Gary A. Davis, Graduate Research Assistant and IBM Fellow

Ms. S. Julie Hsieh, Graduate Research Assistant

Ms. Camellia M.L. Yee, Graduate Research Assistant

Ms. Heidi J. Carroll, Undergraduate Laboratory Assistant

All three of the Graduate Research Assistants have master's degrees and are doctoral candidates.

The degrees awarded on this grant up to the present time are:

August 1980, Camellia M.L. Yee, Master of Science, "Chemical Reactions in the Vapor Phase Growth of $ZnGeAs_2$";

August 1981, Gary A. Davis, Master of Science, "Liquid Phase Epitaxial Growth of $Zn_xCd_{1-x}SnP_2$";

May 1982, S. Julie Hsieh, Master of Science, "Vapor Phase Growth of $ZnGeAs_2$".

Also anticipated is:

January 1983, Gary A. Davis, Doctor of Science, "Growth and Characterization of $Zn_xCd_{1-x}SnP_2$".